Theses and Dissertations

6-1-2010

Total internal reflection holographic microscopy (TIRHM) for quantitative phase characterization of cell-substrate adhesion

William Mason Ash
University of South Florida

Total Internal Reflection Holographic Microscopy (TIRHM) for

Quantitative Phase Characterization of Cell-Substrate Adhesion

by

William Mason Ash, III

A dissertation submitted in partial fulfillment
of the requirements for the degree of
Doctor of Philosophy
Department of Physics
College of Arts and Sciences
University of South Florida

Major Professor: Myung K. Kim, Ph.D.
Donald Hilbelink, Ph.D.
Dennis Killinger, Ph.D.
Chun-Min Lo, Ph.D.
Garrett Matthews, Ph.D.

Date of Approval:
March 30, 2010

Keywords: Near-Field, Evanescent, Digital Holography, Membrane, Psuedopod, Motility

To friends and family everywhere

ACKNOWLEDGEMENTS

TABLE OF CONTENTS

LIST OF TABLES

LIST OF FIGURES

Total Internal Reflection Holographic Microscopy (TIRHM) for

Quantitative Phase Characterization of Cell-Substrate Adhesion

William Mason Ash, III

ABSTRACT

Total Internal Reflection Holographic Microscopy (TIRHM) combines near-field

microscopy with digital holography to produce a new form of near-field phase

microscopy. Using a prism in TIR as a near-field imager, the presence of microscopic

organisms, cell-substrate interfaces, and adhesions, causes relative refractive index (RRI)

and frustrated TIR (f-TIR) to modulate the object beam's evanescent wave phase front.

Quantitative phase images of test specimens such as *Amoeba proteus*, *Dictyostelium

Discoideum* and cells such as SKOV-3 ovarian cancer and 3T3 fibroblasts are produced

without the need to introduce stains or fluorophores. The angular spectrum method of

digital holography to compensate for tilt anamorphism due to the inclined TIR plane is

also discussed.

The results of this work conclusively demonstrate, for the first time, the

integration of near-field microscopy with digital holography. The cellular images

presented show a correlation between the physical extent of the *Amoeba proteus* plasma

membrane and the adhesions that are quantitatively profiled by phase cross-sectioning of the holographic images obtained by digital holography. With its ability to quantitatively characterise cellular adhesion and motility, it is anticipated that TIRHM can be a tool for characterizing and combating cancer metastasis, as well as improving our understanding of morphogenesis and embryogenesis itself.

CHAPTER 1

INTRODUCTION

Optics being the wonderful special case of electromagnetism that it is, photonics could easily be to this century what electronics has been to the previous one. Digital holography enjoys elements of both. Firmly grounded, as we shall see, in basic physical principles, this research presented here combines digital holography with near-field microscopy to produce a form of phase microscopy motivated by biophysical applications of cellular mechanics, namely, the characterization of cellular adhesion.

Biological systems make for an interesting set of physics. Understanding how cells get to where they go, and what they do when they get there, has been a keen interest in many fields since Leeuwenhoek first observed protozoa (Figure 1.1). More recently, cellular adhesion and its chemo-mechanics (i.e., cadherin dynamics) have been an area of significant research for quite some time and are key to understanding interactive motility and signaling processes such as morphogenesis [1-3] and even metastasis [4].

Many cells move by crawling over surfaces. Axons grow over long distances, macrophages and neutrophils crawl to sites of infection, fibroblasts migrate through connective tissues and cancer cells metastasize. This is accomplished by a set of coordinated events, namely, the protrusion of lamellipodia, the adhesion of focal
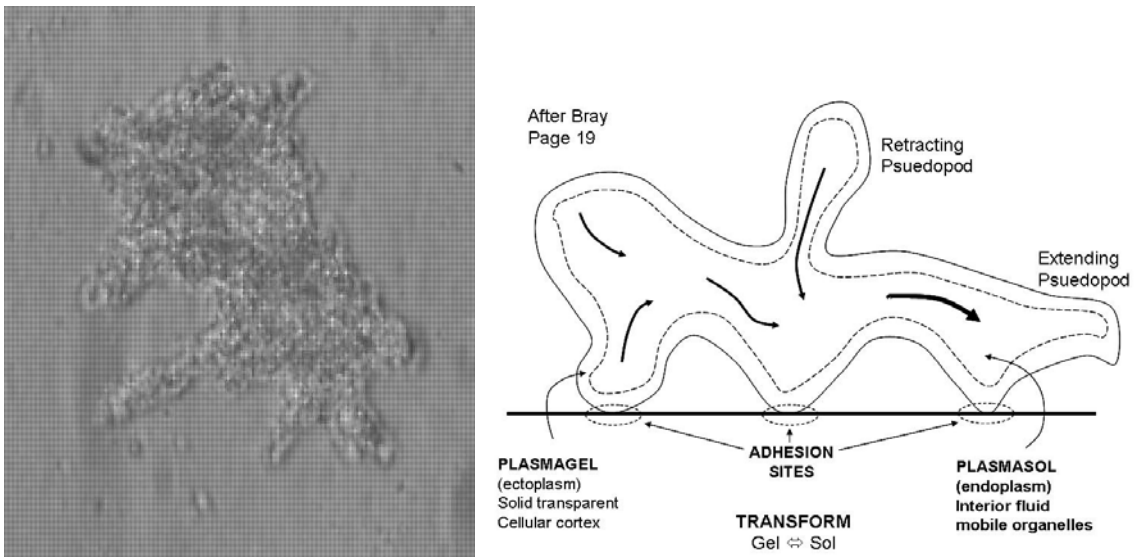
Figure 1.1 Amoeba Proteus psuedopod adhesion. a) Amoeba Proteus (Field-of-

View (FOV) 250 x 300 μm), b) walking pseudopodia (After Bray) [5,6]

contacts, the establishment of traction and the release of old adhesions. Therefore, the ability to generate accurate, quantitative surface profiles of live cellular adhesion to help better understand the important process of cellular motion, adhesion and transduction gains increasing emphasis.

1.1 Optical Microscopy

Arguably one of the key inventions in the history of mankind, the microscope has come for many to symbolize Science itself. Figure 1.2 presents an inverted microscope currently in use at the University of South Florida's Digital Holography and Microscopy Laboratory (USF DHML). In this photograph here the instrument is able to view through the underside of a Petri containing a colony of *Amoeba Proteus* and capture images with its CCD camera for recording, display and later retrieval by the supporting personal computer system.

While perhaps daunting in its abilities, the compound microscope is fairly straightforward in its basic construction, if not its underlying optical design (Figure 1.4). The scheme is termed "Compound" because there are at least two optical elements involved; an "objective" lens which captures the light diffracted by the "object" or specimen/sample and the ocular or eyepiece through which the operator views the resultant image.

For instance, total magnification;

$$M = \frac{L_T}{f_0} \frac{L_0}{f_e} \qquad (1.1.1)$$

3
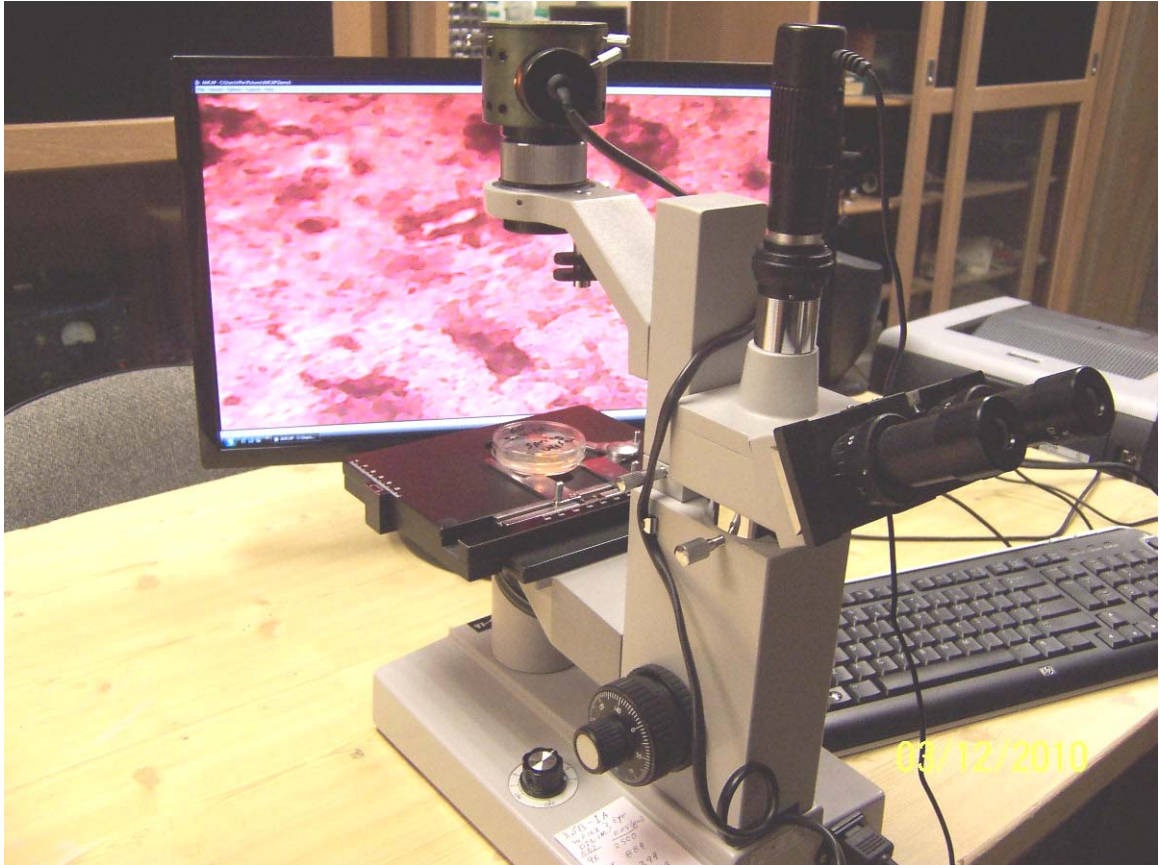
Figure 1.2 Optical Microscopy. An inverted microscope with CCD camera viewing

an *Amoeba Proteus* culture in a Petri dish.

For our hypothetical compound microscope of Figure 1.3, if the tube length L_T = 160mm (standard), L_0 = 250mm, the near point for the human eye ("puntum proximum"), f_0 = 4.0mm and f_e = 210mm, the magnification is;

$$M = \frac{160\text{mm} \cdot 250\text{mm}}{4.0\text{mm} \cdot 210\text{mm}} = 48\text{X} , \qquad\qquad (1.1.2)$$

and, Abbe's expression for resolution, is given by

$$R = \frac{\lambda}{\text{N.A.}} \qquad , \qquad\qquad (1.1.3)$$

where λ is the wavelength of the illumination, and N.A. stands for "Numerical Aperture"; the amount of light the system can pull in. Assuming that λ = 532nm (in the green) and the N. A. = 0.25, yields,

$$R = 532\text{nm} / 0.25 \sim 2.1\mu\text{m} \qquad\qquad (1.1.4)$$

or the ability to resolve about 1/10th the width of an ordinary human hair (~50 microns).

Living cells and their intracellular constituents are largely transparent and therefore quite problematic for conventional bright-field microscopy. A number of techniques have been developed for rendering transparent phase objects visible and have played important roles in the development of modern biology and medicine.

5
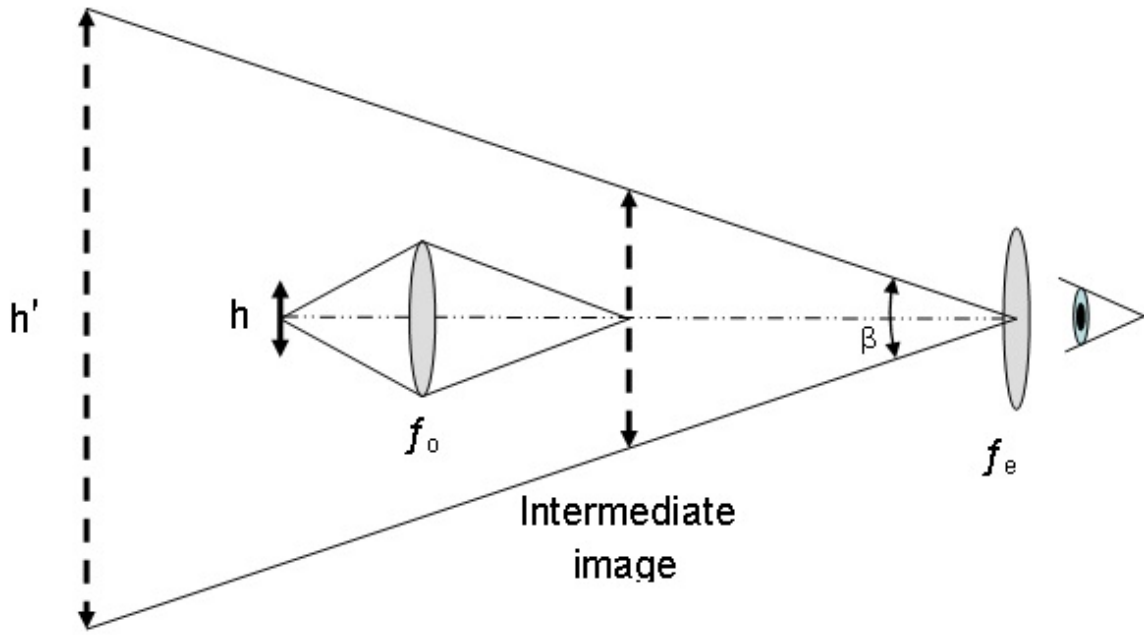
Figure 1.3 Compound microscope schematic. (After O'Shea, [7]).

For example, in dark-field microscopy, only the scattering centers and boundaries contribute to the image signal against a zero background [8]. In Zernike Phase Contrast Microscopy, phase variation is converted into amplitude variation by the use of a phase plate and spatial filtering [9]. Interference microscopy, using a Michelson objective for example, produces fringes of equal thickness for a transparent object [10]. Although these techniques are very effective in making transparent objects visible, the phase to amplitude conversion is nonlinear and there are significant artifacts in the images; such as the halo in Zernike phase contrast or the disappearance of contrast along the direction perpendicular to shear in differential interference contrast (DIC) microscopy. Unfortunately, while useful, these techniques do not produce entirely quantitative phase images.

The optical phase of the light transmitted through transparent objects generally conveys quantitative information about the object, such as the physical thickness and the index of refraction [11], which in turn are functions of the physical density or properties of the chemical concentration. High precision measurements of optical phase can thus reveal subtle changes in these parameters that accompany the cellular processes of interest. As an example, in order to obtain quantitative phase images, one can perform interferometric measurement of a focused beam of light on an object, and scan the beam in a raster fashion. Alternatively, as in phase-shifting interference microscopy [12], the quantitative phase image is obtained from a combination of multiple interferograms.

The microscopy of cellular adhesion is important for a deeper understanding of cellular motion and morphogenesis. Cell-substrate interactions, including attachment,

spreading, morphology changes, and migration, require a complex series of events to occur in a regulated and integrated manner. An orchestrated set of activities takes place that includes, the protrusion of pseudopodia, the formation of new adhesions, and the development of traction, followed by the subsequent release of previous adhesions in order to produce movement. To date, the primary tools for imaging and studying these surface processes have been total internal reflection fluorescence microscopy (TIRFM) and interference reflection microscopy (IRM). The techniques in optical microscopy that we are most interested in here are Phase Contrast Microscopy, Interference Reflection Microscopy and TIR Fluorescence Microscopy.

1.1.1 Phase Contrast Microscopy (PCM)

Invented by Frits Zernike, for which he won the 1953 Nobel Prize in Physics (Table 1.1) [13], Phase Contrast Microscopy was an early technique for rendering transparent "phase-objects" visible without the use of stains that result in cell death. In the Zernike phase contrast microscope, the phase variation is converted into amplitude variation, by use of a phase plate (and perhaps spatial filtering). While quite successful and still in use today, PCM has a drawback in that it's conversion of phase information to amplitude also produces a spurious halo effect. PCM is also important here because TIRHM is also a form of phase microscopy.

As we shall soon see, also worthy of note is PCM's resemblance to holography, in that, PCM uses a type of "reference beam" in its undiffracted illumination path (called the Surround beam "S") that is recombined with the information carrying diffracted

8

Table 1.1 Nobel prizes in physics important to Digital Holography and TIRHM[14]

Year	Recipients	Awarded for
1907	Albert Abraham Michelson	optical precision instruments
1953	Frits Zernike	Phase contrast microscope
1964	Charles Hard Townes Nicolay Gennadiyevich Basov Aleksandr Mikhailovich Prokhorov	laser principle
1971	Dennis Gabor	Holographic method
2000	Jack S. Kilby	Integrated circuit
2009	Charles K. Kao	Transmission of light in fibers
	Willard S. Boyle George E. Smith	CCD sensor

beam. Figure 1.4 presents phase contrast imagery of a SKOV-3 ovarian cancer cell while Figures 1.5 and 1.6 depict the workings of the technique.

1.1.2 Interference Reflection Microscopy (IRM)

In the IRM technique, developed by Curtis in 1964 [15], light waves reflected from the two surfaces at the cell-substrate interface produce interference fringes. Certainly an older technique that does not enjoy nearly the widespread popularity of TIRFM, IRM does allow for estimation of interface thickness profile. When proteins associated with the focal contacts are analyzed utilizing immunofluorescence, the contacts themselves may be viewed using IRM. However, in this instance, the interference image of the interface is usually complicated by the reflection image of the cell body and its contents, thus allowing only a qualitative interpretation of the surface profile. Confocal adaptation of IRM can reduce the spurious reflection signal, but raster scanning of such system imposes significant speed limitations.

Figure 1.7 is Verschueren's apparatus [16] for Interference Reflection Microscopy (IRM) which he describes as "Monochromatic green light is linearly polarized and directed into the objective lens. The light reflected by the object passes through the quarter-wavelength plate on its way to the object and is circularly polarized. On its way back it is linearly polarized again but with a 90° difference in the direction of polarization, and therefore passes through the analyzer. Stray light from reflections at the lens surfaces, with unaffected polarization, is extinguished by the crossed analyzer. Stray
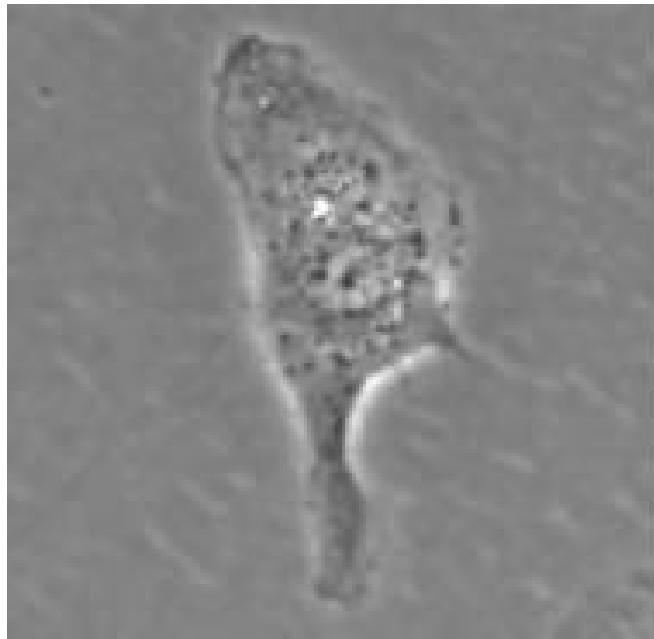
Figure 1.4 Phase Contrast of SKOV-3 Ovarian cancer cell. Note the characteristic "halo-ing" effect, (USF DHML)
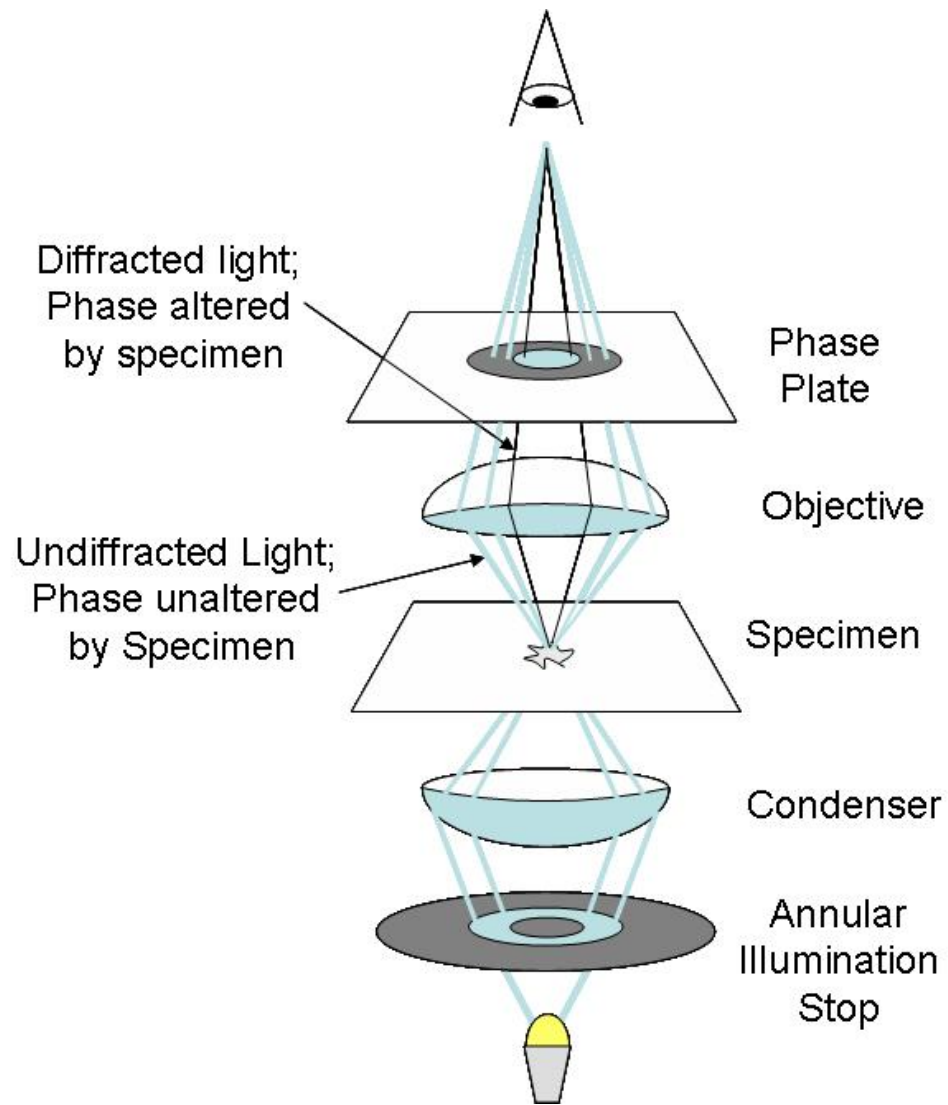
Figure 1.5 Phase Contrast Microscopy. The phase contrast method; annular illumination

(i.e. central stop) together with annular phase coating at objective back focal plane (After

The Phase Contrast Microscope http://nobelprize.org/)
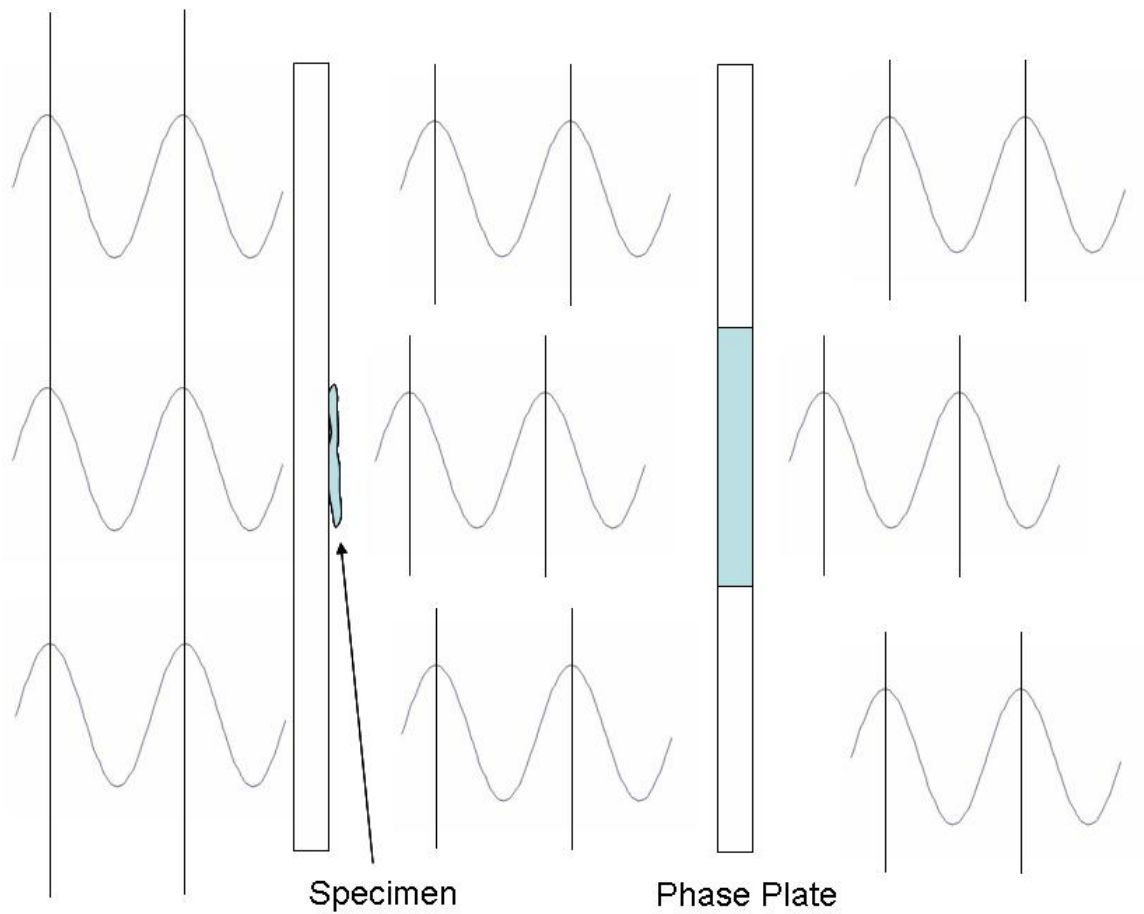
Figure 1.6 Phase Plate. The phase-plate increases the phase difference to half a wavelength. Destructive interference between the two sorts of light when the image is projected results in the specimen appearing as a dark object.

(After The Phase Contrast Microscope http://nobelprize.org/)
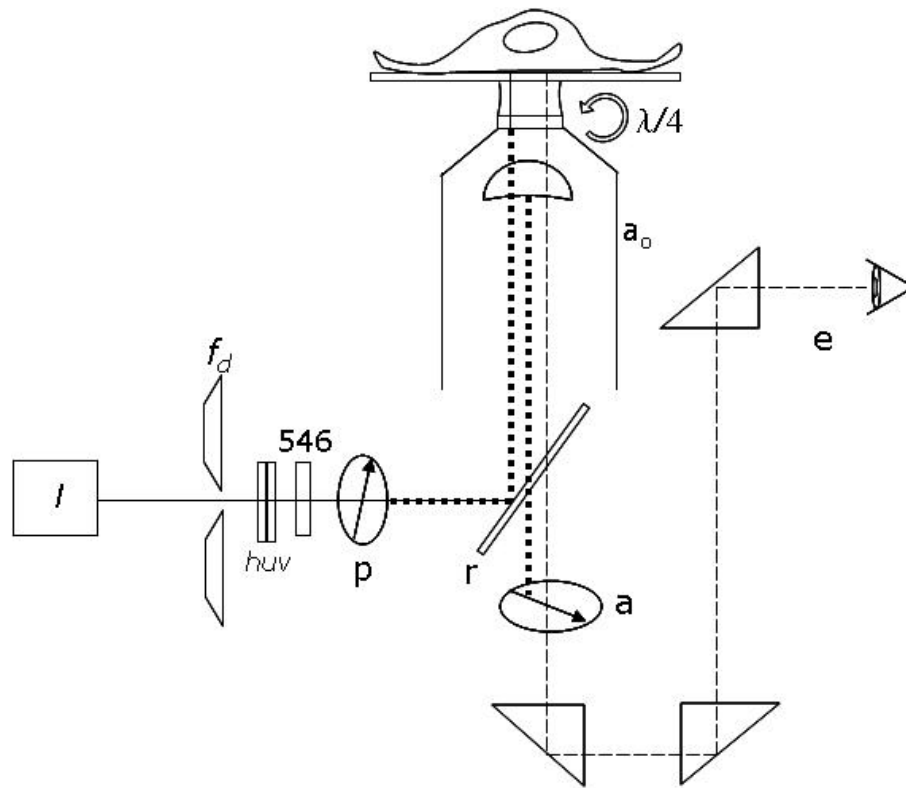
Figure 1.7 Interference Reflection Microscopy (IRM). After Verschueren [16] "Diagram of optical equipment and pathways in an interference reflection microscope without aperture diaphragm and with antiflex device. /, mercury arc lamp, f_d field diaphragm; *huv,* heat reflecting and *u.v.* absorbing filters; *546,* interference 546nm band filter; p, polarizer; *r,* semi-reflecting mirror; a_o, antiflex objective with a rotatable quarterwave quartz plate mounted on the front lens, with its orientation set at 45 ° to the polarizer's direction to obtain maximal image brightness; *a,* analyzer, oriented at 90° to the polarizer; *e,* eyepiece.

light from reflections within the object but from outside the field of interest is eliminated by encircling a small area with the field diagram. In the absence of an aperture iris, the illuminating numerical aperture is at its maximum value for the objective used."

On the other hand, in interference reflection microscopy (IRM), light waves reflected from two surfaces of the cell-substrate interface produces interference fringes, thus allowing estimation of the interface thickness profile [17,18]. However, with IRM the interference image of the interface is usually complicated by the reflection image of the cell body and its contents, thus allowing only a qualitative interpretation of the surface profile. Confocal adaptation of IRM can reduce the spurious reflection signal, but raster scanning of such a system imposes significant speed limitations.

1.1.3 Total Internal Reflection Fluorescence Microscopy (TIRFM)

In 1981, D. Axelrod [19,20] demonstrated total internal reflection fluorescence microscopy (TIRFM) to be an effective technique to study cell-substrate contact. When light is incident from inside of a higher-index n_1 medium into a lower-index one n_2, with the angle of incidence greater than the critical angle given by $\theta_c = \sin^{-1}(n_2/n_1)$, all of the incident light is reflected back to the first medium (Figure 1.8). There is no propagating field in the second medium, except for the evanescent wave, whose amplitude decays exponentially over a distance of a fraction of a wavelength. Although the evanescent field is non-propagating, it can modulate the phase of the reflected n_1 wave either through inhomogeneous refractive indices in the n_2 medium, frustrated TIR (fTIR) geometries, or, if suitable dye molecules are placed in the evanescent field, they can absorb energy from

Snell's Law of Refraction

$$n_1 \sin\theta_1 = n_2 \sin\theta_2$$

$$\Longrightarrow \theta_{crit} = \text{Sin}^{-1}(n_2/n_1)$$

n_2

n_1

1

θ_2

2

3

3

Total Internal Reflection

$\theta > \theta_{crit}$

2

θ_{crit}

θ_1

1
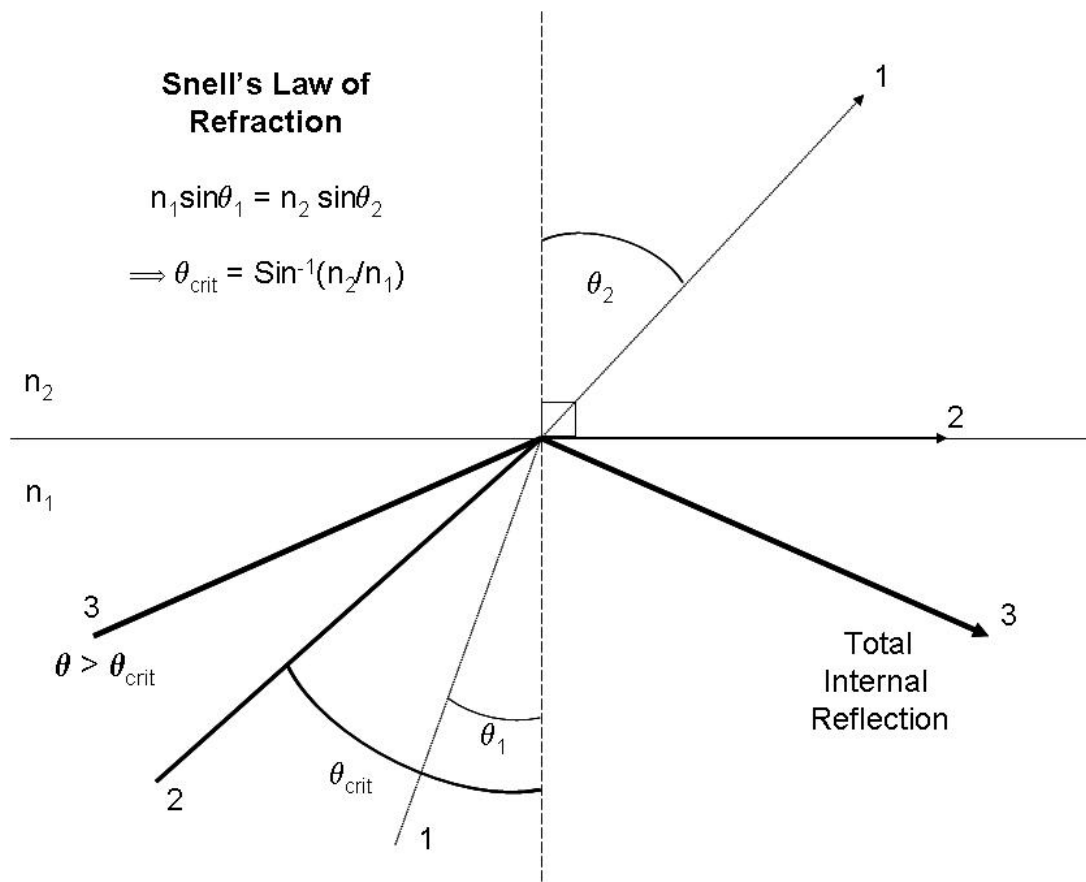
Figure 1.8 Total Internal Refraction (TIR) from Snell's Law. Total Internal refraction can be viewed as a special case of Snell's Law. Snell's Law by itself however cannot describe the near-field evanescent wave. As we shall see in Section 2, the complete description of TIR requires Fresnel Reflection Theory.

the field and fluoresce. All these processes can be used for near-field microscopy.

Fluorescence microscopy, or TIRFM, reveals localization of fusion protein in cell focal

adhesions at the substrate interface in dramatic contrast to the blur produced by out-of-

plane fluorescence in the epi-illumination image. While this provides for excellent

functional imaging, on the other hand, information on the morphology of the cellular

membrane surface is largely absent in TIRFM. Figure 1.9 depicts a TIRFM system as

proposed by Axelrod.   It is intended to be implemented as an added feature on an

existing microscope platform. Laser illumination being brought in to a prism underneath

the sample, such that the laser beam goes into TIR and propagates a near-field into the

sample of interest and exciting added fluorophores to produce a form of dark field

microscopy.

In TIRFM, fluorophores within ~100 nm of the coverslip's surface are excited by

the TIR evanescent field and give off a fluorescent signal which is then imaged. TIRFM

image reveals localization of fusion protein in cell focal adhesions at the substrate

interface in dramatic contrast to the blur produced by out-of-plane fluorescence in the

epi-illumination image. Although TIRFM is limited to investigation of structures and

processes occurring at or near the coverslip-specimen interface, it is simultaneously

fortuitous that many questions of current interest in the biological and biomedical

sciences can be probed at the cell membrane.

While this provides for excellent functional imaging, TIRFM only allows for non-

quantitative morphology of the cellular interface and information on the cellular

membrane surface is largely absent. Recent technical advances have greatly facilitated a
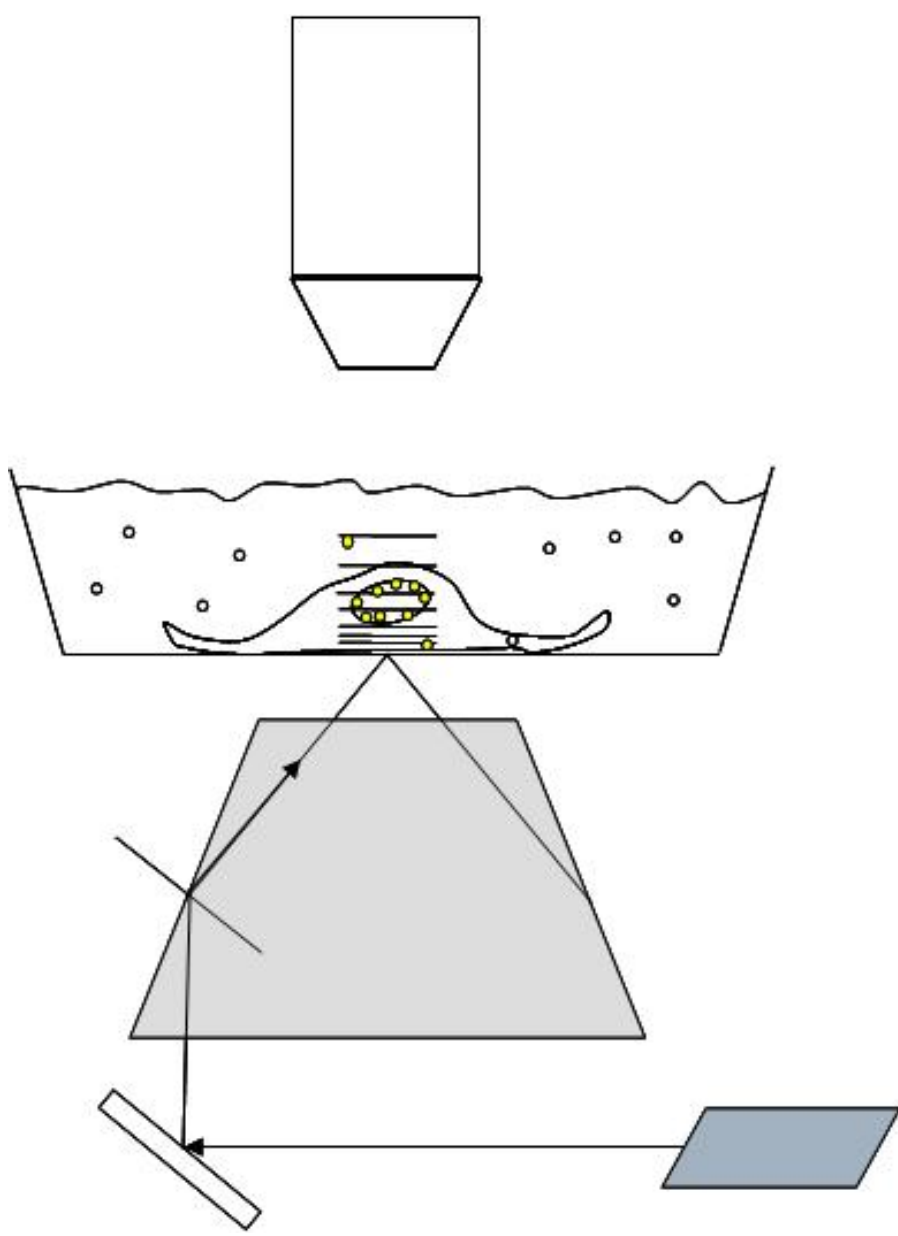
Figure 1.9 Total Internal Reflection Fluorescence Microscopy (TIRFM). A laser source illuminates a TIR prism sets up a near-field through the sample that excites fluorophore tags. (After Axelrod [21]).

wider range of applications of TIR microscopy. TIRFM imagery reveals localization of fusion protein in cell focal adhesions at the substrate interface in dramatic contrast to the blur produced by out-of-plane fluorescence in the epi-illumination image.

1.2   Holography

An interesting and useful application of the electromagnetic phenomena of interference and diffraction is realized in holography. The principle of holography consists essentially of a "write mode" and a "read mode" using a coherent source as depicted in Figure 1.10.

In the "write" 'mode', the object of interest is illuminated with a coherent "object beam"; coherent in the sense that it is of a single wavelength and in phase with little dispersion and high stability in these features over the lengths and times of interest. This object beam is then superposed with a "reference beam" (ref) of the same coherence and the resulting "interferogram" (superposition of wavefronts) is 'written' onto a photographic plate (emulsion), perhaps with (physical) "real space" optics, to create a hologram. When that hologram is illuminated with an analogous reference beam, the image information is reconstructed and "read".

1.2.1   Digital Holography

In digital holography [22], the holographic interference pattern is optically generated by the superposition of object and reference waves (Figure 1.11). But, instead of a photographic plate, the hologram is digitally sampled by a CCD camera and
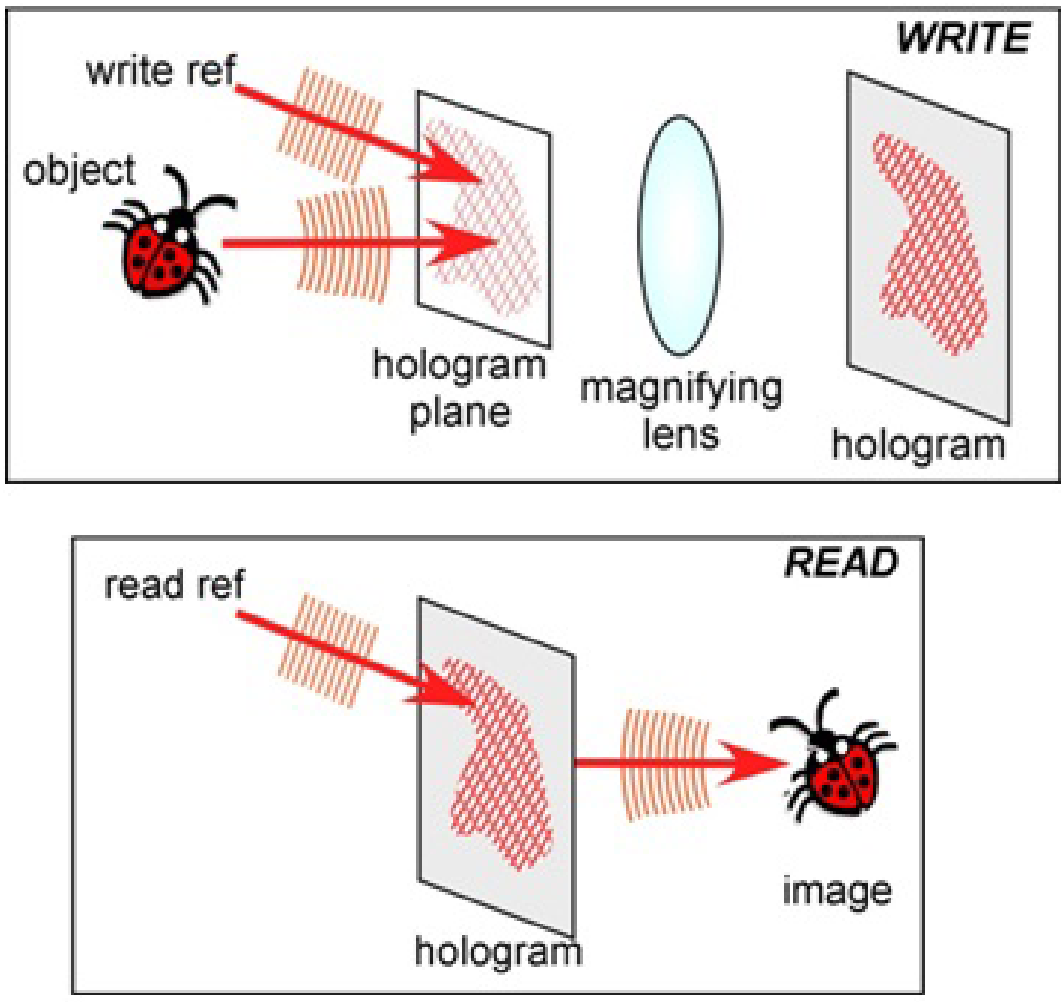
Figure 1.10 The Principle of Holography [23]

transferred to a computer as an array of numbers. The propagation of optical field is completely and accurately described by diffraction theory, which allows for numerical reconstruction of the image as an array of complex numbers representing the amplitude and phase of the optical field [24].

Digital holography offers a number of important advantages such as the ability to acquire images rapidly, the availability of both amplitude and phase information of the optical field, and versatility of the image processing techniques that can be applied to the complex field data. Indeed, digital holography by numerical diffraction of optical fields allows for imaging and image processing techniques that are not feasible in real space holography. Schnars and Jueptner, in 1994, were the first to use a CCD camera connected to a computer as the input, in what is now referred to as digital holography [25]. Since then, developments of digital holographic techniques and applications have been gaining pace ever more rapidly. A number of different methods have been considered for numerical reconstruction including the Fresnel transform, the Huygens convolution, and angular spectrum analysis [26] .

Various special techniques have been developed to enhance the capabilities and to extend the range of applications. Phase-shifting digital holography allows the elimination of zero-order and twin-image components even in an on-axis arrangement [27]. Optical scanning holography can generate holographic images of fluorescence [28]. Application of digital holography in microscopy is especially important, because of the very narrow depth of focus of high-magnification systems [29]. Numerical focusing of holographic images can be accomplished from a single hologram [30]. Direct access to the phase
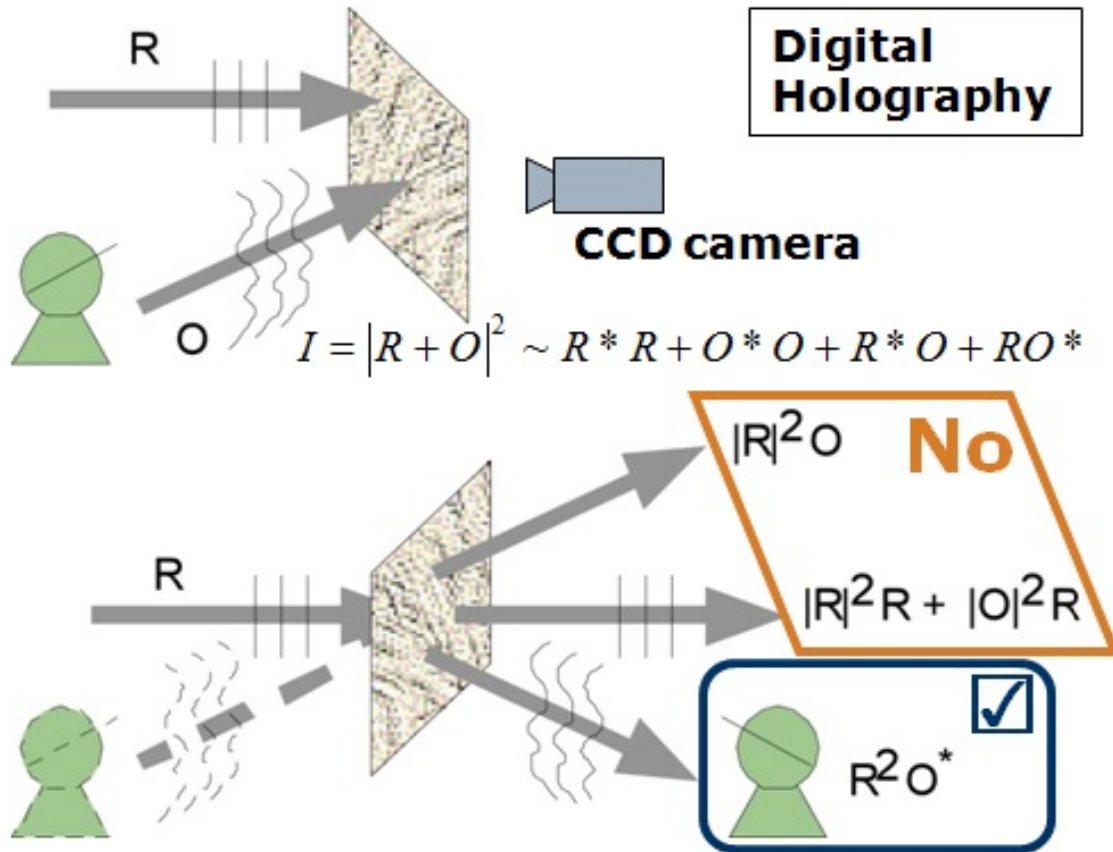
Figure 1.11. Digital Holography. I ≡ Interference wave, R ≡ Reference wave, O ≡ Object wave, * ≡ complex conjugate

information facilitates numerical correction of various aberrations of the optical system, such as field curvature and anamorphism [31].

Digital holography has been particularly useful in metrology, deformation measurement, particle analysis, and vibrational analysis [32,33]. Applications of digital holography for biological microscopy are being actively pursued [34-37]. Low-coherence digital holography allows tomographic imaging [38]. Our University of South Florida Digital Holography and Microscopy Laboratory (USF DHML) has developed digital interference holography for optical tomographic imaging [39,40] as well as multiwavelength phase contrast digital holography for high resolution microscopy [41-43].

1.3 Sample cells

The sample cells used in this research are Amoeba Proteus (Figure 1.1A) [44 45], Dictyostelium Discoideum (myx)amoeba (Figure 1.12) [46-48], SKOV-3 ovarian cancer (Figure 1.13) [49] and 3T3 fibroblast samples (figure 1.14) [50] and were chosen based upon their availability, suitability, relative ease of use and, especially in the instance of SKOV-3 and fibroblast, their importance to the field. The reader is recommended to the references for methods of preparation.

Amoeba Proteus have been used for developmental characterization because of their relative ease of use, their inherent interaction with the substrate and the time scale of their motion. A drawback however, to the proteus amoeba is their size and constantly changing aspect. While some are only a couple hundred microns in extent, some are

physically larger (~ 900µm) than the 10X field-of-view (FOV) that we are dealing with

here. *A. Proteus* are easily kept in the lab environment in cultures consisting essentially

of "pond-water" and fed with *Chilomonas* grown in-situ on bacteria colonies that seem to

do well with some daily aeration, but subsisting largely on "studied neglect" in low light

conditions.

Figure 1.2 depicts the life cycles of Dictyostelium discoideum as related by

Brown and Strassmann of DictyBase "Most of its life, this haploid social amoeba

undergoes the vegetative cycle, preying upon bacteria in the soil, and periodically

dividing mitotically. When food is scarce, either the sexual cycle or the social cycle

begins. Under the social cycle, amoebae aggregate to cAMP by the thousands, and form a

motile slug, which moves towards light. Ultimately the slug forms a fruiting body in

which about 20% of the cells die to lift the remaining cells up to a better place for

sporulation and dispersal. Under the sexual cycle, amoebae aggregate to cAMP and sex

pheromones, and two cells of opposite mating types fuse, and then begin consuming the

other attracted cells. Before they are consumed, some of the prey cells form a cellulose

wall around the entire group. When cannibalism is complete, the giant diploid cell is a

hardy macrocyst which eventually undergoes recombination and meiosis, and hatches

hundreds of recombinants."[51]

Our SKOV-3 ovarian cancer cells (Figure 1.13) were evaluated in two separate

runs; one fixed onto the surface of a BK-7 prism acting as a carrier [52] and a second run

cultured onto the truncated SFL11 prism hypotenuse in Hank's Buffered Saline Solution

(HBSS) requiring an attempt for fast acquisition of "live" phase microscopy before the
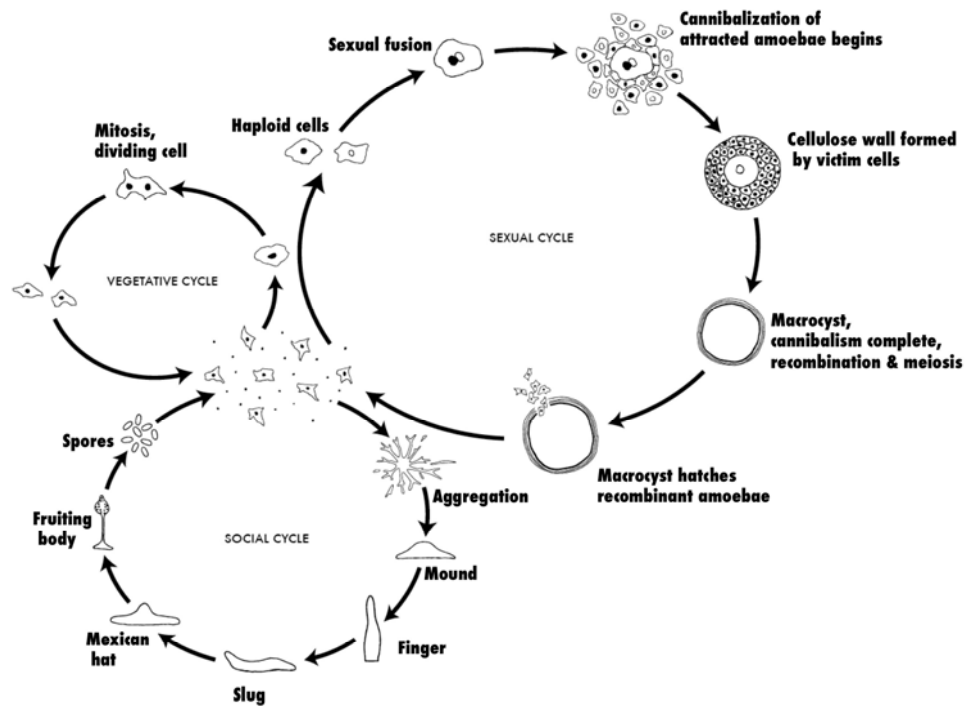
Figure 1.12 The life cycles of Dictyostelium discoideum. (After Brown and Strassmann)[51] Not drawn to scale.

cancer cells succumbed after cooling to room temperature from their preferred 37°C

incubation temperature. In Figure 1.13a) , please note the Zernike phase contrast image

provided for comparison to the digital holography images.

Our 3T3 fibroblast cells had a handling situation similar to the SKOV-3 in that

they were cultured live onto a BK7 prism as a carrier with phase microscopy attempted

before the sample cooled from incubation temperature (37°C) to the laboratory

environment (25°C) the 3T3 being even less robust than the SKOV-3 cells. Figure 1.11 is

an image captured by the author at the University of Illinois GEM4 workshop

1.5 Dissertation Overview

This work may be understood as integrating near-field microscopy with digital

holography to produce a new form of phase contrast microscopy intended to help

understand how cells adhere, how they travel, and what they do, (chemo)mechanically

speaking, when they arrive at their destination. This dissertation presents all of the basic

theory and principles of TIRHM as they relate to near field phase microscopy and digital

holography, how the angular spectrum is implemented, and the physics involved.

 Herein, I present the near field of Fresnel reflection theory and the angular

spectrum method (ASM) of digital holography. Phase shifts from relative refractive index

(RRI) and frustrated TIR (f-TIR) resulting from the presence of focal adhesions and cell-

substrate interfaces on the prism's sensing face modulate the object beam's evanescent

wave phase front. As will be demonstrated, it is these phase shift properties that we make

use of in TIRHM to make it a form of quantitative surface imagery derived from

26
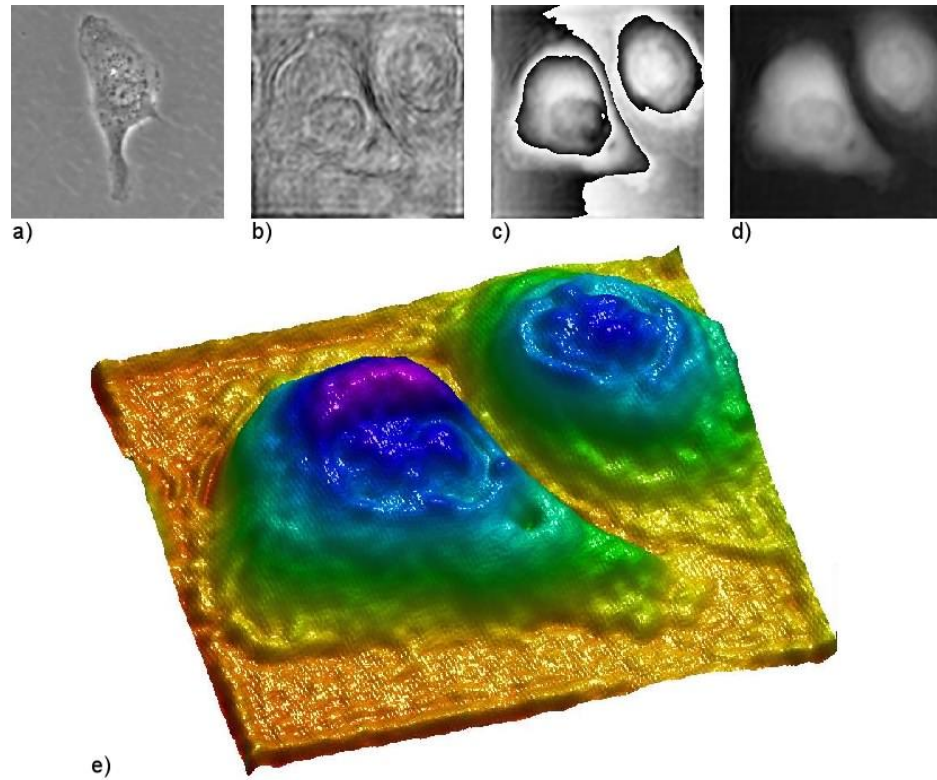
Figure 1.13. Non-confluent SKOV-3 cells. (60 x 60mm2 , 404 x 404 pixels, z = 5mm) a) Zernike phase contrast image, b) amplitude image, c) phase image, d) software-unwrapped, e) 3D perspective pseudocolor of d) (*USF DHML*)
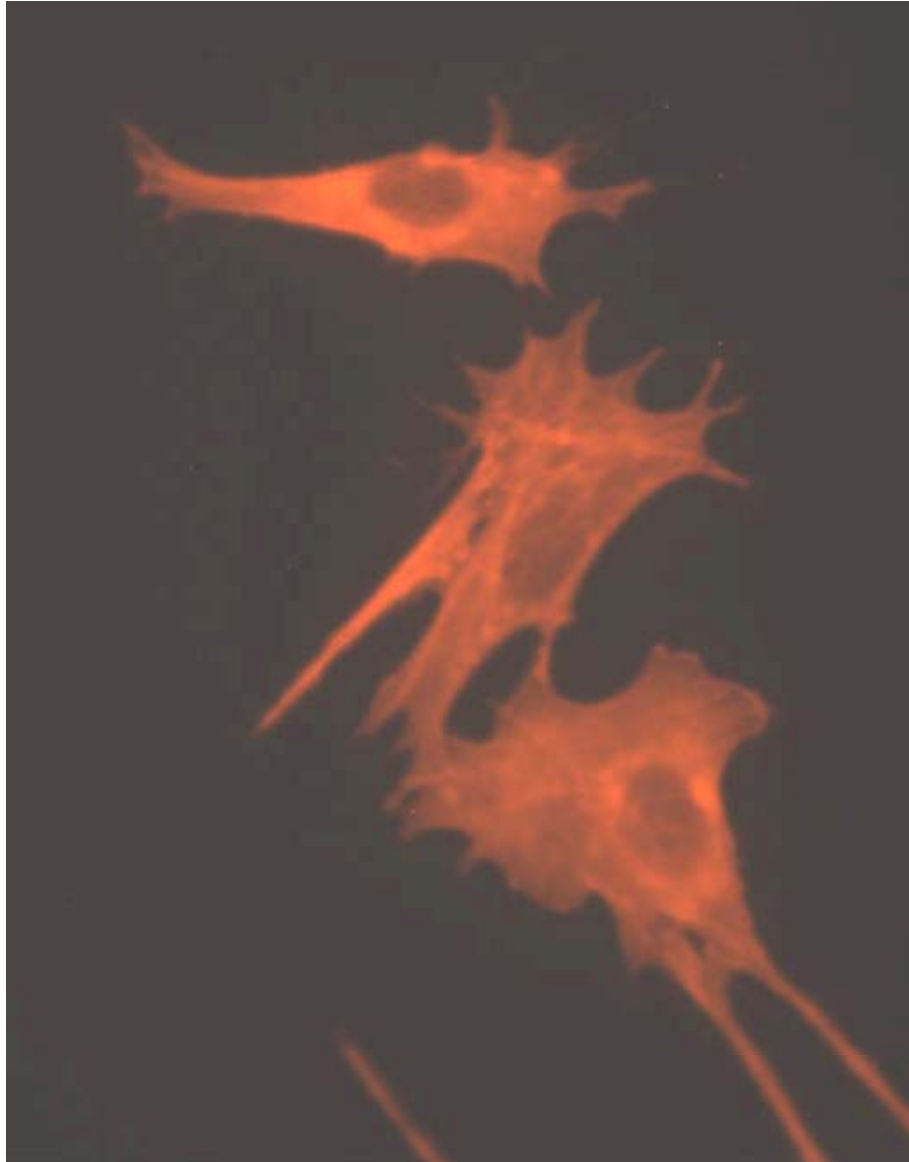
Figure 1.14. Fibroblasts. (3T3 L1) stained with RP fluorescent dye; ~70microns in length (WMAsh, NSF GEM4, UIUC 6/09)

evanescent wave phase shift holography. Subsequent processing by digital holography allows for quantitative phase imaging and measurement of the sample features' surface profile based on assumptions of the objects structure and composition.

TIRHM imaging makes use of the 'total' internal reflection, meaning that essentially all of the input photons participate in the formation of the image signals, and therefore the input optical power can be kept at minimal level. We have demonstrated a Mach-Zehnder TIRHM system that uses a prism in TIR as a near-field imager in its object arm. We have demonstrated these imaging principles of TIRHM using model objects of liquid droplets and spherical surface of known material and shape, and the results indicate distinct capabilities and potential strengths in biomedical cellular microscopy and other applications. System implementation of hardware and software, it's imaging modes, and our results for Amoeba Proteus, Dictyostelium Discoideum myxamoeba, SKOV-3 ovarian cancer, and 3T3 Fibroblast cells are also presented.

The TIRHM system has undergone evaluation of critical performance parameters, displaying a resolution capability nearly inherent to that of the microscope objective used. We find this new technique described herein, total internal reflection holographic microscopy (TIRHM), to be an inherently quantitative tool and offer it as a means of measuring surface profiles with direct applicability in characterizing cellular adhesion and migration, as well as other biomedical applications and 'nanometrics' in general. Based upon this performance, it is fully anticipated that near term applications include measurement of cellular adhesion and motility attributes, particularly those important to

understanding embryogenesis, morphogenesis and cancer metastasis, without the need to introduce stains or fluorophores.

I have attempted to organize this dissertation in as logical and familiar a fashion as possible. After a sufficiently rigorous development of TIRHM theory from first principles, I will discuss the experimental methods in detail and present all of the pertinent results to date. Following the experiments is a discussion of important principles, what conclusions we can draw from this research, and the promise of future work. It is hoped that the reader will largely agree with the findings herein and perhaps choose to encourage investigation in complementary efforts.

CHAPTER 2

THEORY

The theory behind digital holography is well understood and characterized. Furthermore, we have demonstrated that it is possible to couple phase information from a near field evanescent sensing wave produced by Total Internal Reflection (TIR) into the object beam signal of a holographic imager and that the digital holography of total internal reflection is described by Fresnel reflection theory as anticipated. In our cellular imaging application here, the presence of focal adhesions and cell-substrate interfaces on the prism's sensing face cause relative refractive index (RRI) phase shifts and frustrated TIR (f-TIR) that modulates the object beam's evanescent wave phase front thus producing a form of quantitative phase microscopy.

2.1 Total Internal Reflection (TIR)

From Snell's Law, it is well known and characterized that when light is incident from inside of a higher-index medium n_1, into a lower-index medium n_2, with an angle of incidence greater than the *critical angle* given by $\theta_c = \sin^{-1}(n_2/n_1)$, the incident light is

reflected back into the first medium. The TIR effect may be easily viewed while submerged under water and looking back up at the surface at an angle, for instance.

Under TIR, light does not propagate into the second medium except for an evanescent wavefield, whose amplitude decays exponentially over a distance a fraction of a wavelength ($\sim \lambda / 3$). If another medium, n_{cell} is present (as in Fig. 2.1), we shall see that a form of frustrated TIR (f-TIR) can take place.

This 'evanescent' exponentially decaying wave field is set up in order that the electromagnetic fields remain continuous at the interface, extends into the second medium and propagates parallel to the interface. The phase shift and reflectance variations are effective within the penetration depth of about, or about 200 nm if we use 600 nm light. The phase variation therefore can be used to make precise measurements of the interface thickness and characteristics within a few hundred nm. Note that the phase profile of light reflected from an object can be readily obtained by digital holography, a unique and powerful capability that digital holography enjoys over other techniques.

An understanding of total internal reflection (TIR) as described by Fresnel reflection theory is instrumental in seeing how interactions in the resultant near-field modulate the phase of the incident light. It is this phase modulation that, when coupled with digital holographic microscopy, allows for the quantitative near-field phase microscopy of TIRHM. Consider reflection of light, of vacuum wavelength λ_0, across a boundary between two dielectric media with indices n_1 and n_2. The reflection coefficients are given
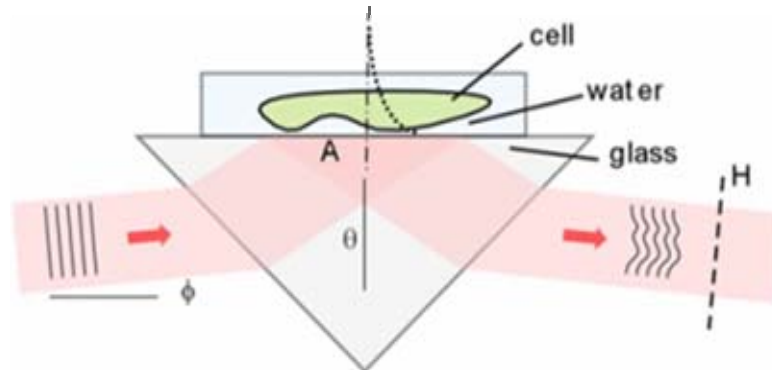
Fig. 2.1 Geometry of TIR evanescent wave surface sensing. When an evanescent wavefront (dotted line ····) is formed at suitable glass-air interface, angle of incidence $\theta_i > \theta_c$, a "TIR frustrating" (f-TIR) sample surface (n_{cell}) introduces optical path difference information as a phase shift. **A** is the plane of the prism sensing face, **H** is the hologram plane. **Note: the evanescent field is NOT to scale.**

by the familiar Fresnel equations:

$$r_\perp = \frac{n_1 \cos\theta_1 - n_2 \cos\theta_2}{n_1 \cos\theta_1 + n_2 \cos\theta_2}; \qquad r_\parallel = \frac{n_2 \cos\theta_1 - n_1 \cos\theta_2}{n_2 \cos\theta_1 + n_1 \cos\theta_2} \qquad (2.1.1)$$

for the s-polarization ($r_\perp$) and the p-polarization ($r_\parallel$), respectively. For internal reflection,

$n_1 > n_2$, if the angle of incidence θ_1 is larger than the critical angle $\theta_c = \sin^{-1}(n_2/n_1)$, then

the reflectance $R = |r|^2$ becomes unity in total internal reflection (TIR) and $\cos\theta_2$ is

imaginary. Defining

$$h_2 = n_2 \cos\theta_2 = i\sqrt{n_1^2 \sin^2\theta_1 - n_2^2} = i\eta_2 \qquad (2.1.2)$$

the reflection coefficients become complex:

$$r_\perp = \exp(-2i\varphi_\perp); \quad \varphi_\perp = \tan^{-1}\frac{\eta_2}{n_1 \cos\theta_1} = \tan^{-1}\frac{\sqrt{n_1^2 \sin^2\theta_1 - n_2^2}}{n_1 \cos\theta_1} \qquad (2.1.3)$$

$$r_\parallel = \exp(-2i\varphi_\parallel); \quad \varphi_\parallel = \tan^{-1}\frac{n_1\eta_2}{n_2^2 \cos\theta_1} = \tan^{-1}\frac{n_1\sqrt{n_1^2 \sin^2\theta_1 - n_2^2}}{n_2^2 \cos\theta_1} \qquad (2.1.4)$$

There is no propagating wave in transmission, but a thin layer of evanescent wave exists

that decays exponentially, $E_t \propto \exp(-k_0\eta_2 z)$, where $k_0 = 2\pi/\lambda_0$ and z is the distance

from the interface. Figure 2.2 (a) shows the reflectance $R = |r|^2$ vs. angle of incidence θ_1,

while Fig. 2.2 (b) is the reflection phase φ vs. θ_1 for the relative index $n_1/n_2 = 1.517$. One

34

notes the Brewster angle at 33° and the critical angle at 41°.

While the reflection phase is only zero or 180° for non-TIR Fresnel reflection, beyond the critical angle the reflection phase decreases continuously and monotonically from 0 to −180° for both cases of polarization. Figure 2.2 (c) illustrates the reflection phase of s-polarization for a few values of the relative index, with $n_1 = 1.517$ and 1.000, $n_2 = 1.333$, 1.382, 1.432, and 1.458. Here the n_1 value represents the BK7 glass prism and the n_2 values are for air, water, 50/50 mixture of water and ethylene glycol, pure ethylene glycol, and fused quartz, respectively, which are the materials used in the measurements below. For a given angle of incidence, for example 72° shown as dotted line in Fig. 2.2 (c), the phase of TIR-reflected light will vary with n_2 the index of refraction of the second medium. This suggests one possible mode of TIR imaging, where the phase profile of the TIR-reflected light reveals the variation of index of refraction of material in contact with the prism.

Another imaging mode makes use of the frustrated TIR (fTIR) that occurs when a third layer of index n_3 is brought close to the interface within the thickness of the evanescent wave. (Here we use the term frustrated TIR in a general sense that includes any disturbance, in amplitude or phase, of TIR by the presence of another interface within the evanescent field.) Referring to the geometry of Fig. 2.3, light is incident from the n_1 medium and undergoes reflection at the two interfaces, n_1/n_2 and n_2/n_3.

a)   b)   c)
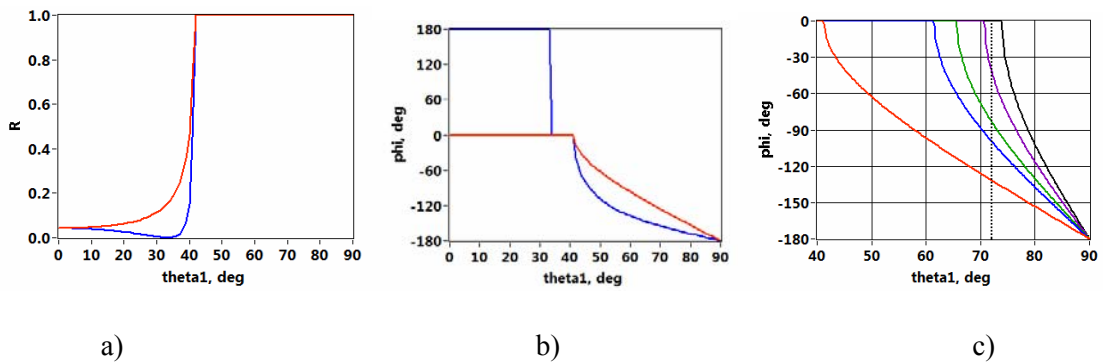
Fig. 2.2. a) Reflectance R and b) reflection phase, phi (φ in text) vs. angle of incidence, theta1 (θ_1 in text)   for the relative index, $n_1/n_2 = 1.517$. [red: s-polarization; blue: p-polarization] c) Reflection phase of s-polarization vs. angle of incidence for various relative indices: $n_1 = 1.517$; $n_2 = 1.000$ (red), 1.333 (blue), 1.382 (green), 1.432 (purple), 1.458 (black).

The reflection coefficient, for s-polarization, is found to be

$$r_\perp = \left(\frac{E_1'}{E_1} \right)_\perp = \frac{(h_1 - h_2)(h_2 + h_3) + (h_1 + h_2)(h_2 - h_3)\exp(2i\varphi_0 h_2)}{(h_1 + h_2)(h_2 + h_3) + (h_1 - h_2)(h_2 - h_3)\exp(2i\varphi_0 h_2)} \tag{2.1.5}$$

where $h_i = n_i \cos\theta_i = \sqrt{n_i^2 - n_1^2 \sin^2\theta_1}$ and $\varphi_0 = k_0 z_0$. For illustration, if we take $n_1 = 1.517$

(glass), $n_2 = 1.000$ (air), and $n_3 = 1.458$ (quartz), then the critical angles for the n_1/n_2 and

n_1/n_3 interfaces are $\theta_{c,12} = 41°$ and $\theta_{c,13} = 74°$, respectively.

The reflectance $R = |r|^2$ and reflection phase φ are graphed in Figs. 2.4(a) and 2.4

(b), respectively, as two-dimensional functions of the angle of incidence θ_1 and the n_2-

layer thickness z_0. Figure 2.4(c) is an expanded view of the dotted-box area of Fig.

2.4(b), showing details of the subtle and rapid variation of phase over a short distance of

z_0. Figures 2.4(d) and 2.4(e) are graphs of $R(z_0)$ and $\varphi(z_0)$, respectively, for several

values of θ_1. Figure 2.4(f) is an expanded view of the dotted-box area of Fig. 2.4(e). As

indicated in Fig. 2.4, there are three distinct ranges of θ_1 for consideration:

Case I: When $\theta_1 < \theta_{c,12}, \theta_{c,13}$, r is real and both the reflectance and reflection phase display

the oscillatory characteristics of thin film interference, as shown in Fig. 2.4 for $\theta_1 < 41°$.
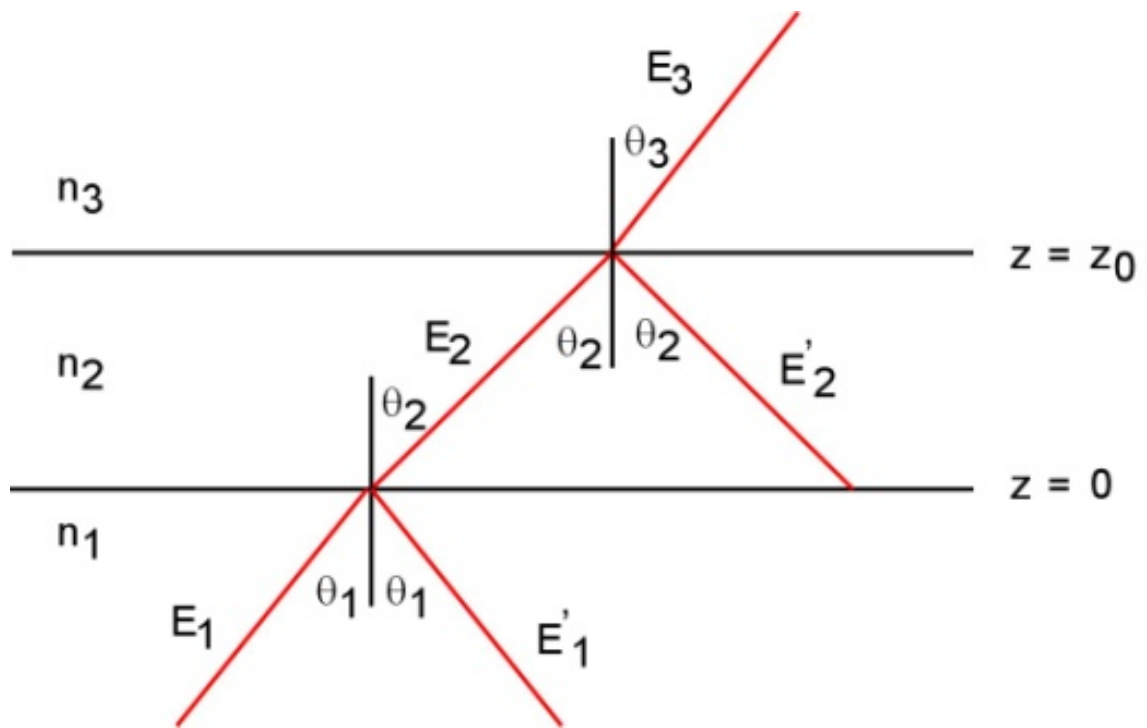
Fig. 2.3 Geometry of frustrated TIR (fTIR).

Case II: When $\theta_{c,12} < \theta_1 < \theta_{c,13}$, the n_1/n_2 interface is in TIR ($h_2 = i\eta_2$ becomes imaginary), but the n_1/n_3 interface is not, and the overall reflection coefficient becomes

$$r_\perp = \left(\frac{E_1'}{E_1}\right)_\perp = \frac{(h_1 - i\eta_2)(i\eta_2 + h_3) + (h_1 + i\eta_2)(i\eta_2 - h_3)\exp(-2\varphi_0\eta_2)}{(h_1 + i\eta_2)(i\eta_2 + h_3) + (h_1 - i\eta_2)(i\eta_2 - h_3)\exp(-2\varphi_0\eta_2)} \qquad (2.1.6)$$

This is the conventional narrow definition of fTIR, where the evanescent field couples into the third medium and becomes a propagating field. For sufficiently short z_0, a fraction of wavelength, the reflectance is substantially reduced and the reflection phase varies monotonically with z_0, as shown in Fig. 2.4 for $41° < \theta_1 < 74°$. This is the regime where 'conventional' TIR imaging methods operate, such as TIR fluorescence microscopy, making use of the amplitude changes in fTIR. Amplitude images can also be obtained using digital holography such that outlines of an object in contact on the surface

appear as dark areas against bright background, and the darkness would be a measure of the layer thickness z_0.

Case III: It is possible to make use of phase-only changes in fTIR if the angle of incidence is large enough for TIR of both n_1/n_2 and n_1/n_3 interfaces, $\theta_{c,12}, \theta_{c,13} < \theta_1$. Then
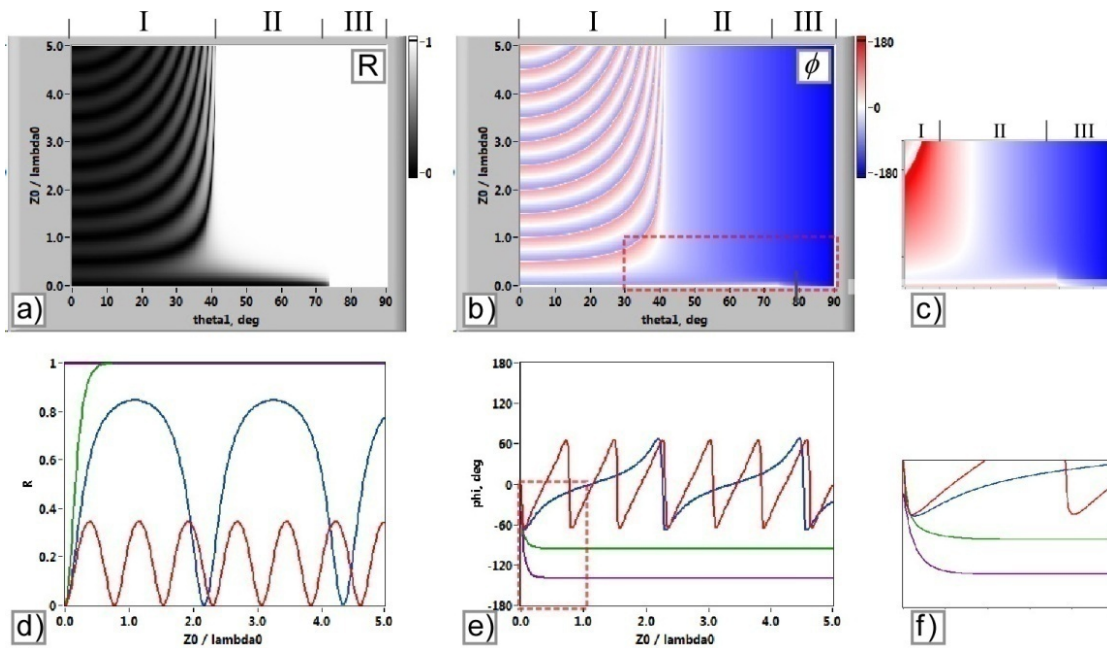
Fig. 2.4 Reflectance and reflection phase in fTIR, for s-polarization with $n_1 =$ 1.517, $n_2 = 1.000$, and $n_3 = 1.458$. a) Reflectance R vs. the angle of incidence, theta1 (θ_1 in text) and the n_2-layer thickness z_0. b) Reflection phase, phi (φ in text) vs. theta1 (θ_1 in text) and z_0. c) Expanded view of the dotted-box area of b). d) Cross-sections of a) at theta1 = 30° (red), 40° (blue), 60° (green), and 75° (purple). e) Cross-sections of b) at several values of theta1 (θ_1 in text) as in d). f) Expanded view of the dotted-box area of e).

$h_3 = i\eta_3$ also becomes imaginary and

$$r_\perp = \left(\frac{E_1'}{E_1}\right)_\perp = \frac{(h_1 - i\eta_2)(\eta_2 + \eta_3) + (h_1 + i\eta_2)(\eta_2 - \eta_3)\exp(-2\varphi_0\eta_2)}{(h_1 + i\eta_2)(\eta_2 + \eta_3) + (h_1 - i\eta_2)(\eta_2 - \eta_3)\exp(-2\varphi_0\eta_2)} \qquad (2.1.7)$$

Then the reflectance R is identically unity. But in this case, the phase varies with θ_1 and z_0, as seen in Fig. 2.4 for $74° < \theta_1$, where for z_0 less than a fraction of wavelength, the phase varies monotonically and rapidly. This can be used to provide a sensitive measure of the thickness of the n_2-layer over a range of 100 nm or less.

This suggests one possible mode of TIR imaging, where the phase profile of the TIR-reflected light reveals the variation of index of refraction of material in contact with the prism (Figure 2.5a). On the other hand, it is possible to make use of phase-only changes in fTIR if the angle of incidence is large enough for TIR of both n_1 / n_2 and n_1 / n_3 interfaces. Then the reflectance R is identically unity. But the phase does vary with θ_1 and d, where for d less than a fraction of wavelength, the phase varies monotonically and rapidly. This can be used to provide a sensitive measure of the thickness of the n_2-layer over a range of 100 nm or less.

So we see that two imaging modes of total internal reflection are possible, based on quantitative phase microscopy by digital holography. In one (Figure 2.5a), the reflection phase profile results from variation of refractive index of an object of inhomogeneous optical property in contact with the prism.
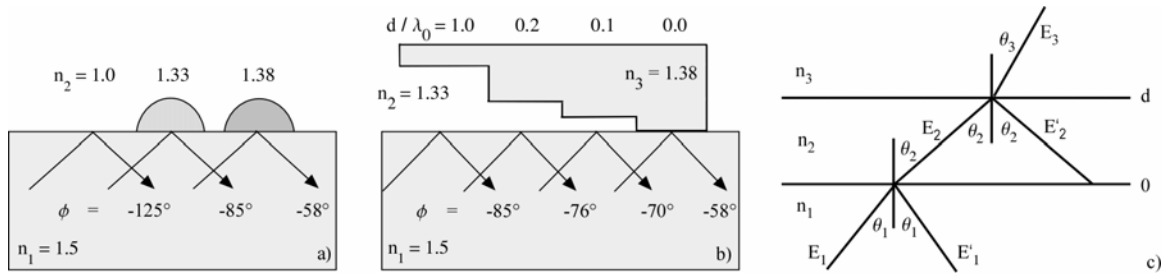
Figure 2.5. TIR Phase shift, φ, due to Fresnel reflection for an angle of incidence, $\theta_1 = 72°$ (TIRHM imaging modes), $n_1=1.5$ is the glass TIR prism; a) relative index profile, b) fTIR thickness profile, c) geometry of frustrated TIR. d/λ_0 is the ratio of distance of the n_1-n_3 gap in the fTIR case to the operating wavelength of the laser source. In 2.5c), the E and θ are for reflections and transmission between materials of refractive indices n_1, n_2 and n_3 separated a distance, d.

42

For example, as in Figure 2.5a), a phase profile between air (n=1.00) and a water

droplet (n=1.33) on the prism surface $(n_1=1.5, \theta_1 = 72°)$ would show a shift in reflected

phase from $\varphi_{air/n1} = -125°$ to $\varphi_{water/n1} = -85°$ or $\Delta\varphi = \varphi_{water/n1} - \varphi_{air/n1} = -85° - (-125°) = 40°$

(or 0.7 radians) across the air water boundary on the prism surface. A biological cell

(n=1.38), for example, in complete contact with the prism surface can thus be imaged to

reveal it's interface with the prism substrate. In the other mode (Figure 2.5b), the

reflection phase profile reflects the gap distance between the surfaces of the prism and an

object placed on the prism. For example, a biological cell in locomotion can reveal the

profile of protrusion of pseudopodia, formation of focal adhesion, development of

traction, and release of adhesion.

2.2 The principle of digital holography; the Angular Spectrum Method

As the basis for digital holography, numerical diffraction may be described the

Huygens Convolution, the Fresnel Transform method and the angular spectrum method

(ASM). The digital holographic technique used in this work is based upon the Angular

Spectrum Method, synonymously (and aptly) termed 'plane wave decomposition'. In

ASM, the holographic image is numerically converted into Fourier space, filtered and

reconstructed at the appropriate distance (to be in focus, for instance). The calculation of

the optical field as an array of complex numbers directly yields the phase profile of the

object signal as a monotonic function. ASM inherently lends itself to performing the un-

tilting processing as part of the algorithm.

There are a number of advantages in using the angular spectrum algorithm over

the more commonly used Fresnel transform or the Huygens convolution methods; they

are consistent pixel resolution, no minimum reconstruction distance, easy filtering of

noise and background components and computational efficiency. Once the angular

spectrum at $z = 0$ is calculated by a Fourier transform, the field at any other z-plane can

be calculated with just one more Fourier transform, whereas the Fresnel or convolution

methods require two or three Fourier transforms for each value of z. The theory behind

digital holography is well understood and characterized, particularly for the Angular

Spectrum Method (ASM).

Specifically, suppose $E_{\Sigma 0}$ (x, y) represents the two-dimensional optical E-field at

the hologram plane Σ_0 which we wish to filter and propagate to the image plane Σ. Given

an input field $E_{\Sigma 0}$ (x, y) from the CCD hologram, the input spectrum is:

$$F_{\Sigma_0}(k_x, k_y) = \mathcal{F}\{ E_{\Sigma_0} \} = \iint dx dy E_{\Sigma_0}(x, y) \exp[-i(k_x x + k_y y)] \qquad (2.2.1)$$

Where k_x and k_y are the spatial frequencies and $k = 2\pi/\lambda$. The input field of course comes

back out with the inverse Fourier transform as:

$$E_{\Sigma_0}(x, y) = \mathcal{F}^{-1}\{ F_{\Sigma_0} \} = \iint dk_x dk_y \, F_{\Sigma_0}(k_x, k_y) \exp[i(k_x x + k_y y)] \qquad (2.2.2)$$

Written in terms of plane wave components:

$$\psi = \exp i[\vec{k}\cdot\vec{r}] = \exp[\ i(k_x x + k_y y + k_z z)] \qquad (2.2.3)$$

where

$$k_z = [k^2 - k_x{}^2 - k_y{}^2]^{\frac{1}{2}} = k_z\ (k_x, k_y) \qquad (2.2.4)$$

Such that a plane wave on Σ_0 looks like:

$$\psi_{\Sigma_0} = \psi(z = 0) = \exp[\ i(k_x x + k_y y)] \qquad (2.2.5)$$

and a plane wave on Σ can be expressed as:

$$\psi_{\Sigma} = \psi(z = Z) = \exp i(k_x x + k_y y + k_z Z)] = \psi_{\Sigma_0}\exp i[k_z Z] \qquad (2.2.6)$$

The output field at Σ is now :

$$E_{\Sigma}(x,\ y) = \iint dk_x dk_y\ F_{\Sigma_0}(k_x,\ k_y)\ \exp i[k_z Z]\exp[i(k_x x + k_y y)] = \mathcal{F}^{-1}\{\ F_{\Sigma}\} \quad (2.2.7)$$

with the anticipated efficiency in transform calculations. Furthermore, we will take advantage of this inherent topology of the ASM when we proceed to image the inclined plane imposed by the TIR sensing geometry. One of the reasons ASM is used in this

45

research is due to its algorithmic utility; the angular spectrum method allows the reconstruction software to compensate for tilt anamorphism due to the inclined TIR plane.

2.3 Digital holography on inclined plane: numerical diffraction to an inclined plane

Because of the TIR prism's geometry (Figure 2.6b), the imaging face is at a sizeable incline with respect to the hologram plane so an en face reconstruction result requires an algorithm that accounts for such an "anamorphism". From the numerical array that represents the hologram, the image of the optical field at plane Σ' (A) is calculated by numerical diffraction of the optical wave from Σ_0 (H) to Σ' (A). Now the object plane Σ' is inclined at a large angle with respect to the hologram plane Σ_0, which requires a special reconstruction algorithm. Its Fourier transform gives the angular spectrum, or the plane wave decomposition of the input field, just as in non-inclined case considered in previous section: To see this analytically, let the field at the input plane Σ_0 be $E_{\Sigma_0}(x, y, 0)$. Its Fourier transform, F_{Σ_0}, then gives the angular spectrum, or the plane wave decomposition of the input field, just as in non-inclined case of ASM.

As before, consider a plane wave as in figure 2.7b on Σ', namely $\psi_{\Sigma'}$ (x' ,y', z' = 0). The transformation with rotation solely around the y-axis is simply;

$$\begin{bmatrix} x \\ y \\ z-Z \end{bmatrix} = \begin{bmatrix} \cos\beta & 0 & \sin\beta \\ 0 & 1 & 0 \\ -\sin\beta & 0 & \cos\beta \end{bmatrix} \begin{bmatrix} x' \\ y' \\ z' \end{bmatrix} = \begin{bmatrix} x'\cos\beta + z'\sin\beta \\ y' \\ -x'\sin\beta + z'\cos\beta \end{bmatrix} \qquad (2.3.1)$$

46

so,

$$\psi_{\Sigma'} = \exp i[k_x x + k_y y + k_z z]\big|_{\Sigma'}$$
$$= \exp i[k_x(x'\cos\beta) + k_y y' + k_z(Z - x'\sin\beta)] \qquad (2.3.2)$$
$$= \exp i[(k_x\cos\beta - k_z\sin\beta)x' + k_y y']\exp i[k_z Z]$$

And the output field on Σ' is just:

$$E_{\Sigma'}(x', y') = \iint dk_x dk_y F_{\Sigma_0}(k_x, k_y)\psi_{\Sigma'}$$
$$= \iint dk_x dk_y F_{\Sigma_0}(k_x, k_y)\exp i[(k_x\cos\beta - k_z\sin\beta)x' + k_y y']\exp i[k_z Z] \qquad (2.3.3)$$
$$= \int dk_y \exp i[k_y y']\int dk_x F_{\Sigma_0}(k_x, k_y)\exp i[(k_x\cos\beta - k_z\sin\beta)x']\exp i[k_z Z]$$

Where

$$F_{\Sigma_0}(k_x, k_y) = \iint dxdy E_{\Sigma_0}(x, y)\exp[-i(k_x x + k_y y)]] \qquad (2.3.4)$$

is simply the Fourier transform of the field at the input plane, Σ_0.

Recombination of the plane wave components at the output plane then yields the resultant diffraction field in an integration over k_x which in general is not a Fourier transform, and therefore can be handled by direct summation of the array, whereas the integration over k_y is an inverse Fourier transform and therefore fast Fourier transform (FFT) is available. The algorithm provides exact (non-approximated) results with a reasonable compromise in computation speed.

Numerical diffraction on to an inclined plane has been attempted with several techniques [52-54], but since existing algorithms are either very slow or provide only approximate solutions for small inclination angles, we have developed this more general
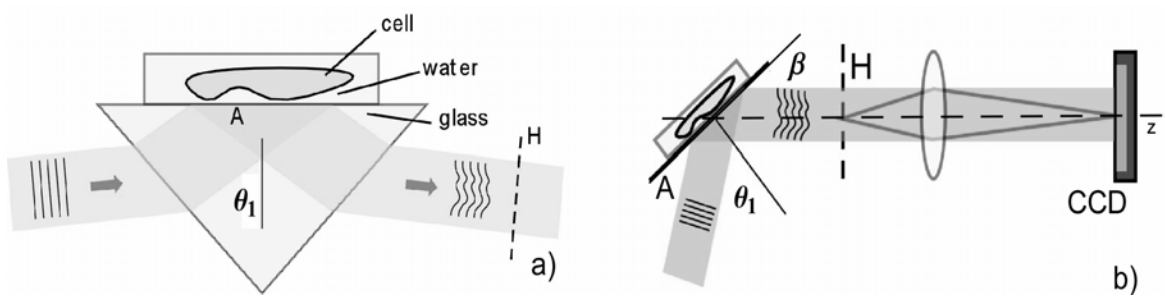
Figure 2.6 TIRHM prism Geometry. a) TIR prism with object beam and aqueous cellular sample; the object beam enters the TIR prism from the left. The near field from object beam TIR interacts with the sample thus modulating the resulting hologram phase profile. b) Optical path geometry depicting the CCD camera imaging of the hologram. A designates the prism interface plane, H is the hologram plane, θ_1 is the angle of incidence, β is the tilt plane angle with respect to the optical axis, z, and CCD is the Charged Coupled Device camera.

angular spectrum algorithm. The Angular Spectrum Method (ASM) of digital holography is used in this technique is due to its algorithmic utility; among its other strengths, the angular spectrum method allows the reconstruction software to compensate for tilt anamorphism due to hypotenuse face/TIR plane inclination and prism optical path.

Figure 2.8 is offered as a conceptual representation of how TIRHM images cellular adhesion in the near-field. The adhesion is formed by components of cellular membrane, here depicted as a phospolipid bilayer, in the range of the near field where phase shifts due to RRI and f-TIR field modulation are carried forward by the object beam

into the hologram. When the hologram is reconstructed numerically the phase information becomes available for the production of a phase image of the substrate-adhesion interface.
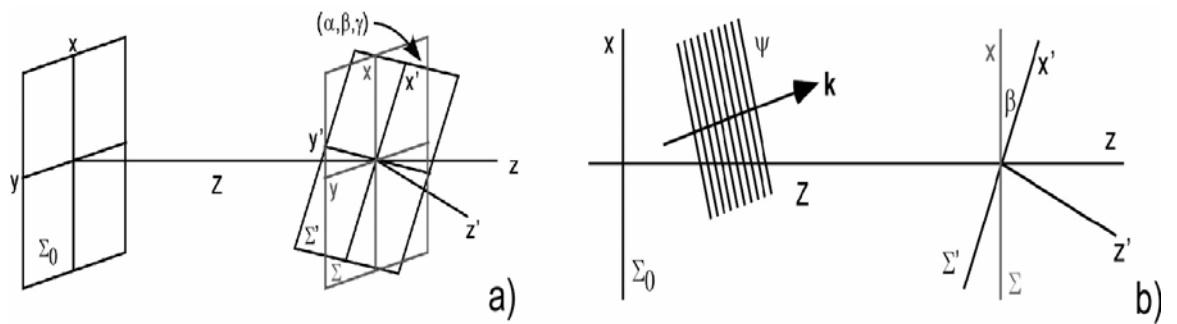
Figure 2.7. Geometry of holography over an inclined plane. a) General coordinate system with input plane $\Sigma 0$ and output planes Σ (unrotated) and Σ' (rotated). b) Coordinate system for general rotation around y-axis only: $\alpha = \gamma = 0$, $\beta \neq 0$.

CHAPTER 3

EXPERIMENTAL SETUP

One can imagine how this research progressed over the years from January of
2007 to the Spring of 2010. The system itself can broadly be understood as an initial
breadboard unit (System I) which, as a result of lessons learned by empirical
implementation of theory, eventually matured into a cage-based unit pinned to a vertical
plate (System II). Table 3.3 is included at the end of this chapter depicting milestones of
significance in the project's timeline.

3.1 TIR Prism

The heart of the TIRHM system is its prism upon whose hypotenuse face the
sample rests. (Please see Figure 3.1) The object beam enters a short face, goes into TIR
at the hypotenuse face setting up the near field and reflecting to exit the second short
face. The interferometer and all fixturing are built around the prism to keep it positioned
horizontally in the object beam at the correct angle of incidence allowing the hologram to
be created, modulated by the TIR near-field and imaged by the CCD camera. Note that

Figure 3.1 TIR Prism. On the left is a 12.7mm (hypotenuse 17.5mm) right angle BK7 glass (n = 1.517) unit, Melles Griot Part Number #01 PRS 011. (Unit 2) At right is a truncated 15.00 mm (Hypotenuse 21.00mm) right angle SFL11 glass (n = 1.785) unit, made from Edmund part number NT45-950- Scribelines for prism alignment are barely visible on the upfacing hypotenuse of the SFL11 unit.

there is a minimum requirement of $\theta_1 > \theta_{critical}$ as depicted in Table 3.1 in order to

maintain the TIR condition.

      Two types of prisms were used in this work. Initially, early on, a 25.4mm

(hypotenuse 35mm) right angle BK7 glass (n = 1.517) lab unit was used, followed by a

smaller 12.7mm (hypotenuse 17.5mm) right angle BK7 glass (n = 1.517) unit (Melles

Griot Part Number #01 PRS 011), and eventually, a 15.00 mm (Hypotenuse 21.00mm)

right angle SFL11 glass (n = 1.785) unit, (Edmund part number NT45-950) was

employed; the higher index of refraction being able to accommodate smaller angles of

incidence and therefore less tilt of the image plane. In order to accommodate illumination

entrance for the LookDown camera (see Section 3.3), the right angle point of the SFL11

prism was truncated down to a polished flat by the Physics Department Machine Shop.

3.2 Interferometer

      In the interest of completeness, it is worth some historical note that this

investigation started, not with the Mach-Zehnder (M-Z) interferometer used for TIRHM,

but with initial practice on the Michelson topology depicted in Figure 3.2. Please note

the progression of instrument designs from the Michelson unit in Figure 3.2, to the

transmission M-Z in Figure 3.3, the System I TIRHM in Figures 3.4 and 3.5, and

eventually the System II configuration in Figure 3.6

      The basic interferometer topology to implement the TIRHM system is depicted in

Table 3.1 Critical Angle (degrees) when entering n_2 from n_1

$\theta_c = \sin^{-1}(n_2/n_1)$			n_2						
			Air	Water	50% EG	Ethylene Glycol	Silica	Glycerol	BK7
			1.0003	1.333	1.382	1.431	1.458	1.473	1.517
n_1	Water	1.333	48.63						
	50% EG	1.382	46.35	m					
	Ethylene Glycol	1.431	44.32	m	m				
	Silica	1.458	43.32	66.10	71.47	79.12			
	Glycerol	1.473	42.78	m	m	m	81.84		
	BK7	1.517	41.25	61.49	65.68	70.71	73.97	76.15	
	SFL11	1.785	34.08	48.31	50.76	53.33	54.77	55.60	58.20

50% E.G. – 50% ethylene glycol aqueous solution

m – miscible

<u>References:</u> 1) Edmund Optics Specifications, 2) Weber [55]

Figure 3.2. The laser source is split into object and reference beams by a device such as a beam cube, BS1. The object beam is brought into the TIR prism by mirror, M1, as described in Figure 3.1. The reference beam is preserved and brought back into superposition with the object beam by mirror, M2, at beam cube, BS2, establishing the hologram at H which is imaged by the camera (CCD).   Optics L_{obj}, L_{img} and L_{ref} are included (as necessary) for magnification and beam front/curvature conditioning.

Figure 3.5 shows a basic configuration of the original System I interferometer for digital holographic microscopy of total internal reflection. A yellow HeNe laser (λ = 594 nm, 2 mW) input beam is split into two parts, object (obj) and reference (ref), by a beam splitter BS1 and recombined at BS2 for superposition, forming a Mach-Zehnder interferometer. The object beam enters the prism and undergoes total internal reflection at the hypotenuse *A* of the right-angle prism. S-polarization is used in the imaging experiments.

The presence of a specimen on the prism surface modulates the phase front of the reflected light. A objective lens L_{obj} (f = 15 mm, NA = 0.4) placed next to the prism projects a magnified image of the hologram plane H on to the CCD camera, through an imaging optics L_{img}. Another lens L_{ref} is placed in the reference arm so that the two beams have matching wavefront curvatures. The CCD camera (SONY XCD-X710CR, 1034 x 779 pixels, 4.65 x 4.65 μm^2 per pixel) acquires an image of the hologram plane H (which is usually taken in close vicinity of the object plane A) in superposition with the reference beam. A set of programs developed in-house using LabVIEW® calculates propagation of the optical field back to the object plane *A*. Because of the presence of the prism, the object plane A
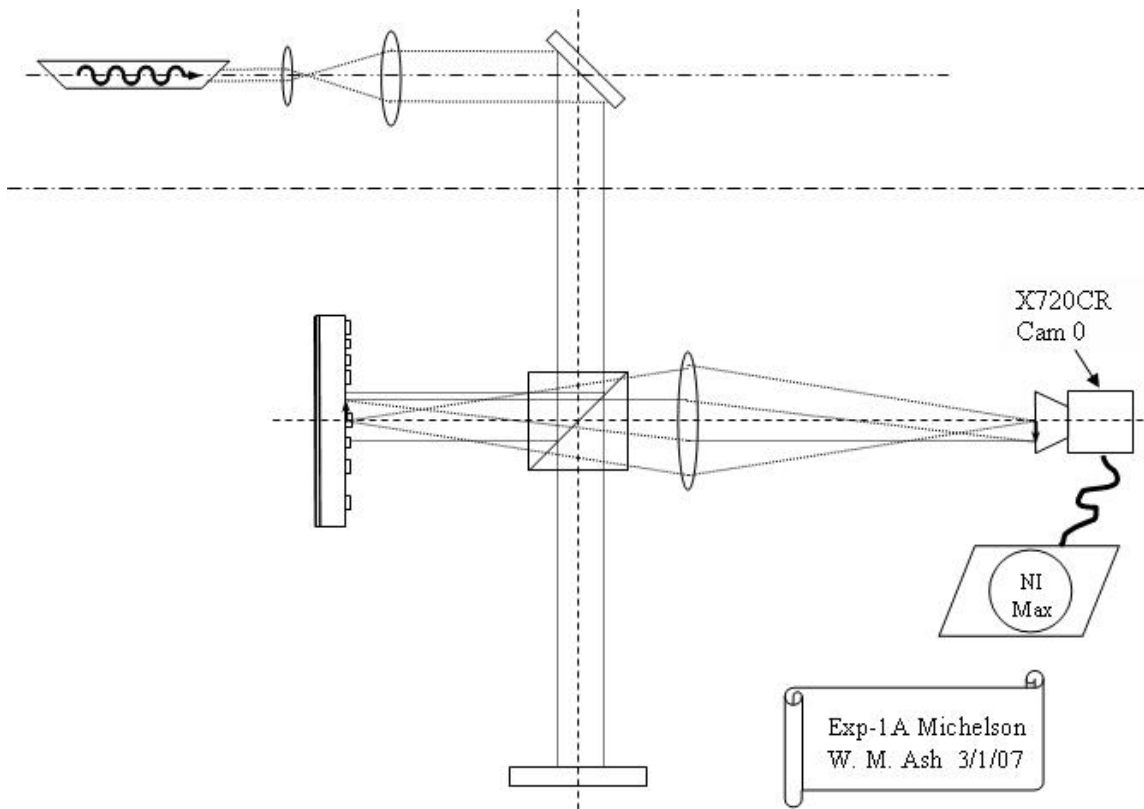
Figure 3.2 Michelson interferometer. (As in original lab notes). A 2 mW HeNe laser at 594nm is expanded and introduced into a Michelson beam cube splitter with a resolution target in reflection. The resulting hologram is sensed by a Sony X720CR CCD FireWire™ camera controlled by National Instruments Measurement Explorer (NI MAX) software running on a personal computer.

optically appears to the camera, or to the plane H, at about 72° angle of inclination, which causes a large difference (about 1:3) in the x- and y-scales of images presented below. (This angle is only coincidentally of same numerical value as θ_1 below.)

The System II TIRHM apparatus configuration is depicted in Figure 3.6. Note that the TIR prism is mounted into a three axis micrometer translation stage with hypotenuse horizontal to the breadboard. The System II laser source is a Coherent DPSS producing 40mW at $\lambda = 532$nm fiber coupled into a single mode 50:50 fiber splitter (Thorlabs FC632-50B-FC 2x2; instead of a more traditional beam cube splitter). The fiber splitter feeds the expander/ collimators (BE $_{OBJ/REF}$) for both the object and reference arms. The object beam is incident upon the TIR prism, interacts with the TIR face and the sample in the near field, reflects, and is imaged onto the CCD camera by microscope objective MO$_{OBJ}$. In order to produce the hologram, the reference beam is brought into superposition by a 1" beam cube, B/C, acting as a combiner. The system is also polarized to aid in balancing beam intensity levels in superposition at the CCD camera.

Built on a 30mm Thorlabs cage system with 1" optics, the unit is mechanically pinned to a vertical plate with the sample sitting atop the TIR prism; the objective beam entering and exiting from underneath. Two types of microscope objectives for MO$_{OBJ}$ and MO$_{REF}$ are currently in use with the TIRHM; a 10x/0.25 Edmund μPlan and a 25x/0.40 LWD (Long Working Distance) UNICO plan, whose working distances are 10mm and 5mm, respectively. Note that continual hardware upgrades were incorporated.
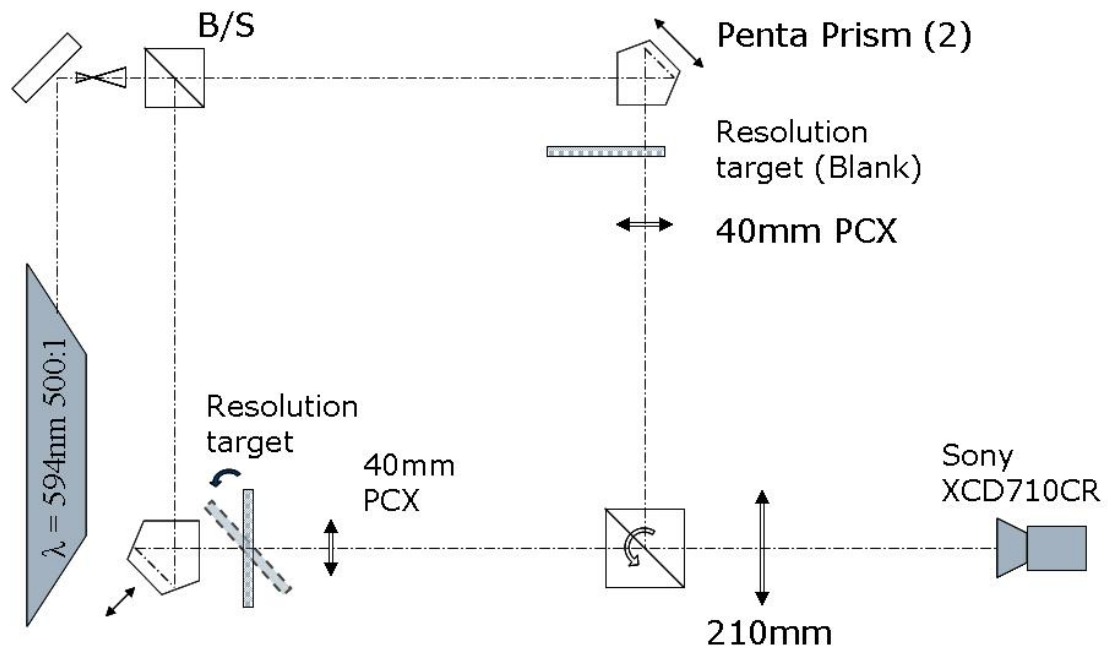
Figure 3.3 Ex2 layout - Resolution target tilt BS – beam splitter/beam cubes, PCX-plano convex lens, Sony CCD – charge coupled device camera, beam expander 1:7 actual system, these elements are incorporated with off-the-shelf (OTS) microscope objectives.
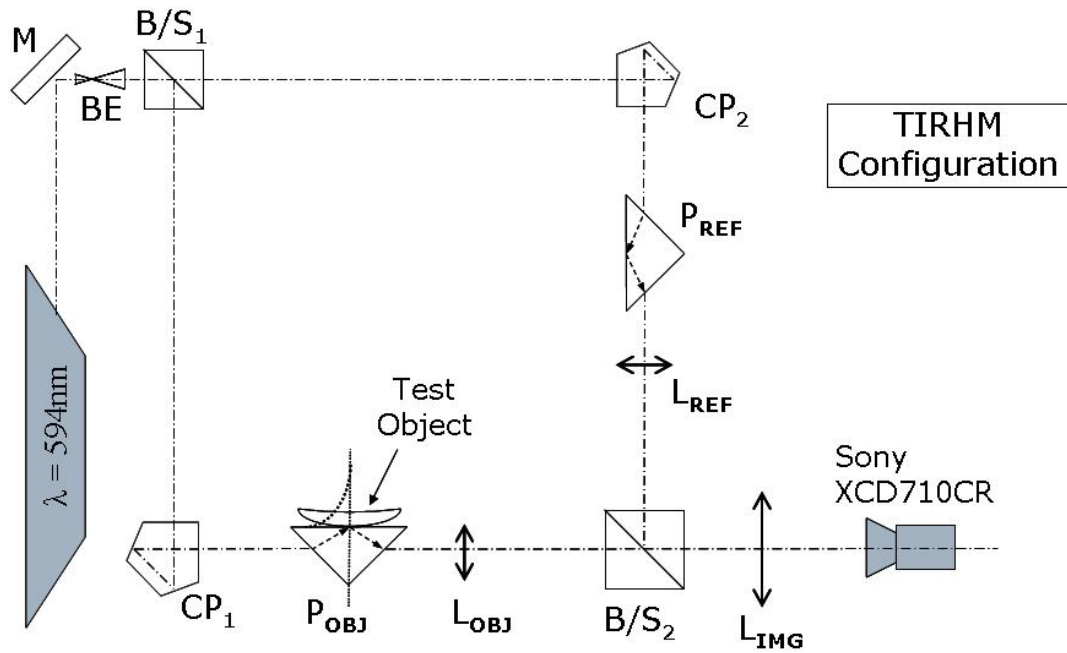
Figure 3.4 Mach-Zehnder TIRHM topology showing lens experiment . BE -beam

expander 1:7, $BS_{1,2}$ beam cubes, $CP_{1,2}$ Penta prism, P −TIR prism; obj - object beam.

ref – reference beam,. L_{obj} – objective lens, L_{ref} – reference lens, L_{img} – image lens,

CCD – charge coupled device camera
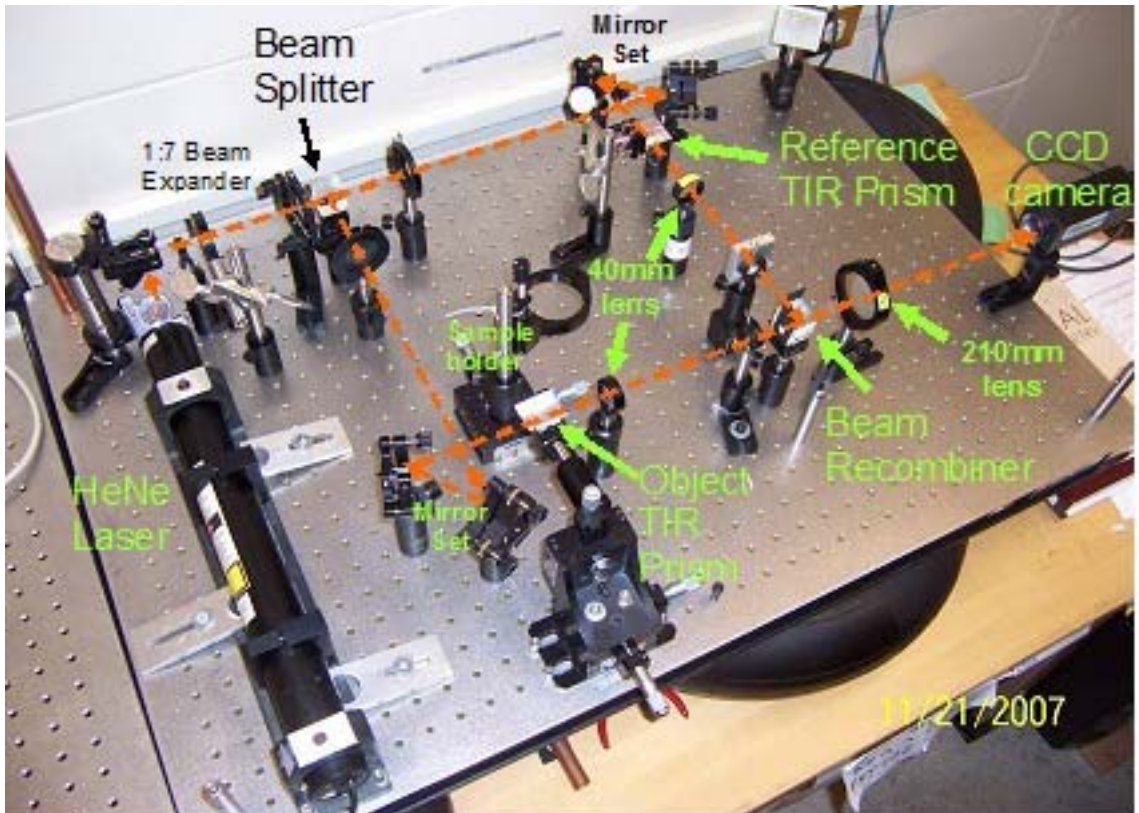
Figure 3.5 Original system. (System I) Mach-Zehnder interferometer for

digital holography of total internal reflection. Here the pentas are replaced by

figure-of-4 mirrors for noise reduction.

3.3 Camera and Image Acquisition

The CCD camera used to acquire the TIRHM hologram is a SONY FireWire CCD camera XCD-X710CR, with 1034 x 779 pixels (horizontal x vertical), 4.65 x 4.65 μm^2 per pixel. To process the hologram, the CCD camera digitally images the hologram to a Firewire card installed in a Dell personal computer platform which also runs the camera drivers, support routines and numeric processing algorithms.

A second SONY Firewire camera is mounted directly over the TIR prism and pointed down at the hypotenuse face. Termed the "Lookdown camera", it is focused on the same spot that the TIRHM camera is looking up into to provide a direct image for correlation with the TIRHM phase image. The lookdown camera uses either an Edmund 10X/0.25 or 20X/0.40 MO depending on the TIRHM camera magnification and has a super luminescent diode (SLD) for illumination underneath the TIR prism.

Camera setup and alignment is performed with National Instruments Measurement and Automation Explorer (MAX) package which is used to initialize camera settings particularly protocol and shutter speed prior to handoff to the Angular Spectrum Method virtual instrument (vi), named "AAA HoloExpt.vi" . The cameras are set at Format 7, Mode 1, 512 x 384, Mono 16, 400 Mbps with the TIRHM camera designated as "cam1" and the Look Down camera designated as "cam0" by the firmware.

3.4 Computer and Programs Overview

The first computer system, full name U241589.cas.usf.edu, initially used with this

61
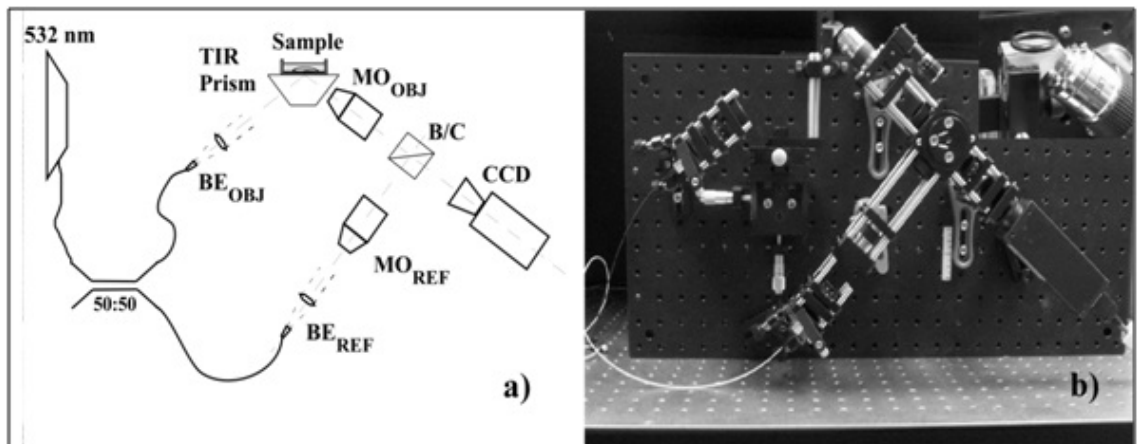
Figure 3.6 System Upgrade (System II) a) Mach-Zehnder TIR digital holographic microscope (DHM) apparatus. 50:50 - fiber optic coupler, $BE_{OBJ/REF}$ – beam expander/collimator (object beam / reference beam), B/C - beam combiner (cube), MO_{OBJ} / MO_{REF} – microscope objective (object beam / reference beam), CCD – charge coupled device camera, b) TIRHM system on vertical plate; TIR prism at apex. Inset: TIR prism close-up showing sample reservoir gasket on prism hypotenuse face. (The lookdown camera perpendicular above the prism hypotenuse face and diode light source below the TIR prism are not shown.)

research is a Dell Optiplex GX280 with an Intel Pentium ® 4 CPU 3.40 Ghz with 1.00

GB of RAM running Microsoft Windows XP Professional Version 2002 Service pack 2.

The Firewire interface card is a Texas Instruments OHCI Compliant IEEE 1394 Host

controller in PCI Slot 3 (PCI bus 4, device 2, function 0). The digital camera interface is

National Instruments NI-IMAQdx IIDC with device driver

C:\WINDOWS\system32\DRIVERS\niimaqdxkw.sys downloaded from NI.

The second computer system, full name C004673.forest.usf.edu, used with this

research is a Dell Optiplex 960 with an Intel® Core™2 Duo CPU E8400 @ 3.00GHz

2.99 GHz with 4.00 GB of RAM (3.25 GB usable) running Microsoft Windows 7

Enterprise. The Firewire interface card is a Texas Instruments OHCI Compliant IEEE

1394 Host controller (PCI bus 4, device 0, function 0). The digital camera interface is

National Instruments NI-IMAQdx IIDC with device driver 3.5.0.49155 at

C:\WINDOWS\system32\DRIVERS\niimaqdxkw.sys. Note that this system was

eventually replaced with the initial system due to software contention.

The LabVIEW software package from National Instruments, Inc. is used for

hologram acquisition and reconstruction, and also for the untilt post processing routine.

This software algorithm is performed in a routine that LabVIEW refers to as "Virtual

Instrument" or ".vi" . A .vi routine can call a subroutine, termed a "sub vi", which allows

for modular software construction and the use of both NI library vi's as well as user

defined vi routines. The specific routine used for digital hologram reconstruction in this

research is called "**AAA HoloExpt.vi**". The primary sub vi's used by AAA HoloExpt.vi

are depicted in Table X and are part of the kimlab electronic software library, in this

instance, I:\kimlab__folder 2007 - Bill A_DHML library 2007-04-15 WMAwork.

Note that for IEEE 1394 Firewire, NI-IMAQ**dx** 'grandfathers' in the IEEE 1394

compatibility to the more recent 'dx' version. The AAA HoloExpt.vi and major subvi's

also allow for images to be saved as bmp or kimlab defined ".dh2c" files with notes for

later retrieval and processing. Note that continual software improvements were

incorporated over the duration of this investigation.

The procedure behind digital holography is depicted in Figure 3.7. The sample,

Allium cepa (onion) cells, resides on the prism face (with $\theta_1 < \theta_{critical}$; non-TIR mode for

engineering) and provides a direct image as shown in Figure 3.4a. With the addition of

the reference beam, the CCD camera captures the hologram created by superposition of

the object beam (OBJ) with the reference beam (REF) (Figures 3.7b and 3.9) and this is

relayed to the processing platform as a direct camera feed, over Firewire in this instance.

At that point, our LabVIEW software converts the numerical image of the

hologram into Fourier space, where it is processed, including filtering (Figure 3.7c). The

complex array comprising the angular spectrum is then transformed back into its real

image. So it is this numerical processing inherent in DHM that has allowed us to extract

the phase information and thus perform phase microscopy. ASM also allows the un-tilt

algorithm to be directly coded into the LabVIEW software routine. Note also the change

in aspect ratio between Figures 3.7d and e, and 3.7g and h due to the un-tilting process. A

Table 3.2. Primary Sub vi's (subroutines) of AAA HoloExpt.vi

Name	Purpose
camera setup (ieee).vi	Sets up the parameters of the camera for the holography session
cam image (ieee).vi	Acquires an image from the camera
res-scale.vi	Used to calibrate FOV with a USAF 1951 Resolution target
get hologram.vi	Get a hologram from images(s) acquired from the camera or read from files
AS HoloDiffract.vi	Top level program to acquire hologram and calculate diffraction using the angular spectrum method (See Fig. 3.8)

typical en face direct image of onion tissue, fig. 3.7f), is presented for comparison.

The un-tilt algorithm provides exact (non-approximated) results with a reasonable compromise in computation speed, which we perform in near real-time using CUDA (**C**ompute **U**nified **D**evice **A**rchitecture *from NVIDIA Corporation, Santa Clara, California*) hardware acceleration. Thus the angular spectrum method allows the reconstruction software to compensate for tilt anamorphism due to the inclined TIR plane of the prism with respect to the optical axis.

3.4 Sample preparation

For certain organisms, such as the live *Dictyostelium Discoideum* myxamoeba, sample preparation is as simple as placing the specimens into a gasket reservoir containing an aqueous solution on the prism hypotenuse (Figure 3b inset). The gasket reservoir here contains an aqueous (water) solution (n~1.33) around the sample, the amoeba themselves being allowed to adhere to the prism surface in range of the near-field. These *Dictyostelium* are imaged under a conformal layer of polyacrylamide approximately 100um thick that serves the dual purpose of promoting adhesion by keeping the myxamoeba down on the prism face in the near-field and maintaining an aqueous ambient around the specimens.

For our tests on live 3T3 fibroblasts and SKOV-3 ovarian cancer cells, the specimens were cultured on the prism hypotenuse which acted as a sample carrier; the gasket reservoir containing Hank's Buffered Saline Solution (HBSS; n~1.33) simply
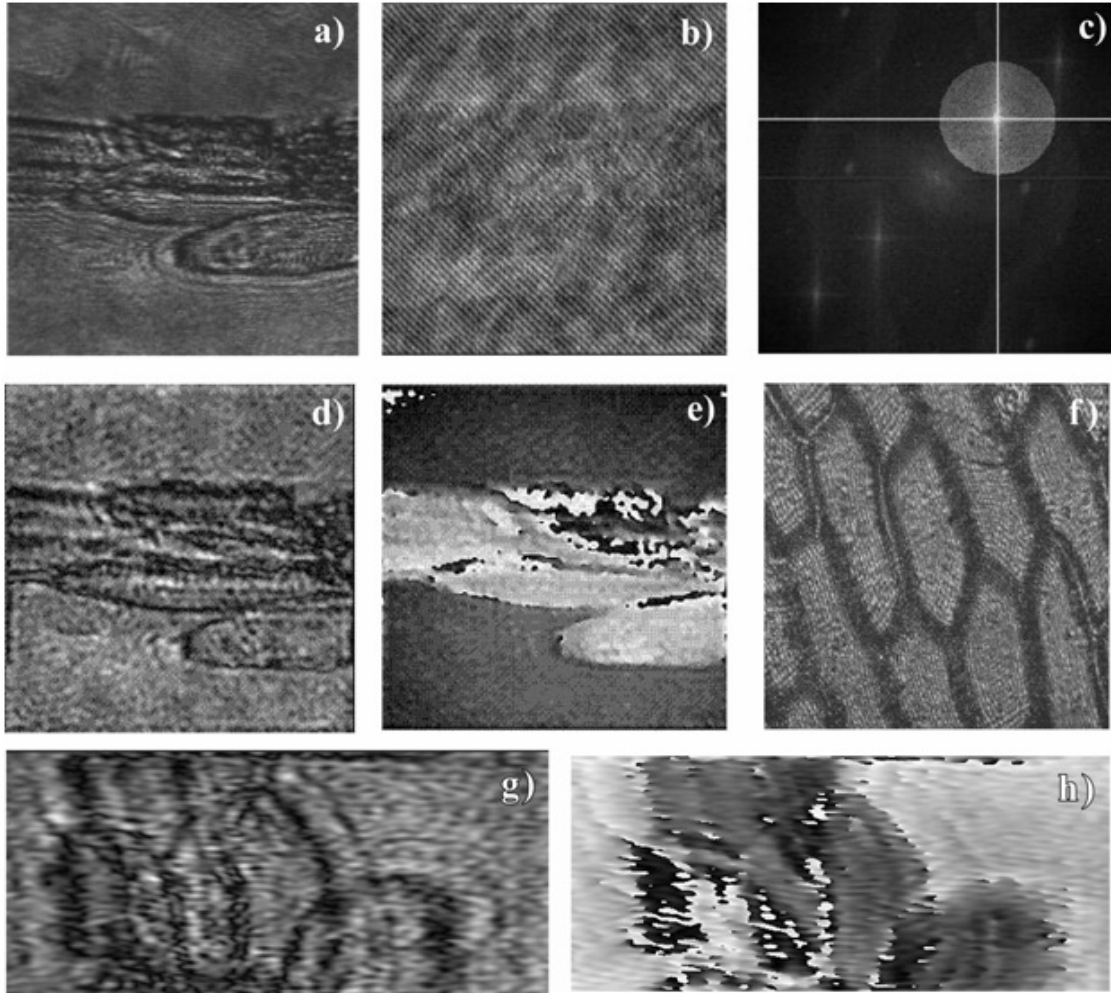
Figure 3.7. DHM process with un-tilt via the angular spectrum method: non-TIR engineering run with onion tissue (*Allium cepa*); 10x Edmund μPlan with BK7 prism. a) Direct prism image with tilt (field-of-view (FOV) (x,y); 256μm x 684μm (tilt-compressed)), b) hologram, c) angular spectrum filtering first order peak, d) and e) amplitude and phase image reconstruction with inherent tilt (FOV 256μm x 684μm (tilt-compressed)), f), typical en face 'direct' image of *Allium cepa* (FOV 400μm x 400μm), g) un-tilted (and transposed) amplitude and h) phase image. space yielding both the amplitude and the phase information (Figures 3.7 d and e).
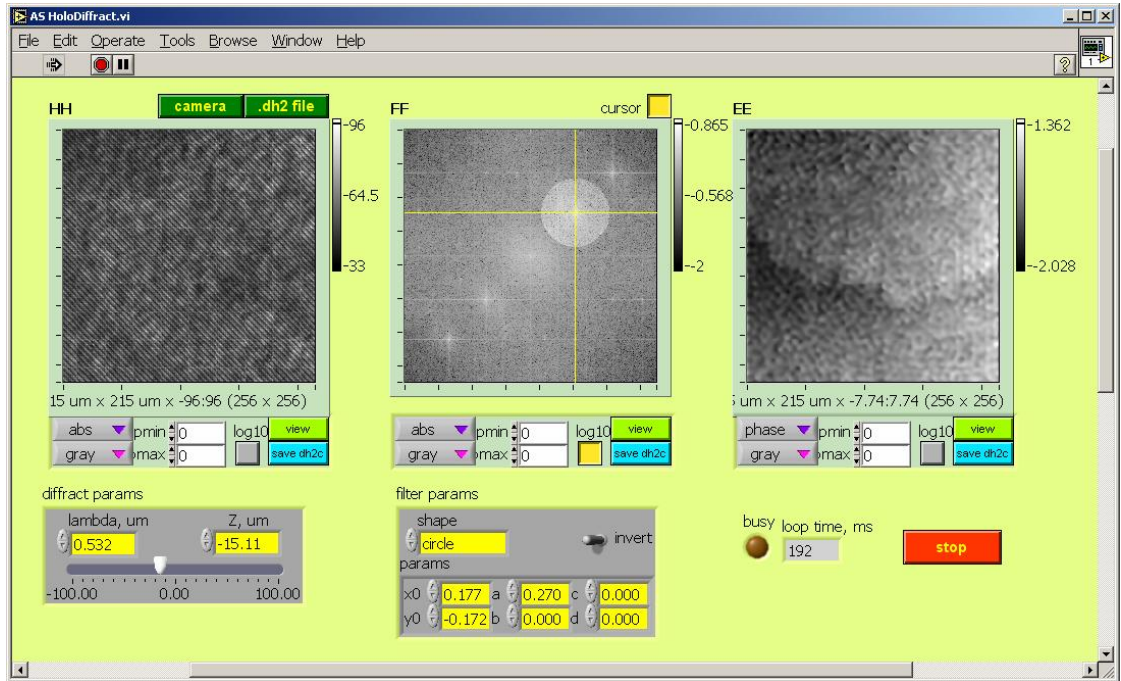
Figure 3.8 AS Holodiffract.vi Operator's screen displaying Amoeba Proteus Phase

image reconstruction (EE). HH is the hologram feed from the TIRHM camera, FF is

the hologram converted into Fourier space for filtering; the first order peak in the

"first quadrant" is selected with a circular filter, EE is the reconstructed phase

image.
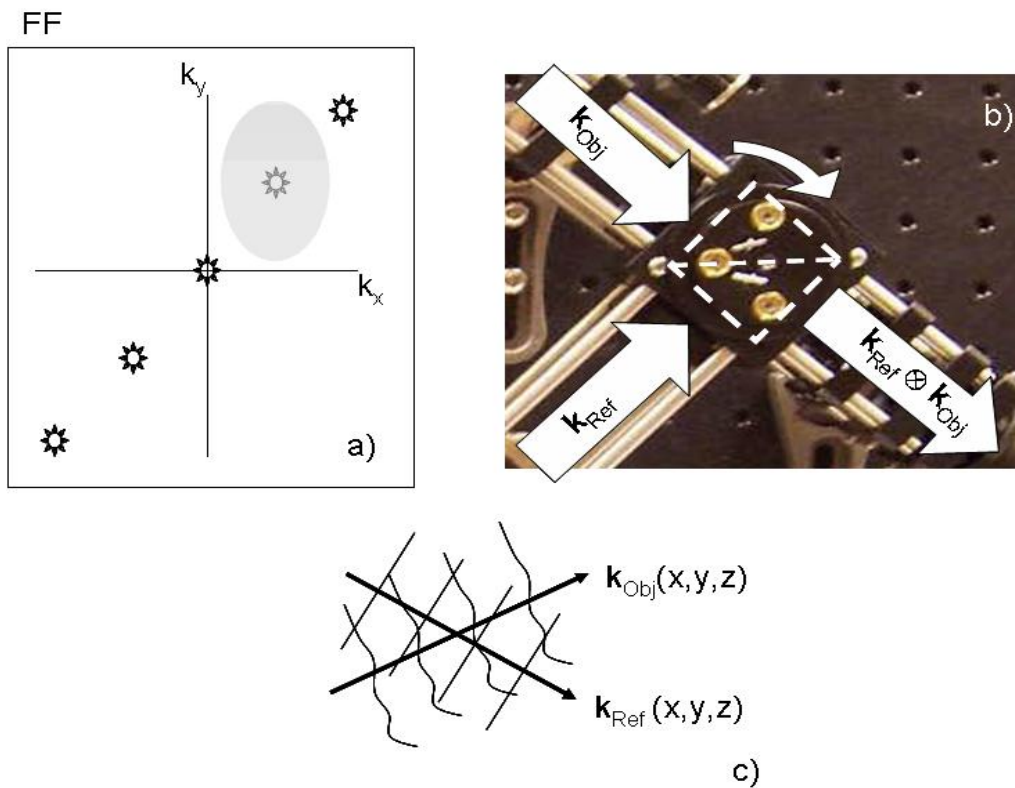
Figure 3.9 Adjustment of Angular Spectrum. a) The angular spectrum (as in "AS Holodiffract.vi") depicting selection and filter acquisition of one first-order diffraction peak (star in greyed circle) and deselection of zero order and other products, b) Beamcube holder mount and adjustment in System II; Rotation of beam cube causes k_x displacement of non-zero diffraction products in a), cube tilt adjustment with brass set screws mount causes k_y displacement, c) visualization of $\mathbf{k}_{obj}$ and $\mathbf{k}_{ref}$ wavevectors being controlled by beamcube rotation and tilt. Note: The first order peak being selected in a) should be moved away from the other diffraction products by beamcube rotation and tilt so that the filter can be made as large as possible to increase the spatial frequency components of the reconstruction.

emplaced around the sample. The fibroblasts and the SKOV-3 were prepared with standard biological preparatory procedures as related in their references [47, 48] with the kind help of Dr. Lo. *Amoeba proteus* and *Dictyostelium Discoideum* samples were obtained from Carolina Scientific Supply, Burlington, NC 27215-3398.

Table 3.3 TIRHM Project timeline

Date	Milestone achieved	Significance / Comments
2.15.07	Michelson experiments	Practice w/ camera, interferometry, ASM, LV
7.16.07	Build Mach Zehnder	Moving to more complex split beam topology
8.16.07	Install TIR prism	Begin System I with BK7 prism
2.25.08	Water droplet experiment	40 degree phase shift as predicted by theory
4.18.08	Lens experiments	Demonstrate f-TIR and n_1, n_2, n_3
12.22.08	Mounted vertical plate	Begin System II; proper object beam incidence
1.23.09	Install FO splitter	No longer constrained to mirror geometries
2.19.09	First SKOV-3 run	Target application; BK7 prism carrier
3.9.09	Mount Lookdown Camera	Ability to correlate direct image with phase
3.30.09	Mounted SFL11 prism	Denser glass lowers θ_{crit}; allows for less β tilt
4.24.09	*Amoeba Proteus* signature	Phase signatures captured
6.4.09	3T3 Fibroblast run	Target application; BK7 prism carrier
9.1.09	Lookdown camera working	Long effort to fully implement hardware
11.27.09	*Dictyostelium Discoideum*	Model organism; adheres well. Small at 7μm
1.22.10	BIOS 2010 movies	Compressed amoeba phase signature movie
2.26.10	Begin 2nd SKOV-3 run	Phase signature only after drying cycles (days)
3.11.10	Begin Polylysine test runs	Attempt for better adherence of *A. Proteus*

CHAPTER 4

EXPERIMENTS

4.1 Early efforts; EX-1A through EX-3

The first experiments of this research were conducted even before the

development of the first Mach Zehnder System I and became almost a set of

preproduction practice exercises, such as camera operations, HeNe laser illumination,

angular spectrum establishment, LabVIEW vi construction and operation, angular

spectrum diffraction and filtering, and hologram reconstruction, that built upon each

other to produce a working Michelson unit in order to produce Digital Holographic

Microscopy (DHM).

Initial sample objects were USAF 1951 1X resolution targets (Figure 4.1).

The features on this resolution target (RT) are nickel plated bars with sizes ranging from

Group 0 Element 1 (G0E1) 2500 μm long x 500 μm wide down to G7E6 (10.96μm x

2.192 μm). These RT are used in the calibration routine "res_targ" for the AAA

HoloExpt.vi software. Table 4.1 recounts much of the early groundwork in preparation

for proceeding into the TIRHM phase of this investigation.   The AAA HoloExpt

captures in Figures 4.2 and 4.3 present many of the salient features from this

experimental period using the equipment depicted previously in Figures 3.2 through 3.5.
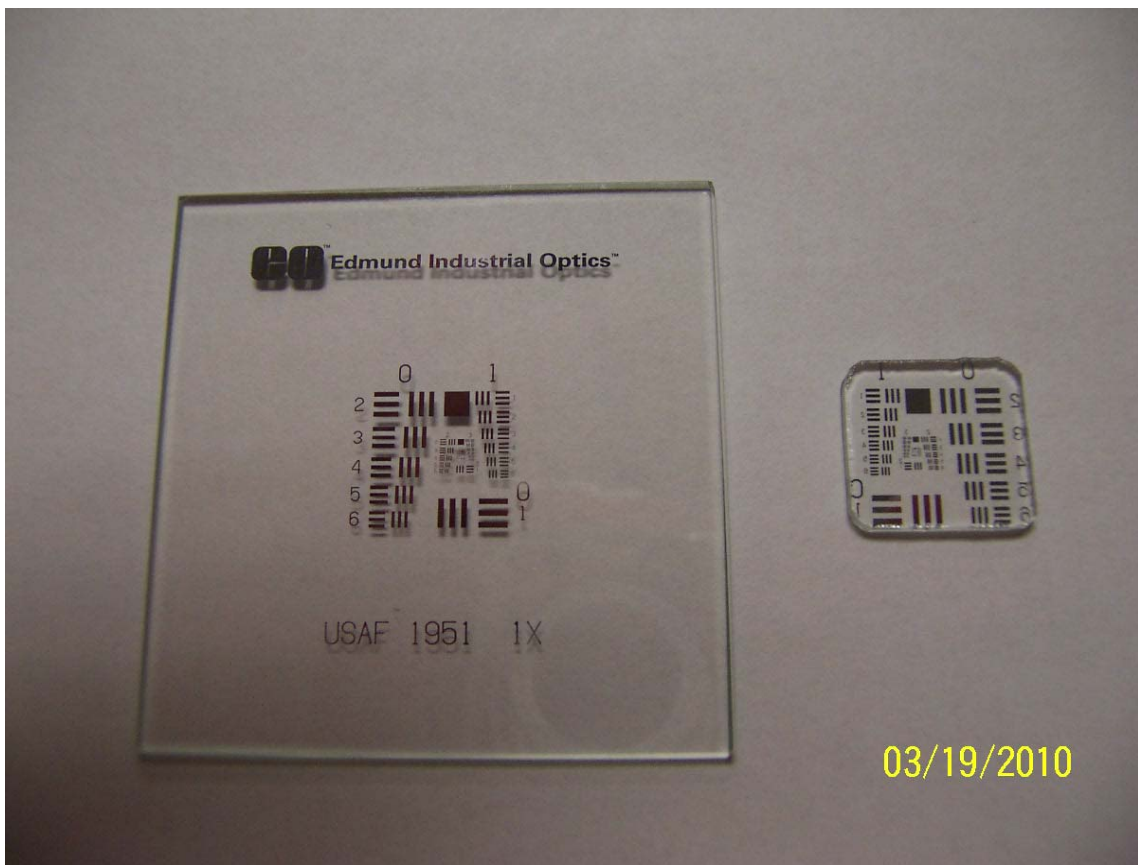
Figure 4.1 USAF 1951 1X Resolution Target. A 2" x 2" resolution target (left) and cut down chip for emplacement on TIR prism face (placed in glycerin for optical path continuity)

Figure 4.2 depicts typical progress during EX-1A; the system is the original Michelson build, with an en face RT in reflection in the object arm. Early efforts often focused on amplitude images to improve proficiency prior to tackling (the perceived) subtlety of phase imagery.

Figure 4.3 depicts another step in the development of conditions that are encountered in the full up system; the issue of plane tilt due the aspect of the TIR Prism hypotenuse to the optic axis of the system/camera FOV. EX-2 introduced increasing RT tilt angles with respect to the optic axis in order to estimate the amount of compression distortion and field defocus that would be experienced at various θ_1 and β angles. This data here presents the difference between 45 and 60 degrees of tilt on the Group 4 elements. Element 3 is kept in focus during these tests while the elements above and below become out of focus by being too far , or too close in, from the focal plane. Group 4 was chosen for this test because of its ability to quantitatively fill this field of view (FOV). Note also the difference between the amplitude images in figures 4.2 and 4.3 and remember that 4.2 is in Michelson reflection mode while 4.3 is in transmission mode in the Mach Zehnder; the bars in the transmission mode are actually an absence of light and a loss of signal in those portions.

4.2 System II Operation/ Calibration Run 11-19-09

System calibration quickly became a standard procedure in order to maintain baseline system performance and dataset integrity. Figures 4.4 through 4.7 present a

74

Table 4.1 Early Experiment plan (11/07)

Name	Designator	System	Comments / Description
Digital Holographic Techniques	EX-1A	Michelson	Fabricate Digital Holographic interferometer and operate LabVIEW software En face USAF 1951 resolution target as object
Mach-Zehnder	EX-2P1	M-Z	Fabricate M-Z interferometer
M-Z Digital Holography	EX-2P2	M-Z DIH	Reconstruct holograph of en face USAF 1951 resolution target as object
Tilt target	EX-2P3	M-Z DIH	Reconstruct holograph of tilted USAF 1951 resolution target as object; 0° to 75° in tilt
Lazy 4	Quicklook	MZDIH w/Prism	Reconstruct holograph of USAF 1951 resolution target as object on prism in glycerin
Lens spot	EX-3P1R800 Quicklook	TIRHM	TIR spot pattern of f = 300mm planoconvex lens (PCX300)
Thumbprint	EX-3P1R1000 QLII	TIRHM	Reconstruction of thumbprint on prism (not really TIR regime)
Teflon tape	EX-3P1R2000	TIRHM	Image Teflon tape on PCX300 lens surface Planned for week of 11/28/2007
TCMPP	EX- 4 Phase M	TIRHM II	TIRHM Cellular Motion Picture Photography Planned for 12/07 into 1Q08

Figure 4.2 AS HoloDiffract Operator's screen; Exp-1A with Michelson unit.

Output EE is an Amplitude image Object is USAF resolution target en face in reflection Group 4 Element 2. (G4E2 = 139.2μm x 27.84 μm) Note the filter area (FF) is very small with the angular spectrum products all on line. Wavelength (lambda, um) is not set; should be .594 um. z (z, um) should be numerically compensated for focus, but isn't.
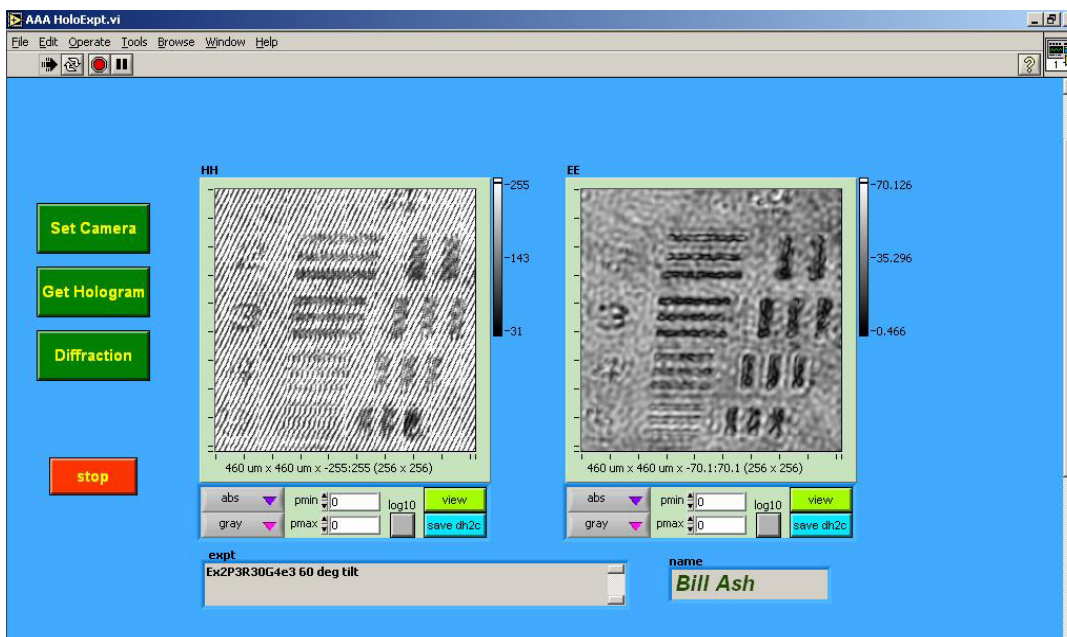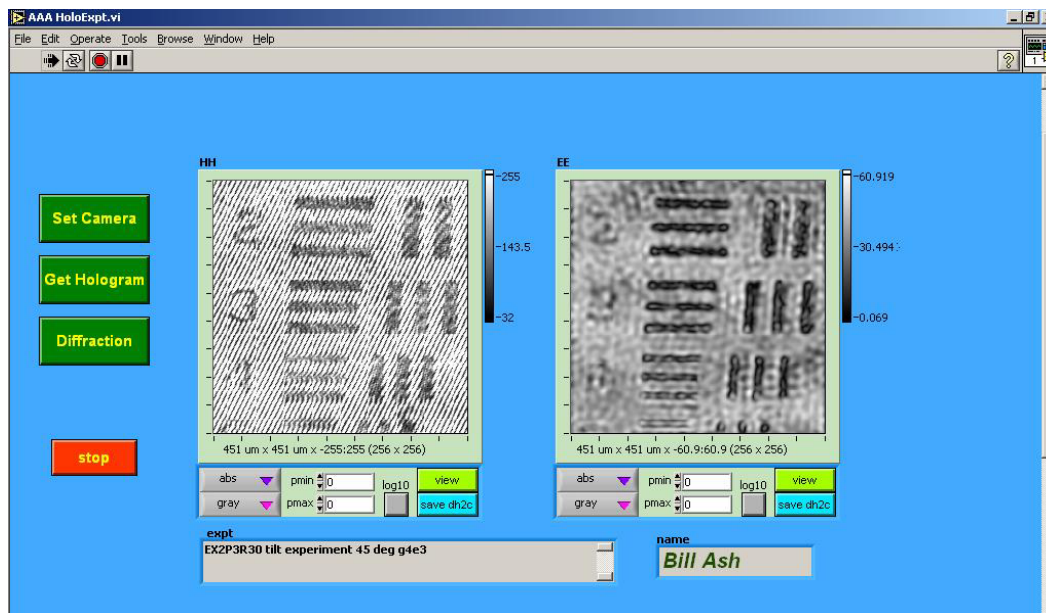
Figure 4.3 EX2 RT Tilt experiment; a) Tilt at 45°. Screen capture is from "AAA

HoloExpt" top level vi routine – final/end console. Object is RT G4E3 (124.0 μm x

24.80 μm) in transmission in M-Z unit (Fig 3.3) with 45° of tilt to optical axis.

b) Tilt at 60°, Object is RT G4E3 (124.0 μm x 24.80 μm) in transmission in M-Z

unit (Fig 3.3) with 60° of tilt to optical axis.

photodocument record of a System II calibration run performed on 11-19-09 when the system was fairly mature from a hardware perspective and software improvements for phase movie captures were being tested and implemented. Initial setup is performed with the NI MAX routine to check camera alignment and focus and to set camera shutter speed. MAX can not be running when AAA HoloExpt is brought up or the camera acquisition software will go into contention.

The RT chip is placed on the TIR prism in glycerin and allowed to settle to remove bubbles, sometimes overnight. Alignment is first performed with the TIR camera (cam0) (Figure 4.4) and then the Lookdown camera (Figure 4.5) alignment and registration is brought into agreement with the TIR camera position. Lookdown illumination is with red Super luminescent diode (SLD) through prism truncation. Development of the hardware and software worked as diligently as possible to get agreement between the two FOVs, taking the prism tilt compression into account (compare TIR camera images with lookdown images throughout). The RT features in this calibration run are groups 6 and 7; G6E1 = 7.182 x 39.06 um, G7E6 = 2.192 x 10.96um.

After the cameras have been aligned and their shutters speeds set for the correct relative exposure times to get the correct relative beam level balance, the reference beam intensity must be set higher than the object beam so that the object beam amplitude modulation is above the reference beam zero floor, the MAX control settings are saved and MAX is closed (Note: The initial computer has enough throughput to run two MAX routines simultaneously, the newer machine eventually lost this capability; perhaps from externally controlled software uploads). After exiting MAX, LabVIEW is brought and
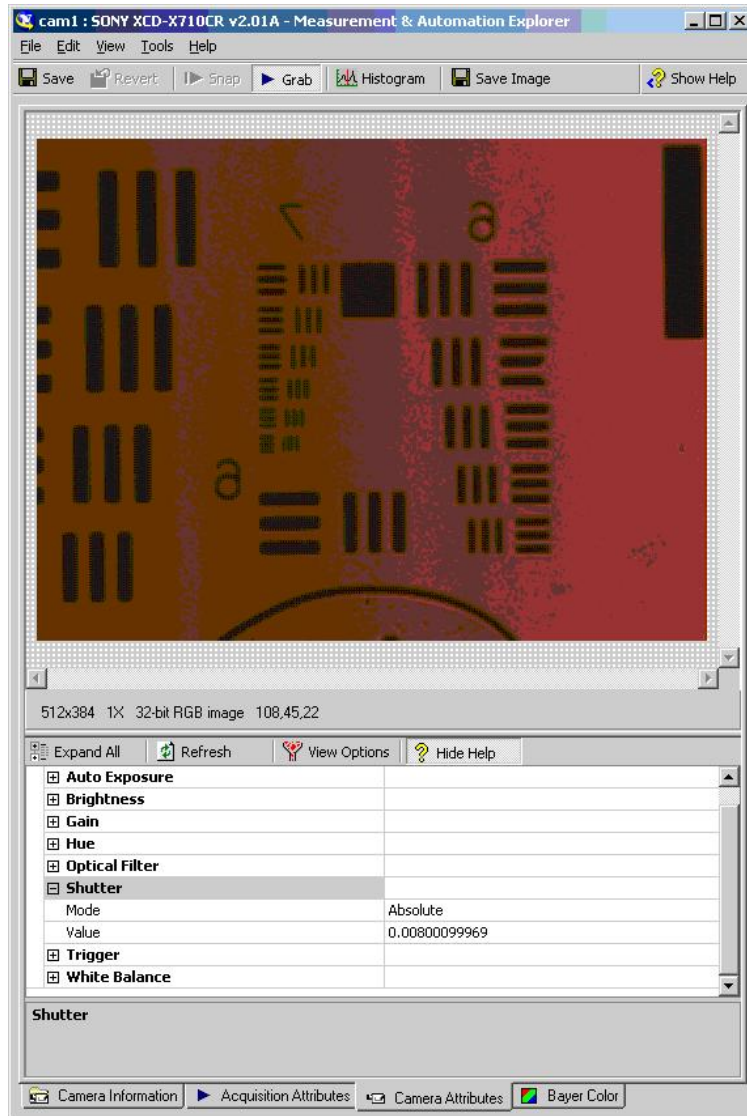
Figure 4.4 TIR camera MAX image of RT chip in glycerin on truncated SFL11 TIR prism; Groups 6 and 7. Tilt compression in phase image is in x-direction. Illumination is with green laser object beam. Shutter speed at 0.02s. Note bubble curvature at bottom FOV; black for loss of signal (LOS).

AAA HoloExpt.vi is loaded and run. The first action is to run the Camera Setup (ieee).vi

routine from the top level AAA routine. Note that this is a the IEEE 1394 FireWire

version for the SONY cameras used on TIRHM. The camera setup routine displays the

TIR camera power bar, the TIR camera hologram feed, the lookdown camera feed and

the angular spectrum.

Having roughed the reference and object beam power levels in MAX and set a

nominally camera speed, the final adjustments on ref and obj power levels are made in

camera set up with the power bar. In order to stay out of overdriving the input, the obj

and ref beams are checked against the power bar reading separately and the levels

adjusted with the polarizers on the reference beam and the camera input, the obj beam

polarization being locked perpendicular (s-polarization - senkrecht) to the prism plane of

incidence at the object beam expander/collimator polarizer control. Object beam usually

runs about 3 bars and the reference beam level near 4 bars.

Camera setup is also where the hologram feed is calibrated; the <scale> control

conveniently runs "Res_scale" so that the RT can be measured on the screen and the

correct FOV set. **NOTE: TIR prism compression must be taken into account when**

setting the FOV, so care must be taken to read in-focus, non-compressed RT bars.

Note that the FOV can also be selected in the TIE camera feed screen. Once the FOV has

been correctly set the next step is to align the angular spectrum. In order to insure proper

Angular Spectrum (AS) alignment for this TIR system, please refer to the discussion that

goes with "**Figure 3.6 Adjustment of Angular Spectrum.**" The AS adjustment set

Figure 4.5 Lookdown camera MAX image of RT chip in glycerin on truncated SFL11 TIR prism; Groups 6 and 7. Illumination is with red Super luminescent diode (SLD) through prism truncation. Shutter speed at 0.0008s. Note bubble curvature at bottom FOV. (Some image degradation due to electronic storage and reproduction.)

screws are located on the beam cube dynamic mount and are set while viewing the AS

feed in the camera setup panel. Once the power levels, FOV and angular spectrum are

set, the camera setup routine is closed and software control reverts to top level vi. The

next step is to acquire the hologram and perform filtering and reconstruction.

The hologram can be acquired either at <Get Hologram> or, with the

implementation of direct hologram feed for real time phase imagery and movie

production, acquisition can take place in the AS HoloDiffract routine. AS HoloDiffract

has controls to acquire and filter the AS and display processed data. Figure 4.7 presents a

screen capture of the phase image and lookdown camera feed from the RT target

calibration run in this section. Note reasonable definition in the phase image down to

about G7E2 (3.480 x 17.40um) and G7E5 is visible in phase. Note also the overall

planarity of the phase image, consistency of filed composition and generally acceptable

noise figure overall.

Subsequent to calibration runs such as these the system would display reasonable

stability even after TIR prism removal and remount. The image mode of Figure 4.7 also

must be understood because it is in this setting that long duration acquisitions would be

performed. In this operator's panel, prism x-axis traverse, display vertical axis, is

conducted in a straightforward fashion with the x translation micrometer control, the only

limitations therein being alignment tolerance of the prism body coordinates to the optic

axis and maintenance of full illumination coverage. Prism traverse in the view panel x –

axis, the compression axis, is slightly more involved. The prism micrometer controls for

the other two body axes, being affixed to the vertical plate (Figure 3.6), they are rotated
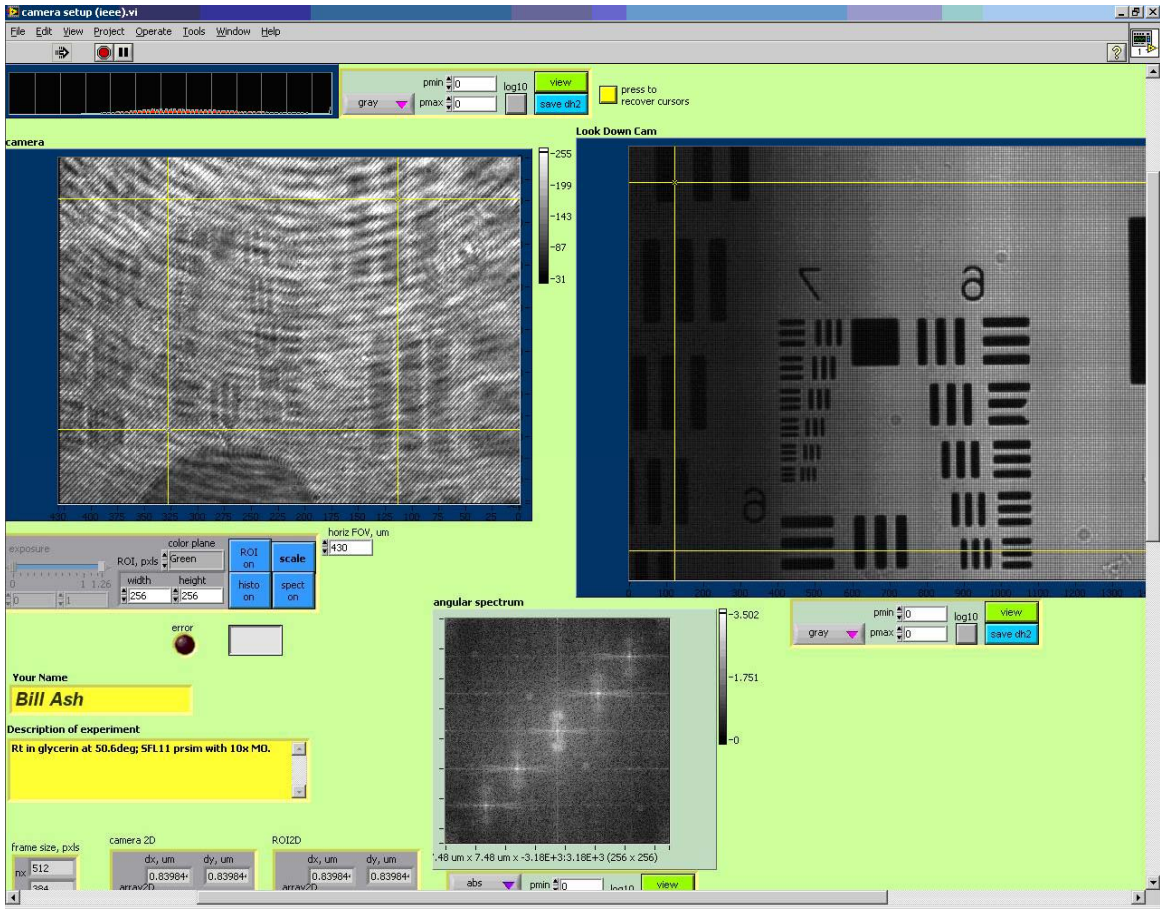
Figure 4.6. Camera Setup (ieee).vi routine; Operators console. Hologram on left

Lookdown camera feed on right. FOV calibrated at 430um. The power levels of the

object and reference beam are too high, as evinced by the power bar top left and the

angular spectrum diffraction products at bottom center, and are reduced either by

adjusting the polarizers or increase of camera speed in MAX. This setup required further

adjustment.

counterclockwise from the TIR optic axis and thus sample positioning much be

compensated for by a combination of micrometer adjustments, but this can also be

accomplished with sufficient practice.

One final operator control worthy of note in the AS HoloDiffract operator's panel

of Figure 4.7 is the movie sequence control <Start BMP Sequence> located below the

image windows. This control initiates image capture of the hologram, the phase image,

and the lookdown camera image which are saved to files for processing into movie

sequences in order to characterize phase images over time. In order to capture these

movie sequences the operator can spend lengthy periods examining and positioning

samples with the real-time phase and lookdown feeds and capture image sequences of the

most useful datasets.

4.3 Water droplets and Lens Experiments

First, we demonstrate the imaging of the reflected phase profile due to variations

of refractive index of materials in contact with the prism. As shown in Fig. 4.8(a), water

droplets of index n_2=1.333 are placed on the prism of BK7 glass, n_1 = 1.517. Figure

4.8(b) is the amplitude image of the reflected optical field, while Fig. 4.8(c) is the phase

image, at the object plane A, calculated from a hologram image at H., The field of view is

300 x 900 μm^2 and the presumably circular water droplets, of about 100μm in diameter,

appear highly elliptical because of the relatively large angle of the plane A relative to H.

Given the angle of incidence $\theta_1 = 72°$, TIR is in effect for both glass-air and
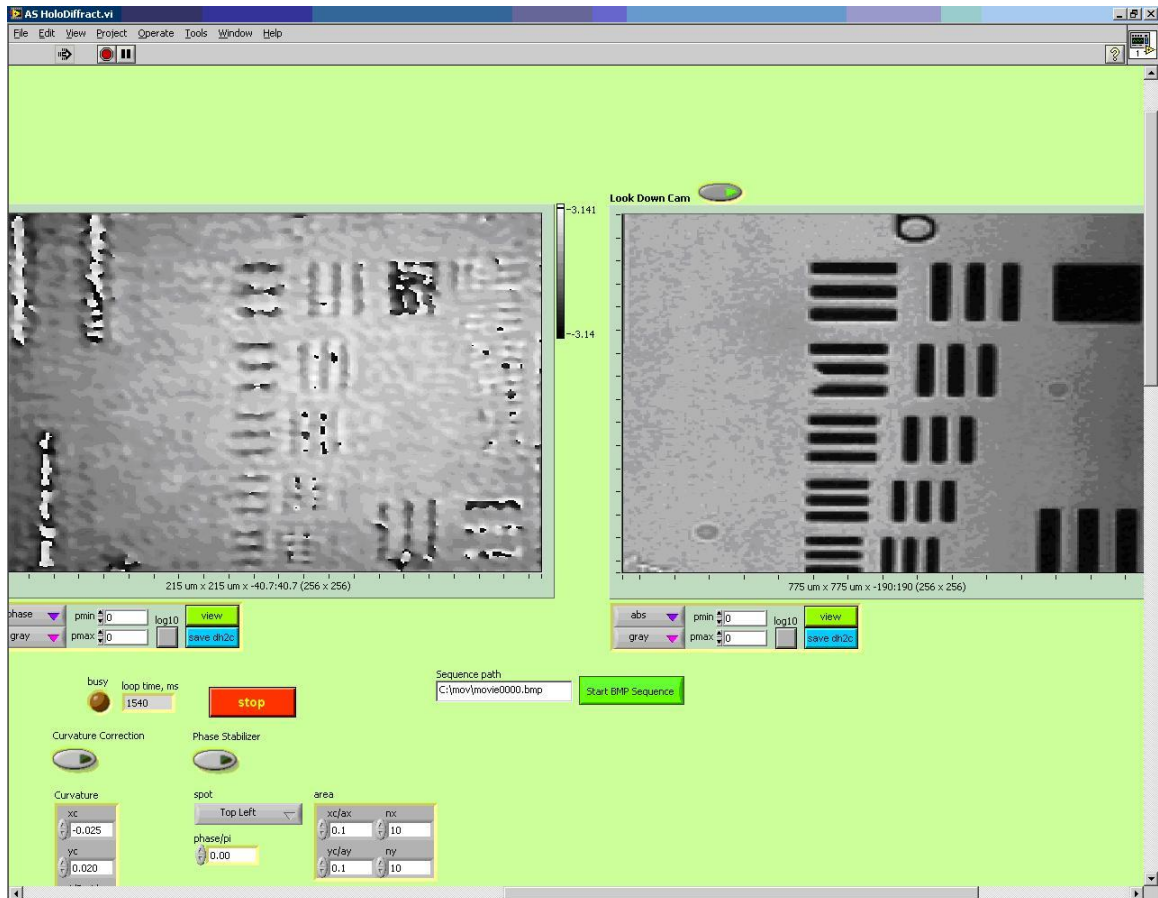
Figure 4.7 AS HoloDiffract.vi RT calibration run; Operators Console. Phase image of RT on left, LookDown camera feed on right. Tilt compression in phase image is in x-direction. Operation in this configuration allows the operator real-time simultaneous viewing of phase image and Lookdown direct image. Note movie sequence control <Start BMP Sequence> below image windows. The curvature correction and phase stabilizer controls for software compensation are also visible at bottom left.

85

glass-water interfaces. The amplitude image of Fig. 4.8(b) does show variations in intensity due to diffraction from phase discontinuities and other spurious interference. We note that when the angle of incidence is not large enough for TIR at the glass-water interface, the water droplets appear as black spots because of the diminished reflectance. On the other hand, the phase image of Fig. 4.8(c) has significantly less noise or spurious signal and displays the profile of water droplets with good fidelity. Referring to Fig. 2.2(c) in Section 2 Theory, the reflection phase shift is $\varphi = -131°$ for the glass/air interface, while it is $\varphi = -97°$ for the glass/water interface, so that the phase difference between the two areas is expected to be $\Delta\varphi = 34°$.

Figure 4.8(d) is a cross-section through one of the droplets of Fig. 4.8(c), where the phase step is measured to be about $\Delta\varphi = 40° \pm 5°$. A similar measurement is made using 50/50 mixture of water (1.333) and ethylene glycol (1.432) in Fig. 4.8(e). With presumed index of 1.382 for the mixture, the expected phase step is $\Delta\varphi = 85°$, while the measured value is $\Delta\varphi = 60° \pm 10°$. Although these numerical values have significant uncertainties, the trend is consistent with expectation, i.e., the larger the index difference, the larger the phase difference.

The next experiment demonstrates imaging of phase profile resulting from variation of thickness of the gap between two layers of materials. As depicted in Fig. 4.9 and 4.10(a), a fused quartz plano-convex lens ($n_3 = 1.458$) of UV focal length 250 mm is placed on the glass ($n_1 = 1.517$) prism. Note that only the index of refraction (at visible wavelength) and the surface curvature of the sample lens are the pertinent parameters for this experiment, while the UV focal length is not. The angle of incidence was 75°, just
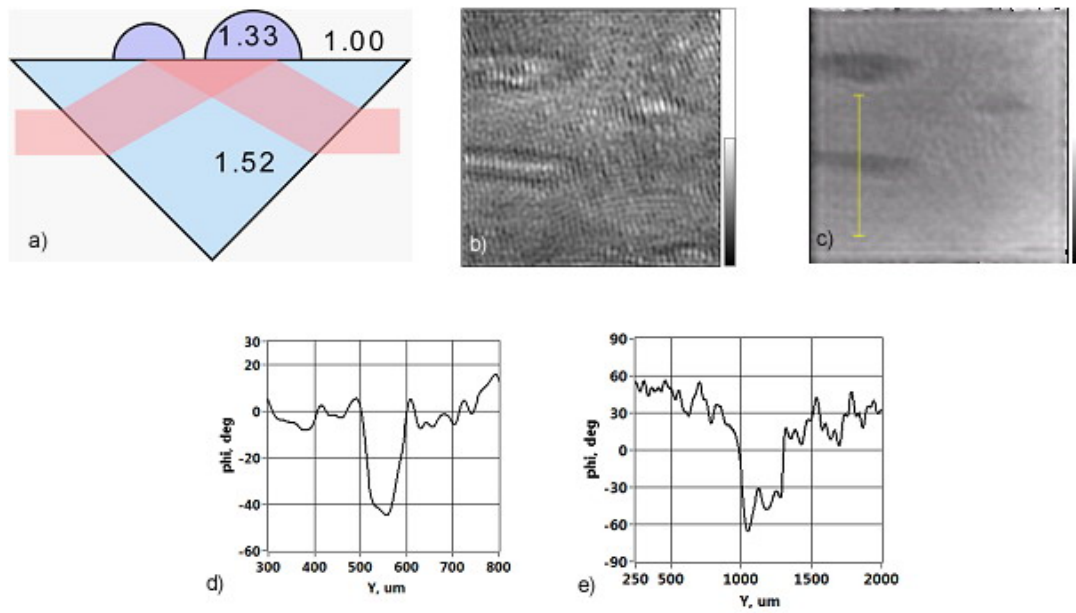
Fig. 4.8 Water droplet Experiment. a) General configuration of water droplets placed on prism. b) Amplitude and c) phase images of light reflected from the prism. Field of view is approximately 300 x 900 μm^2 with 256 x 256 pixels. Gray scale for b) is 0 ~ 1 in arbitrary unit, while for c) it is -180° ~ +180°. d) Graph of cross-section along a vertical line through a water drop in c). Fig 4.8 e) is a similar graph for a droplet of 50/50 mixture of water and ethylene glycol.

beyond the critical angle of glass-quartz interface ($\theta_{c,13}$ = 74°). The relatively uniform

amplitude image in Fig. 4.10(b) indicates TIR, whereas the phase image in Fig. 4.10(c)

shows a clear profile of the contact area (which again has about 3:1 anamorphism). The

field of view is 260 μm horizontal by 780 μm vertical. The radius of curvature of the

convex surface is 115 mm (UV lens), so that the air gap (n_2 = 1.000) goes from zero at

the point of contact to 660 nm at the edge of the 780 μm vertical field of view.

A cross-section of Fig. 4.10(c) along a vertical line through the center of the spot

is shown in Fig. 4.11(a), while Fig. 4.11(d) shows such cross-section calculated from the

given indices and curvature. The measured phase dip through the spot is 130° ± 15°,while

the modeled value is 100°. The discrepancy is attributed to spurious diffraction

perspective rendering in Fig. 4.10(d), represents the area of contact, circular shape of

about 140 μm diameter and within 20 nm between the prism and lens surfaces. That is,

the thickness of the evanescent field is about 20 nm and the profile of the lens surface

within the evanescent field can be imaged. The measurements are repeated by filling the

glass-quartz gap with 50/50 mixture of water and ethylene glycol (n2 = 1.382, Fig.

4.11(b) and 4.11(e)), and with pure ethylene glycol (n2 = 1.432, Fig. 4.11(c) and 4.11(f)).

 The expected phase dips for these cases are 60° ± 15° and 35° ± 15°, while the

measured values are 80° and 50°, respectively. These measured values of phase dips as

well as the width of the spots show trends consistent with the model. When the gap is

filled with these materials, the index difference across interfaces become smaller and the

evanescent fields become thicker. The maximum gaps that can be imaged in these cases

are 70 nm and 120 nm, respectively.

Quick Target Radius

$(x-h)^2 + (y-k)^2 = R^2$

R = 5 cm

100 nm

0,0   1 mm

W. M. Ash
5/5/07
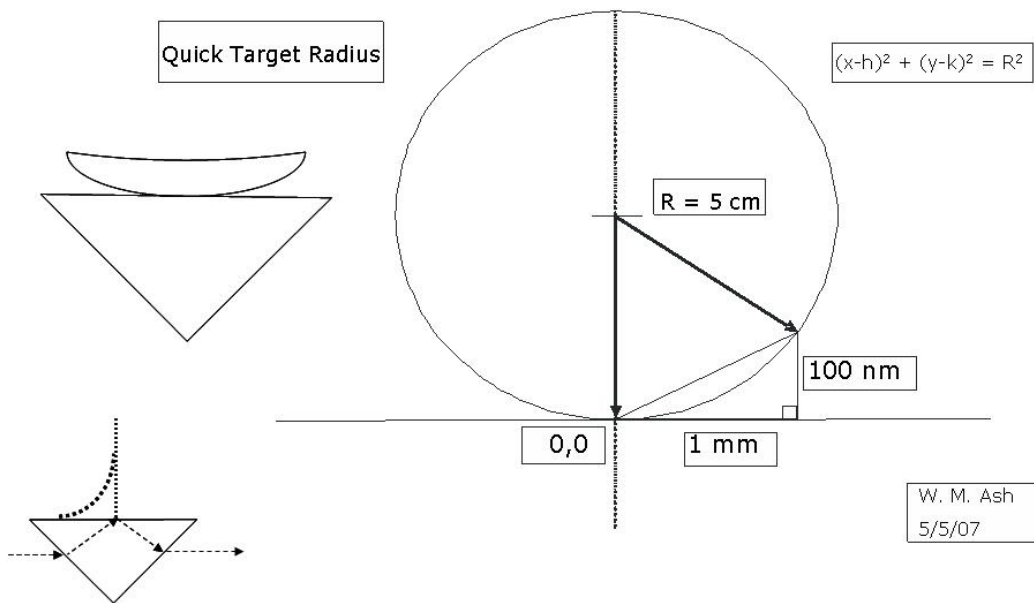
Figure 4.9 Lens Experiment geometry example. In this calculation here f =100mm $\rightarrow$ R

= f/2 = 100mm/2 = 50mm = 5cm. This lens will be 100nm off the prism hypotenuse

1mm or 1000 μm from the point-of-contact at the lens vertex.
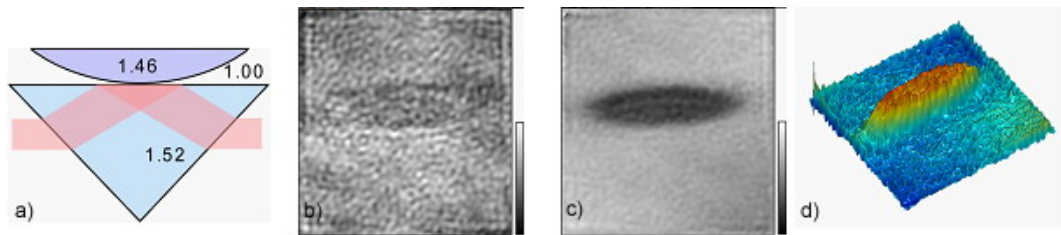
Fig. 4.10 Lens Experiment Results a) General configuration of quartz lens placed

on prism. b) Amplitude and c) phase images of light reflected from the prism. d)

Pseudo-color perspective rendering of c). Field of view is approximately 260 x 780

μm^2 with 256 x 256 pixels. Gray scale for b) is $0 \sim 1$ in arbitrary units, while for c) it

is -180° ~ +180°.

4.4 TIRHM of cells: *Amoeba Proteus*

Performed with System II as described in Section 3, Experimental Setup. Test specimens, tissues and protists, such as the *Amoeba Proteus,* SKOV-3 ovarian cancer cell and 3T3 fibroblasts presented herein, were quantitatively imaged both in amplitude and phase to evaluate of critical performance parameters, such as its resolution limit, and demonstrate performance as predicted by theory.

Figure 4.12 is a capture of a live *Amoeba Proteus* sample on a right angle SFL11 prism taken with a 10X Edmund μPlan MO and with a tilt-compression ratio of about 2:1 x-axis (tilt-compressed) versus the non-compressed y-axis. The aqueous amoeba sample was placed in a covered reservoir directly on the hypotenuse face of the prism.

Figure 4.13 is a capture of a live *Amoeba Proteus* sample on a right angle SFL11 prism taken with a 10X Edmund μPlan MO. In figure 4.13 e) through h), protoplasm movement, captured at 7 minute intervals, may be discerned by thrust activity designated at arrow between phase captures relative to overall relaxation, shift and counterclockwise rotation for the feature in general.

The feature in Figure 4.14. was imaged during an *Amoeba Proteus* run. The features bear strong resemblance to other *Proteus* protoplasm. Note the near total attenuation of amplitude signature and pronounced phase cross-section indicative of TIR.. Taken with 10xMO on SFL11 prism with incidence of 50 degrees.
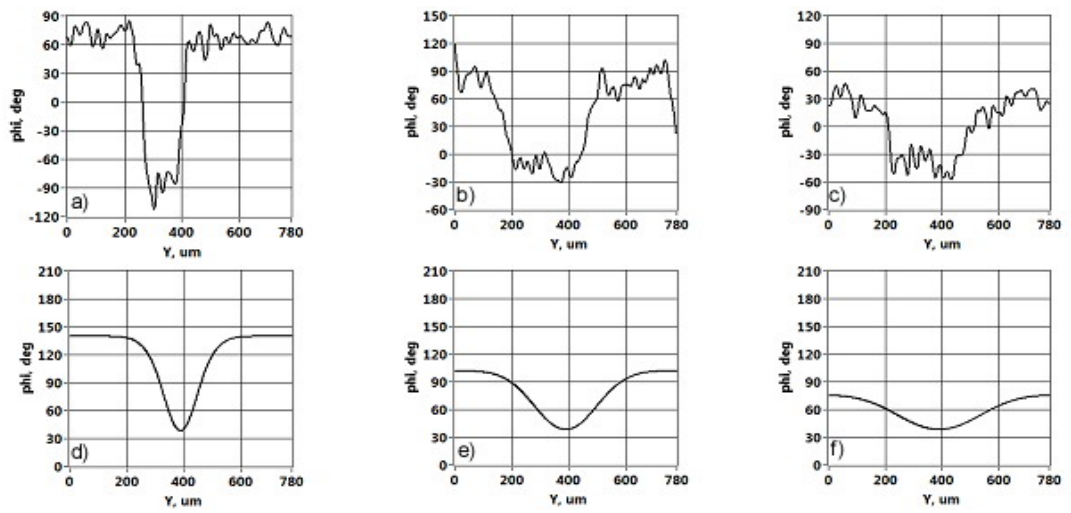
Fig. 4.11. Cross-section of phase profile across the contact spot of quartz lens on glass prism, when the gap is filled with a) air, b) 50/50 mixture of water and ethylene glycol, and c) pure ethylene glycol. Panels d), e), and f) are the corresponding theoretical graphs.

4.4 TIRHM of cells: *Dictyostelium Discoideum*

Figures 4.15 through 4.17 present near-field phase images of *Dictyostelium Discoideum* in their myxamoeba stage imaged on an SFL11 prism in an aqueous solution with the 25X LWD MO. In Figures 4.16 and 4.17, a) is the near-field phase image, while b) is the same feature looking down with a 20X MO on a direct camera feed (LookDown camera). The tilt compression in the horizontal axis of the raw phase images due to the inclination of the prism geometry is numerically compensated by the un-tilt ASM algorithm in c). The direct lookdown camera in Fig 4.17 b) images down through a ~100um layer of polyacrylamide which holds the *Dictyostelium* onto the prism face in an aqueous film. The aggregate structure in Figure 4.17 is composed of individual *Dictyostelium* (myx)amoeba which are themselves about 10μm in size.

4.4 TIRHM of cells: **SKOV-3 Ovarian Cancer**

Figure 4.18 is a capture of a SKOV-3 ovarian cancer cell taken on a right angle BK7 prism with a 25x/0.40 LWD UNICO Plan microscope objective. Note that a phase signature is still apparent at the extremities of the cell where lamellipodia are present. Also note the features in the specimen's interior. In this dataset, dead SKOV-3 cells were fixed directly onto the hypotenuse face of the ½" BK-7 prism; the prism serving doubly in the role as sample carrier.
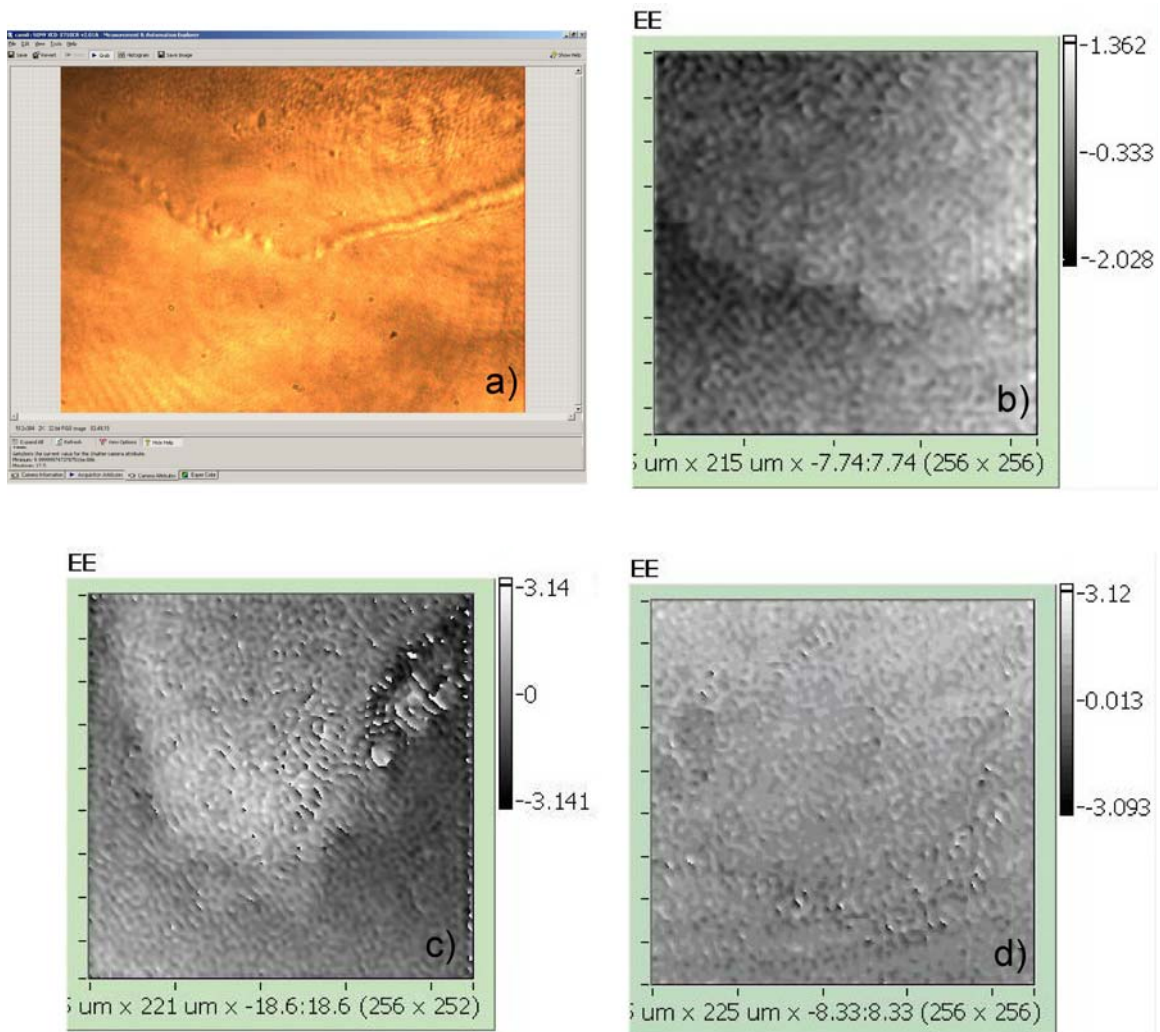
Figure 4.12. *Amoeba Proteus* **sample;** a) MAX image of TIR camera feed indicative

of cell membrane in *Amoeba Proteus* sample illuminated with HeNe laser (594nm),

b) close up phase image of center FOV in a); c and d) Phase imagery from *Proteus*

samples. Taken with 10X MO and SFL11 Prism at 48.8 deg.
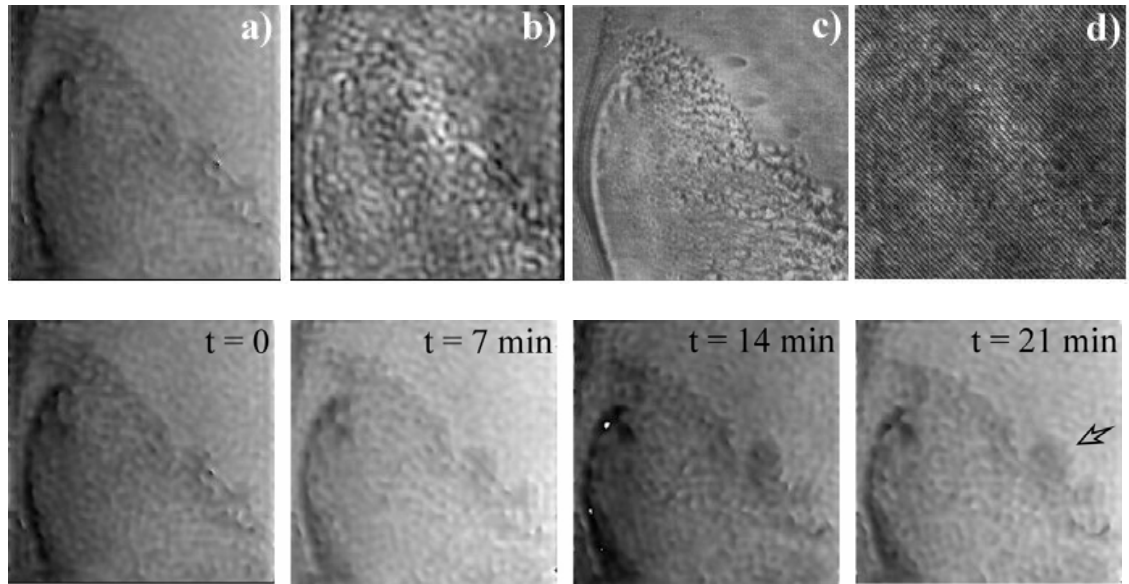
Figure 4.13. *Amoeba Proteus* sample; 10x Edmund μPlan with SFL11 prism, a) Phase image, b) amplitude image, FOV 250 μm (tilt-compressed) x 125 μm . c) Direct image (for reference), d) Hologram, e) through h) *Amoeba Proteus* sample activity at 7 minute intervals.
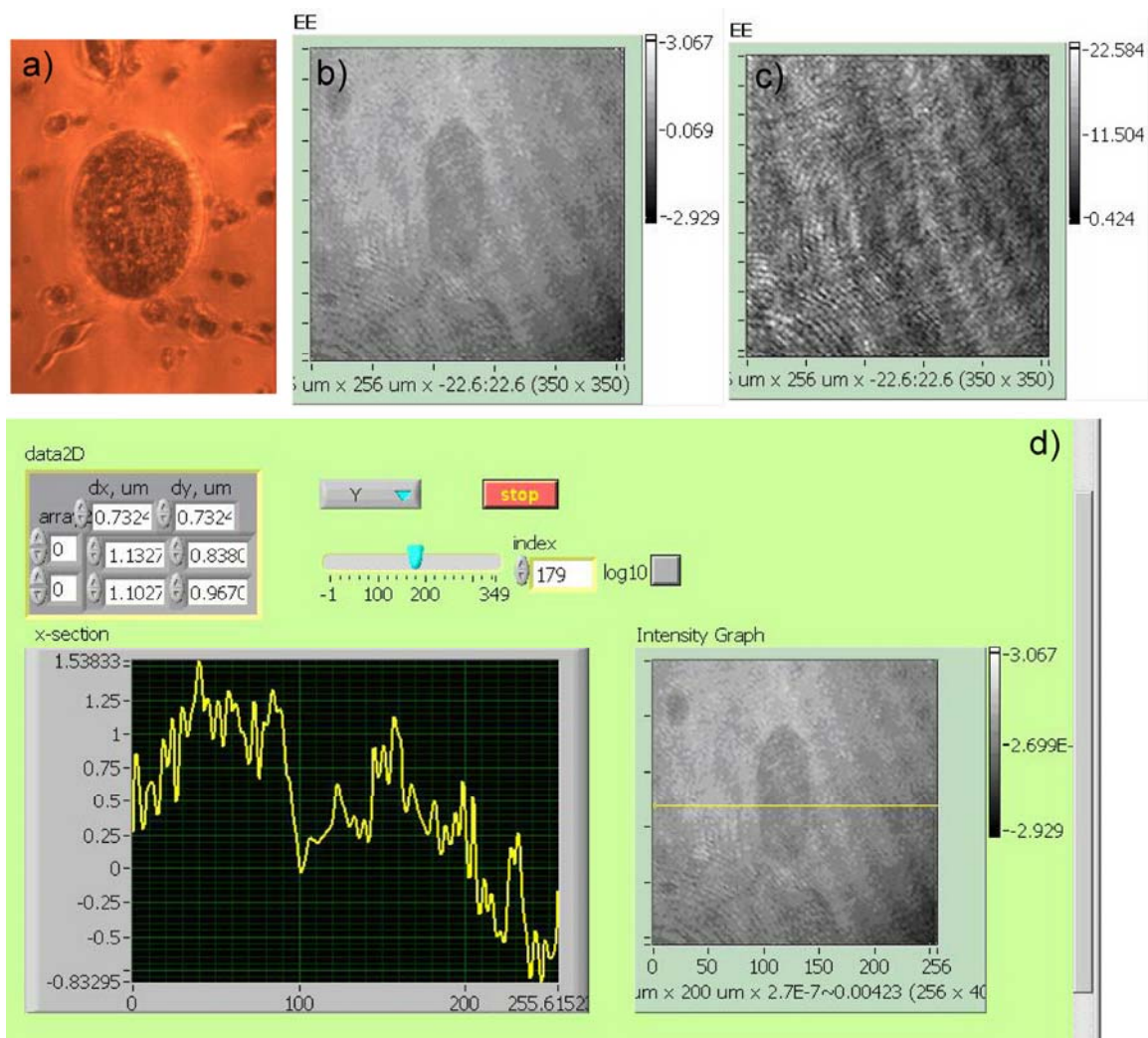
Figure 4.14. Proteus Sample. This feature was imaged during an *Amoeba Proteus* run. The features bear strong resemblance to other *Proteus* protoplasm. Note the near total attenuation of amplitude signature and pronounced phase cross-section indicative of TIR.. Taken with 10xMO on SFL11 prism with incidence of 50 degrees.
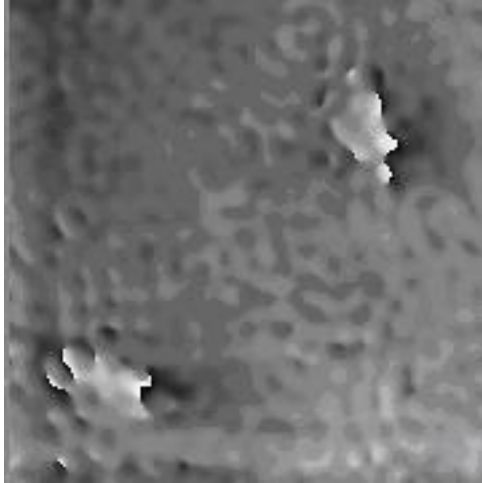
Figure 4.15. *Dictyostelium Discoideum*. (FOV ~90μm (compressed) x 60 μm)
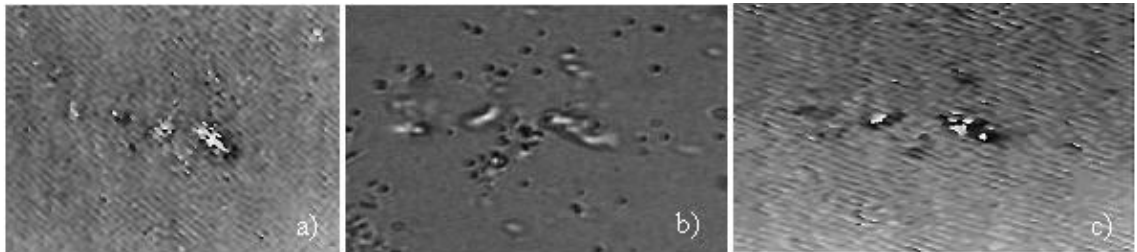
Figure 4.16. *Dictyostelium Discoideum* **TIRHM.** a) Raw phase image with inherent tilt compression in horizontal axis. (FOV ~131μm (compressed) x 86μm), b) Direct lookdown image for comparison; intentionally defocused to highlight the nearly transparent *Dictyostelium* (FOV 131μm x 86 μm) c) Un-tilted phase image of 3a) (here $\beta = 66°$ is used for un-tilting)
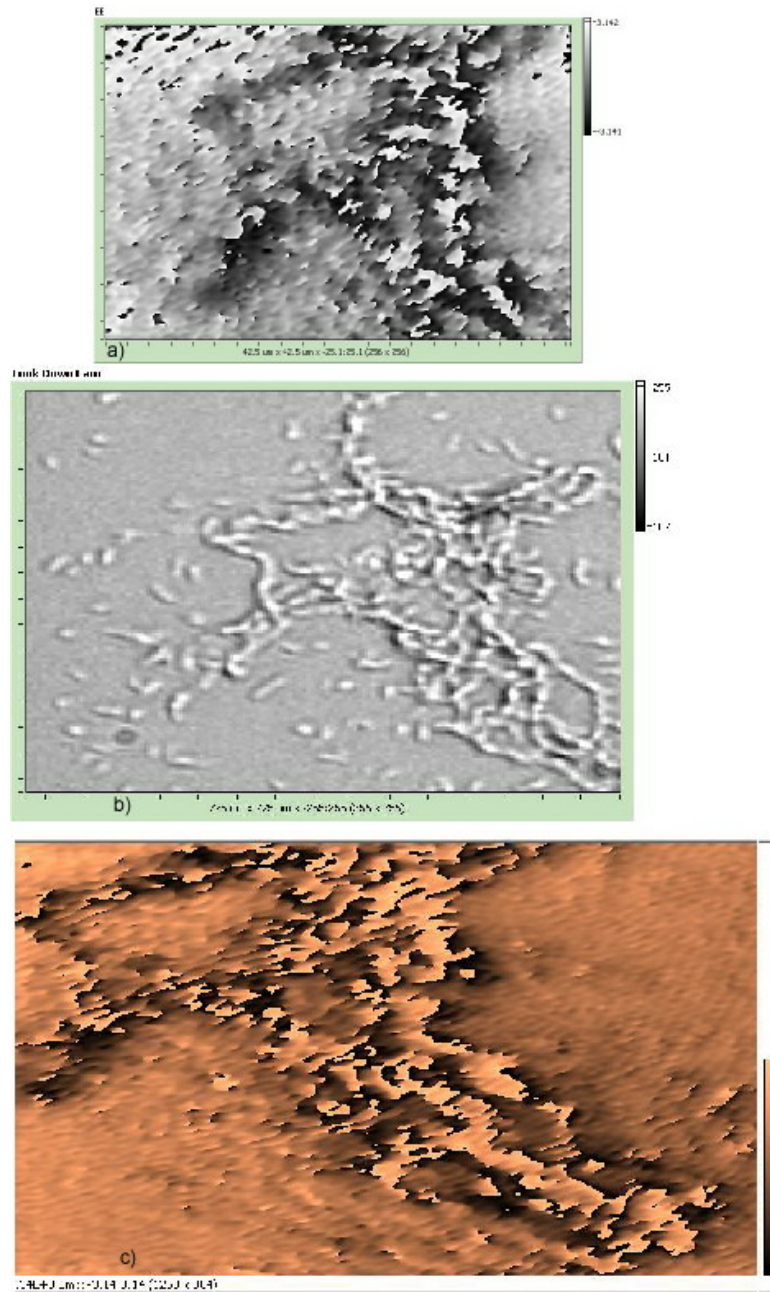
Figure 4.17. TIR holographic microscopy: *Dictyostelium Discoideum.* a) phase

image (FOV ~80μm (compressed) x 42 μm), b) direct image looking down at prism

face (slightly defocused to highlight nearly transparent myxamoeba),

c) phase image, β = 66°. Scale bar is 10μm.

Figure 4.19 is from the second run of SKOV-3 cultured on SFL11 prism with 25xLWD UNICO plan. This run was intiially intended to be a live run in order to image SKOV-3 motion, however, phase signatures were not obtainable until after the sample sat in the laboratory environemnt for 48hiurs and subject to random drying and rehydration steps, possibly fixing the cells onto the prism face. Note that the TIR phase image shows round feature of cell at center FOV and "ridge" adhesion below it. Note that there is also slight rotation in the lookdown camera mount and subsequently its FOV.

4.4 TIRHM of cells: 3T3 Fibroblast

Figure 4.20 is a capture of a 3T3 fibroblast cell taken on a right angle SFL11 prism with a 25x/0.40 LWD UNICO Plan microscope objective. Note the features in the specimen's interior. In this dataset, the fibroblast cells were cultured directly onto the hypotenuse face of the SFL11 prism; the prism serving doubly in the role as sample carrier.

While the phase image does produce an overall still capture, the pronounced amplitude image in b) would seem to indicate a lack of full TIR. The fibroblasts were cultured onto the prism surface still extant, their sensitivity to temperatures below 37°C, and in vitro conditions in general, limited the duration of this data capture. In order to alleviate this situation for future image captures, an environmental chamber such as the prototype in use here at the laboratory is highly recommended. CO_2 ambient should also be considered.
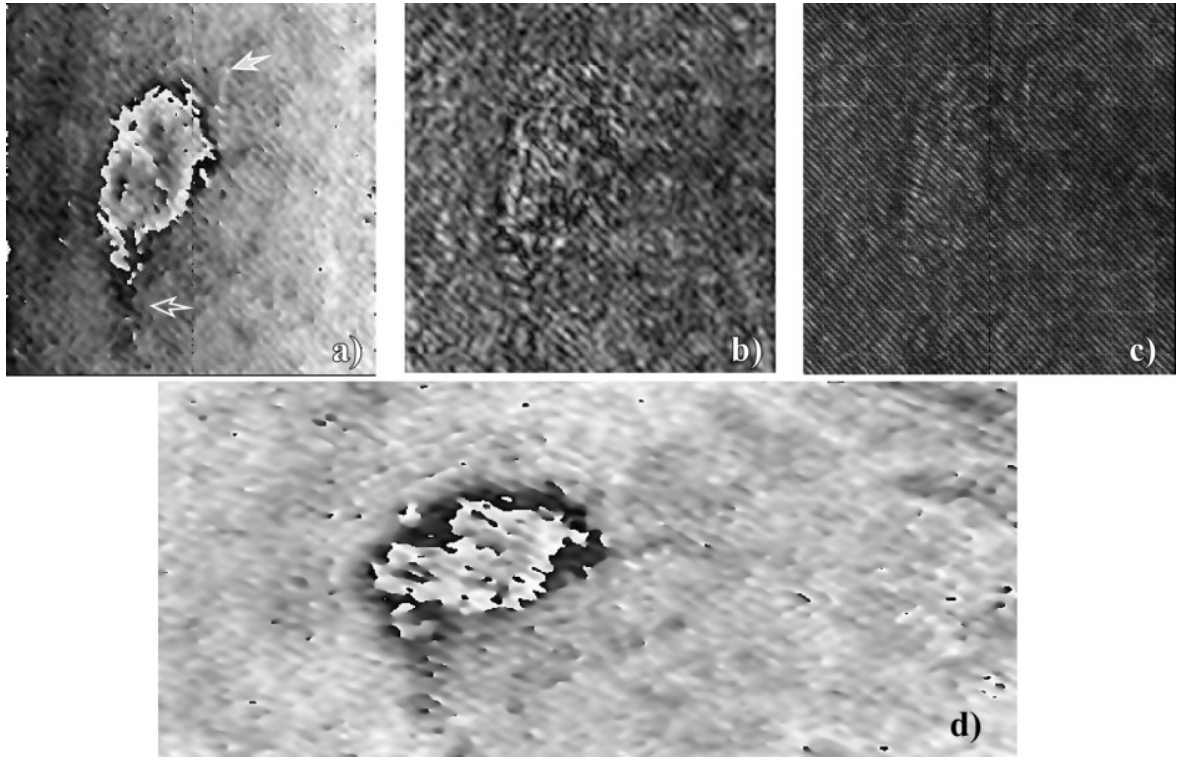
Figure 4.18. SKOV-3 ovarian cancer cell fixed on BK7 prism, with 25x LWD

UNICO Plan a) Phase image, b) amplitude image, c) Hologram, FOV 130 μm (tilt-

compressed) x 57 μm, d) un-tilted (and transposed) phase image. Note lamellipodia

phase signature (arrows).
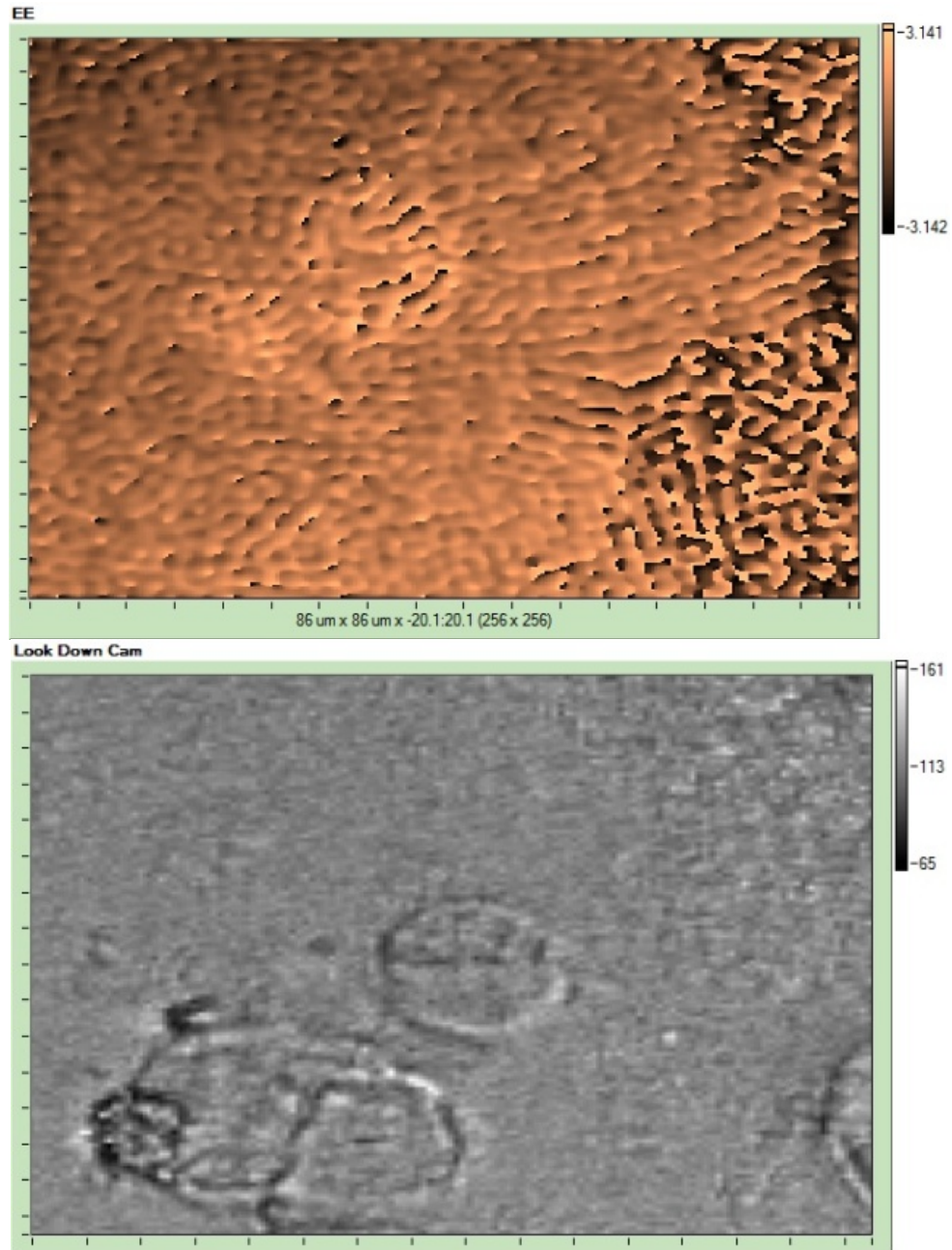
Figure 4.19 Second run of SKOV-3 cultured on SFL11 prism with 25xLWD

UNICO plan. a) TIR phase image shows round feature of cell at center FOV and

ridge adhesion below it, b) Look down camera image. Note that there is slight

rotation in the lookdown camera mount and its FOV.
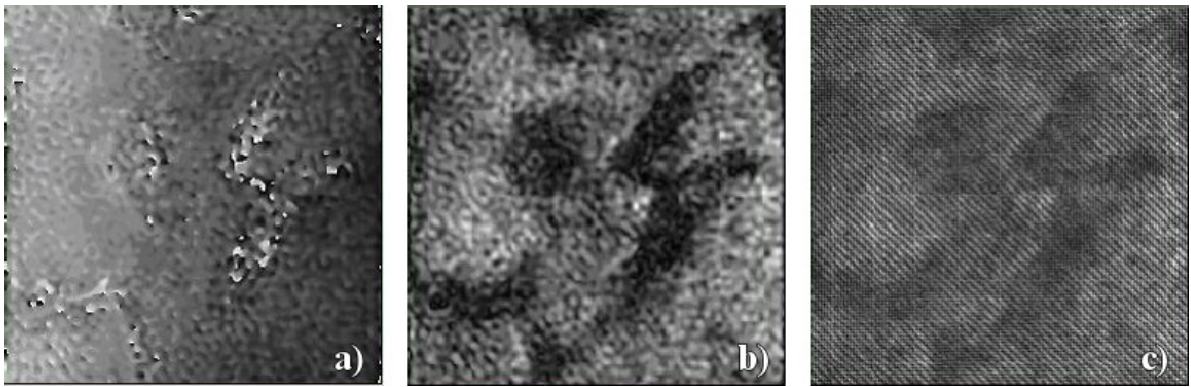
Figure 4.20. 3T3 Fibroblast cell; 25x LWD UNICO Plan with SFL11 prism, a)
Phase image, b) amplitude image, c) Hologram. FOV 180 μm (tilt-compressed) x
90.5 μm

4.5 TIRHM of cell motion

It is desirable to capture phase images of cellular adhesion over time to characterize their dynamic behavior; this necessitates the capture of a set of temporally correlated images as a "movie". While this may sound simple from a theoretical perspective, in practice, the logistics and techniques involved quickly demonstrate the level of talent and experience required for acceptable production of this rather straightforward concept. Variabilities that can be tolerated with "still photography" quickly ruin the most enticing datasets and techniques thought well-honed by hours produce often less-than-spectacular results if useful at all.

The movies here were captured as bmp's (device-independent bitmaps) by routines written into LabVIEW AS Holodiffract for both the phase image and the lookdown camera captures simultaneously (another routine captures and stores the holograms separately for record keeping and post-processing, if necessary). The bmps are then assembled into movies with Apple QuickTime™ Player Pro (7.6.5) with the <File> => <Open Image Sequence> command. which allows the operator to select the first image file out of a file folder of sequentially numbered image files and also select a frame rate for processing (i.e. 2 frames per second). the bmps run around 150Kbytes of memory so the assembled movies can run well into the megabyte range. Figures 4.21 and 4.22 are stills from a *Proteus* run taken with the standard System II 10X MO.
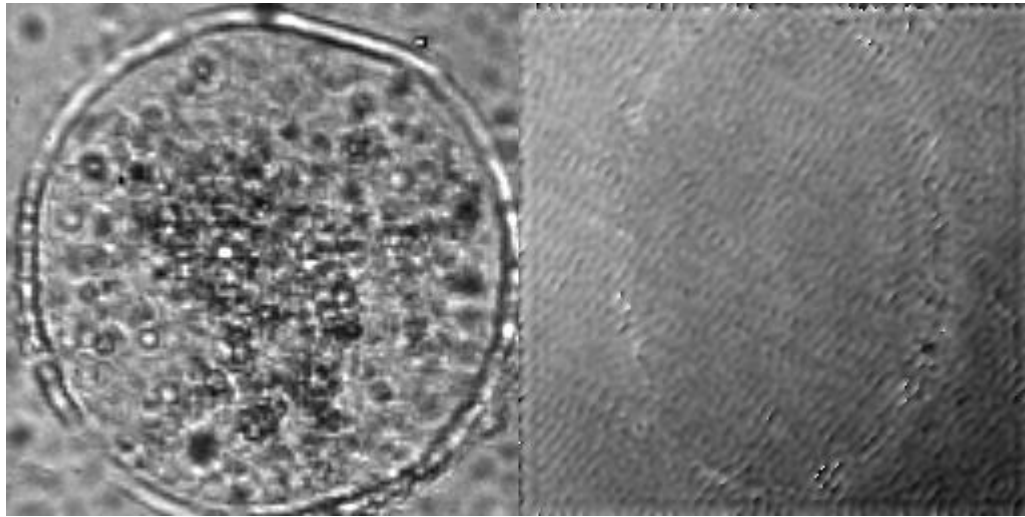
Figure 4.21 Unidentified circular object. Lookdown camera on left, TIR phase image on right. This image sequence was captured during an *A proteus* run. While the object itself is not yet identified, it has a defined outer wall with a pronounced phase signature. The interior contents are seen to circulate in the lookdown movie images.
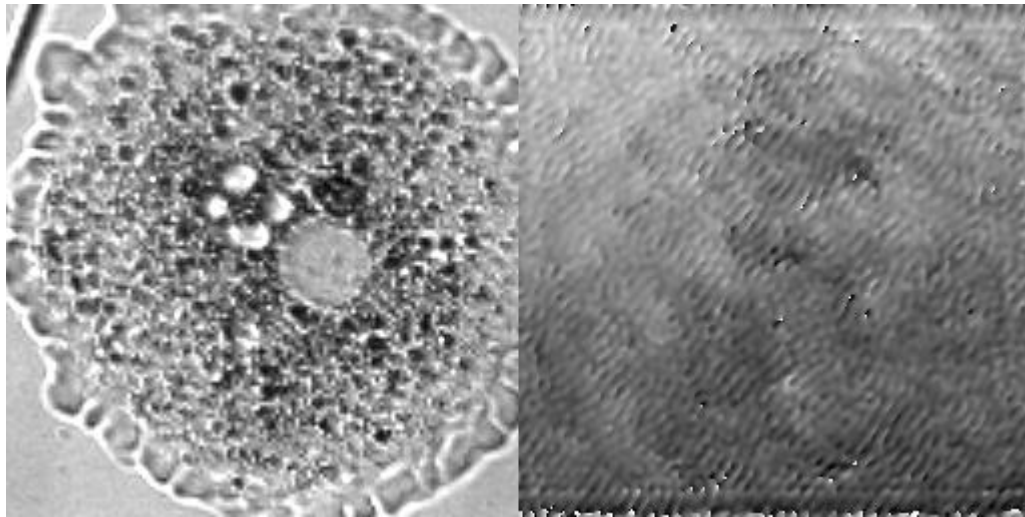
Figure 4.22 *Amoeba Proteus* **under lens flat.** Lookdown camera on left, TIR phase image on right. This proteus has pulled itself up into a ball under the pressure of the lens flat. Its membrane will eventually fail and will come apart under the pressure of the lens these events being captured in a movie sequence.

CHAPTER 5

DISCUSSION

TIRHM images in the near-field without the introduction of stains or fluorophores and makes use of the phase information that is obtained with digital holography. With simple geometries and relative refractive indices, such as our lens and water droplet experiments, we have demonstrated the expected phase shifts predicted by Fresnel reflection theory within reasonable experimental variation. While we have a more complex situation with living cells, we still see phase signatures successful being produced. With an estimation of the cellular refractive index of $n = 1.38$, nominal operation of our system currently can produce a phase contrast of approximately .35 radians ($\Delta\varphi_{water/cell} = 20°$) in an aqueous solution on a $n = 1.785$ SFL11 prism at an angle of incidence of some 52°. This actually exceeds the calculated phase contrast of .28 radians ($\Delta\varphi_{water/cell} = 16°$). Note however, that the change in phase that is caused by the f-TIR thickness profile (gap) between the substrate and the specimens and the relative refractive index (RRI) phase profile from adherent parts of the investigated specimen cannot be differentiated between without additional information or assumptions about the nature of the specimen's adhesions to the substrate.

Since the sensing face is at a sizeable incline with respect to the hologram plane, an en face reconstruction result requires an algorithm that accounts for such inclination. In order to appreciate the geometry of the prism required to produce the evanescent wave, consider that, when looking through the prism, the plane of the object appears to be tilted with respect to the holograph image plane and hence the CCD sensing array. Looking through an SFL11 prism of n = 1.785, the object plane appears to be inclined at about an angle of $\beta = \tan^{-1}$ (n tan θ) ~ 66° (for θ_i = 52°) (which then becomes the un-tilt angle).

The reader should keep in mind, however, that when imaging through a prism in this fashion, in addition to the first-order plane-tilt and optical path effects that must be taken into account, there are higher-order effects in applying a microscope objective system that has been designed for an en face object plane to a tilted object plane, the investigation of which is a subject for further study. Magnification (and N.A.) of the objective versus available working distance through the prism's optical path is another key consideration that must be taken into account.

For numerical comparison, the penetration depth of the evanescent field for 532nm laser light in an SFL11 prism (n_1= 1.785) at θ_1 = 51.7°, the 1/e evanescent wave penetration depth into water (n_2=1.333) is approximately 96nm. The same system with a BK7 prism (n=1.517) at 62° has a 1/e depth of 266nm. Higher prism n was used to lessen the incident angle ($\theta i > \theta c$) tilt for imaging, however, this has the competing effect of reducing the penetration depth.

The *Amoeba Proteus, Dictyostelium Discoideum,* SKOV-3 ovarian cancer and 3T3 fibroblast samples were chosen based upon their availability, suitability, relative

ease of use and, especially in the instance of SKOV-3 and fibroblast, their importance to the field.

Amoeba Proteus have been used for developmental characterization because of their relative ease of use, their inherent interaction with the substrate and the time scale of their motion. A drawback however, to the proteus amoeba is their size; some being physically larger than the field-of-view (FOV) that we are dealing with here (~ 900µm). A review of the literature noticed a curious lack of TIRFM data on A proteus and eventually a dearth of material (apparently supplanted by Dicty work-- being the model organism in this field) followed by a renewed interest in the organism in the mid-1980's, notably by Grebecki [43].

Dictyostelium Discoideum was selected for this investigation because, in addition to being a reasonably 'dependable' organism to work with (i.e. availability, handling, preparation, etc.), it is interesting in that it has motility similar to many adherent cells, demonstrates cellular differentiation during its life cycle, and is a 'model organism' with a well known and understood genome. The *Dictyostelium Discoideum* myxamoeba are relatively small cells (approximately 10 microns), thus requiring a special long working distance (LWD = 5mm) 25x/0.40 microscope objective to be used in this experiment in order to accommodate the thickness of the prism exit path, while still providing meaningful magnification and optical performance. Studied particularly for their agglomeration processes, while the individual *Dictyostelium* make for more challenging detailed features for this particular implementation, it is interesting to note, however, that the phase image clearly shows distinctive composite cellular structures on the scale of the

overall structure captured in the aspect of this particular specimen. The conformal polyacrylamide gelatin layer is also a useful technique having reasonable mechanical properties to keep the specimens relatively hydrated and in the near-field, while being quite transparent and easy to image the direct lookdown camera through.

Being a significant threat to women's health, the study and characterization of SKOV-3 ovarian cancer has been one of our primary goals. SKOV-3 is a relatively small cell (approximately 30 microns), thus requiring the more powerful 25x MO to be used; a special long working distance (LWD = 5mm) unit is employed to accommodate the thickness of the prism exit path.

But TIRHM is not without its own set of considerations. While not necessarily apparent from the cellular features herein, image anamorphism due to the angle of inclination is a subject of design interest that is currently being addressed. Working distance is a related parameter that also must be kept in mind and accounted for in the optical design. These considerations, plus the strong desire to enter and exit perpendicular to the face, and minimize noise and additional tilt from the refraction, while maintaining a greater than critical angle for TIR are driving the design into custom prism angles and refractive indices. As a result of working with the apparatus and these procedures, we find the primary identifiable noise sources to be from the sample surface preparation involved with handling, culturing and fixing these biological specimens. While noisy components cannot be ruled out, system noise can be due to non-optimized illumination that causes light scattering in the experimental setup. All of these sources

are alleviated with continued emphasis placed upon sample preparation, system engineering, alignment and operation.

Also worth mention is the importance of producing and properly handling the angular spectrum, its filtering and reconstruction. The researcher is encouraged to visualize the superposition of the wave vectors for the object and the reference beam plane waves and their resulting diffraction products in k-space that constitute the angular spectrum. Alongside this is the numerical process where the spatial frequency of the hologram is Fourier transformed into angular spectrum k-space and only those spatial frequencies of interest around the first order diffraction peak being selected out by the numerical filter and then reconverted back into image space gaining the phase information in the process. As such, it is the researcher's task to physically adjusts the real space (laboratory) angle between the object and reference beams with the beam recombiner cube rotation and tilt, thus altering the spatial frequency components of the angular spectrum and placing the first order peak away from other diffraction components for it to be properly filtered.

CHAPTER 6

CONCLUSIONS

We have introduced a novel analytical method of total internal reflection holographic microscopy (TIRHM) for obtaining quantitative phase images of micron scale surface profiles in near-field. The theory of TIRHM is developed from the basic Fresnel description of TIR and frustrated TIR (fTIR). Phase shifts in TIR and fTIR are calculated in terms of the indices of refraction, angle of incidence, and the gap thickness. Digital holography allows imaging of the phase profile of TIR and two specific imaging modes of TIRHM, relative refractive index (RRI) and f-TIR shifts are described. In RRI, the reflection phase profile results from variation of refractive index of an object of inhomogeneous optical property in contact with the prism. A biological cell, for example, in complete contact with the prism surface can be imaged to reveal the intracellular structure. In the f-TIR mode, the reflection phase profile images the gap distance between the surfaces of the prism and an object placed on the prism. For example, a biological cell in locomotion can reveal the profile of protrusion of pseudopodia, formation of focal adhesion, development of traction, and release of adhesion.

The holographic microscopy of total internal reflection (TIRHM) is particularly advantageous in cellular microscopy applications for a number of reasons. The imaging

makes use of total reflection, meaning essentially all of the input photons participate in the formation of the image signals, and therefore the input optical power can be kept at minimal level. Although the intensity images of conventional holography are often associated with speckle and other interference noise, the phase images of digital holography are much less susceptible to such noise. The phase image is directly calculated from the hologram as part of the complex optical field. Therefore it is completely quantitative and can be subjected to various numerical processing techniques. In principle, it may be possible to image the phase front of TIR using conventional interference techniques, but the geometry of the imaging system through the prism requires the ability to image a plane with large inclination angle. This is not possible in any existing microscopy technology, whereas digital holography has a great deal of flexibility including the ability to image an inclined plane. With a relatively simple apparatus, one can easily obtain phase images of prism-cell interface with a optical thickness resolution of a few nanometers. We have demonstrated these imaging principles of TIRHM using model objects of liquid droplets and spherical surface of known material and shape. The results unambiguously demonstrate the capabilities of TIRHM to image profiles of these parameters and indicate strengths in potential applications in biomedical cellular imaging.

We have demonstrated a Mach-Zehnder TIRHM system that uses a prism in TIR as a near-field imager in its object arm. The relative refractive index (RRI) shift and frustrated TIR (f-TIR) resulting from the presence of focal adhesions and cell-substrate interfaces on the prism's sensing face modulating the object beam's evanescent wave

phase front. Subsequent processing by digital holography allows for quantitative phase imaging and measurement of the sample features' surface profile. Herein we have reviewed the near-field of Fresnel reflection theory, the angular spectrum method (ASM) of digital holography and discussed this technique to integrate near field microscopy with digital holography to produce a new quantitative form of near field phase microscopy. We have also presented current results with the important model organism, *Dictyostelium Discoideum,* the well-known and characterized *Amoeba Proteus*, as well as 3T3 fibroblast testing and SKOV-3 ovarian cancer cell imagery. Evaluation of the TIRHM system's critical performance parameters displays a resolution capability nearly inherent to that of the microscope objective used, displaying reasonable definition in the phase image down to about G7E2 (3.480 x 17.40μm) with visibility down to at least G7E5 (2.461 x 12.30μm) for a 10X/0.25 μPlan microscope objective.

Based upon the results of our phase shift imagery, we see that we can evaluate which portions of the cell membrane are within the range of the evanescent field, capture their phase shift, and then use this phase shift for quantitative imaging of the sample's focal adhesions at the sample-substrate interface. Frustrated TIR (f-TIR) and relative refractive index phase shift from the presence of focal adhesions and cell-substrate interfaces allows for digital holographic phase imaging such that our TIRHM method successfully integrates phase shift digital holography with evanescent wave surface sensing and phase profile imagery. With the near-field phase microscopy results from *Dictyostelium Discoideum and A. Proteus*, and our results with SKOV-3 ovarian cancer and 3T3 fibroblasts, it is fully anticipated that near term applications include the measurement of

cell motility attributes and adhesion mechanics, without the need to introduce stains or fluorophores. Particularly important are those applications leading to the understanding of morphogenesis, embryogenesis, and cancer metastasis.

Based upon our analysis and results from our phase shift imagery, we see that TIRHM can;

1) evaluate which portions of the cell membrane are within the range of the evanescent field,

2) measure the phase shift for those portions of the cell, and,

3) use this phase shift for quantitative imaging of the sample's focal adhesions at the sample-substrate interface.

As such, this performance is indeed capable of providing a form of quantitative near-field phase microscopy suitable for characterization of cellular adhesions and motility.

FUTURE WORK

Based upon this performance, it is fully anticipated that near term applications include measurement of cellular adhesion and motility attributes, particularly those important to understanding embryogenesis, morphogenesis and cancer metastasis, without the need to introduce stains or fluorophores.

We also excitedly anticipate as near term opportunities, a host of new experiments not only with new samples, but also in combination with other techniques such as correlation of cellular adhesion pull-strength/push strength force tests, correlation testing with fluorophore tags and evaluation of prism functionalizations both biological, such as polylysine, conacavalin, fibronectin, laminin and collagen, and physical functionalizations especially plasmonics. Other experiments include the study and evaluation of wound healing/morphogenesis and quantitative characterization of cellular membranes and motility.

As this research proceeds, all results indicate that TIRHM can soon be available as a tool for quantitative surface imagery by clinicians and researchers. Immediate tasks to be accomplished include, continuing to evaluate system performance and establishment of noise floor, increasing magnification, improvements in sample preparation and handling and new prism designs in support of these initiatives. Evaluation of the unit's performance will continue, and engineering development of a clinical prototype, particularly in combination with other microscopic techniques, also needs attention.

REFERENCES

[1] Leckband, Deborah and Prakasam, Anil, "Mechanism and Dynamics of Cadherin Adhesion", Annual Review of Biomedical Engineering, Vol. 8: 259-287 (2006).

[2] Mitra, Satyajit K., Hanson, Daniel A. & Schlaepfer, David D., "Focal adhesion kinase: in command and control of cell motility", Nature Reviews Molecular Cell Biology 6, 56-68 (2005).

[3] Gumbiner, Barry M., "Regulation of cadherin-mediated adhesion in morphogenesis", Nature Reviews Molecular Cell Biology 6, 622-634 (2005).

[4] Jeanes, A., Gottardi, C J and Yap, A S, "Cadherins and cancer: how does cadherin dysfunction promote tumor progression?", *Oncogene* 27, 6920–6929, (2008).

[5] Bray, D., [Cell Movements: from molecules to motility], 2nd ed., Garland, New York (2001).

[6] Ivan Cameron, Robert Rinaldi, Gerald Kriby, David Davidson, "*Amoeba Proteus*

display a walking form of locomotion", Cell Biology Intl 31, 759-762 (2007)

[7] O'Shea, Donald C., *Elements of Modern Optical Design*, Wiley-Interscience, New York, (1985), page 29.

[8] Murphy, D. B., [Fundamentals of Light Microscopy and Electronic Imaging], Wiley-Liss, New York (2001).

[9] Zernike, F., "How I Discovered Phase Contrast", *Science*, New Series, Vol. 121, No. 3141, 345-349 (1955).

[10] Spencer, M., [Fundamentals of Light Microscopy], Cambridge University Press, London (1982).

[11] James, J. and Tanke H., [Biomedical Light Microscopy], Kluwer Academic Press, Dordrecht (1991).

[12] Debnath, S. K., Kothiyal, M. P., Schmit, J. and Hariharan, P., "Spectrally resolved white–light phase–shifting interference microscopy for thickness–profile measurements of transparent thin film layers on patterned substrates," Opt. Express **14**, 4662-4667 (2006). http://www.opticsinfobase.org/oe/abstract.cfm?URI=oe-14-11-4662

[13] Frits Zernike, Phase Contrast Microscopy, *1953 Nobel Lecture*

[14] http://nobelprize.org/nobel_prizes/physics/

[15] A.S.G. Curtis, " The mechanism of adhesion of cells to glass – a study by interference reflection microscopy," J Cell Biol **20**, 199-215 (1964).

[16] H. Verschueren, "Interference reflection microscopy in cell biology: methodology and applications," J Cell Sci **75**, 279-301 (1985).

[17] A.S.G. Curtis, " The mechanism of adhesion of cells to glass – a study by interference reflection microscopy," J Cell Biol **20**, 199-215 (1964).

[18] H. Verschueren, "Interference reflection microscopy in cell biology: methodology and applications," J Cell Sci **75**, 279-301 (1985).

[19] D. Axelrod, "Cell-substrate contacts illuminated by total internal reflection fluorescence," J Cell Biol **89**, 141-145 (1981).

[20] D. Axelrod, N.L. Thompson, and T.P. Burghardt, " Total internal reflection fluorescent microscopy," J Microsc **129**, 19-28 (1983).

[21] Daniel Axelrod, "Total Internal Reflection Fluorescence Microscopy in Cell Biology", Traffic *2: 764(2001)*

[22] Schnars, U. and Jueptner, W., *Digital Holography*, Springer Verlag, Berlin Heidelberg (2005).

[23] Gabor D 1971 Holography *Nobel Lecture*

[24] J.W. Goodman, Introduction to Fourier Optics, 2nd ed (New York, McGraw-Hill, 1996).

[25] U. Schnars and W.P. Jueptner, "Direct recording of holograms by a CCD target and numerical reconstruction," Appl. Opt. **33**, 179-81 (1994).

[26] S. Grilli, P. Ferraro, S. De Nicola, A. Finizio, G. Pierattini and R. Meucci, "Whole optical wavefields reconstruction by digital holography," Opt. Express **9**, 294-302 (2001).

[27] I. Yamaguchi and T. Zhang, "Phase-shifting digital holography," Opt. Lett. 22, 1268 (1997).

[28] T.-C. Poon, "Three-dimensional image processing and optical scanning

holography," Adv. Imaging & Electron Phys. **126**, 329-350 (2003).

[29] E. Cuche, F. Bevilacqua and C. Depeursinge, "Digital holography for quantitative phase-contrast imaging," Opt. Lett. **24**, 291 (1999).

[30] F. Dubois, C. Schockaert, N. Callens, and C. Yourassowsky, "Focus plane detection criteria in digital holography microscopy by amplitude analysis," Opt. Express **14**, 5895-5908 (2006).

[31] P. Ferraro, S. De Nicola, A. Finizio, G. Coppola, S. Grilli, C. Magro and G. Pierattini, "Compensation of the inherent wave front curvature in digital holographic coherent microscopy for quantitative phase-contrast imaging," Appl. Opt. **42**, 1938-46 (2003).

[232] M.L. Xu, X. Peng, J. Miao and A. Asundi, "Studies of digital microscopic holography with applications to microstructure testing," Appl. Opt. **40**, 5046-5051 (2001).

[33] G. Pedrini and H. J. Tiziani, "Quantitative evaluation of two-dimensional dynamic deformations using digital holography," Opt. Laser Technol. **29**, 249–256 (1997).

[34] W. Xu, M.H. Jericho, I.A. Meinertzhagen and H.J. Kreuzer, "Digital in-line holography for biological applications," Proc. Natl. Acad. Sci. USA **98**, 11301-05 (2001).

[35] K.J. Chalut, W.J. Brown, and A. Wax, "Quantitative phase microscopy with asynchronous digital holography," Opt. Express **15**, 3047-3052 (2007).

[36] D. Carl, B. Kemper, G. Wernicke, and G. von Bally, "Parameter-optimized digital holographic microscope for high-resolution living-cell analysis," Appl. Opt. **43**, 6536-6544 (2004).

[37] Marquet, P., Rappaz, B., Magistretti, P. J., Cuche, E., Emery, Y., Colomb, T. and Depeursinge, C., "Digital holographic microscopy: a noninvasive contrast imaging technique allowing quantitative visualization of living cells with sub wavelength accuracy," Opt. Lett. 30, 468–470, (2005).

[38] K. Jeong, J.J. Turek, and D.D. Nolte, "Fourier-domain digital holographic optical coherence imaging of living tissue," Appl. Opt. **46**, 4999-5008 (2007).

[39] M.K. Kim, "Tomographic three-dimensional imaging of a biological specimen using wavelength-scanning digital interference holography," Opt. Express **7**, 305-10 (2000).

[40] L. Yu and M.K. Kim, "Wavelength-scanning digital interference holography for tomographic imaging using the angular spectrum method," Opt. Lett. **30**, 2092, 2005.

[41] J. Gass, A. Dakoff and M.K. Kim, "Phase imaging without 2-pi ambiguity by multiwavelength digital holography," Opt. Lett. **28**, 1141-3 (2003).

[42] C. J. Mann, L. Yu, C.M. Lo, and M.K. Kim, "High-resolution quantitative phase-contrast microscopy by digital holography," Opt. Express **13**, 8693-8698 (2005).

[43] C. Mann, L. Yu, and M.K. Kim, "Movies of cellular and sub-cellular motion by digital holographic microscopy," Biomed. Eng. Online, **5**, 21 (2006).

[44] Andrzej Grebecki, "Two-directional pattern of movements on the cell surface of Amoeba Proteus," J. Cell Science 83 (1): 23. (1986)

[45] Lucyna Grebecka, Pawel Pomorski, Andrezej Gre and Anna Lopatowska, "Adhesion Dependent F-Actin Pattern in Amoeba Proteus as a Common Feature of Amoebae and the metazoan motile cells", Cell Biology International, Vol 21, Issue 9, September 1997, Pages 565-573

[46] Dormann, D. and Weijer C. J., "Imaging of cell migration" EMBO J. 25:3480–3493 (2006).

[47] Coates, Juliet C. and Harwood, A. J., **"**Cell-cell adhesion and signal transduction during *Dictyostelium* development", *Journal of Cell Science* **114**, 4349 (2001).

[48] Kazuhiko S. K. Uchida and Shigehiko Yumura, **"**Dynamics of novel feet of Dictyostelium cells during migration," *Journal of Cell Science* 117, 1443-1455 (2004)

[49] D. C. Lovelady, T. C. Richmond, A. N. Maggi, C.-M. Lo, and D. A. Rabson, "Distinguishing cancerous from noncancerous cells through analysis of electrical noise" Phys. Rev. E 76, 041908 (2007)

[50] Douglas C. Lovelady, Jennifer Friedman, Sonali Patel, David A. Rabson and Chun-Min Lo, "Detecting effects of low levels of cytochalasin B in 3T3 fibroblast cultures by analysis of electrical noise obtained from cellular micromotion," Biosensors and Bioelectronics, Volume 24, Issue 7, 2250-2254 (2009)

[51] David Brown & Joan E. Strassmann, Permission: CC Creative Commons Attribution - Share Alike 3.0, David Brown & Joan E. Strassmann http://dictybase.org/Multimedia/DdLifeCycles/index.html

[52] De Nicola, S., Finizio, A., Pierattini, G., Ferraro, P. and Alfieri, D., "Angular spectrum method with correction of anamorphism for numerical reconstruction of digital holograms on tilted planes", Opt Express **13**, 9935-9940 (2005).

[53] Jeong, J. and Hong, C. K., "Pixel-size-maintained image reconstruction of digital

holograms on arbitrarily tilted planes by the angular spectrum method," Appl. Opt. **47**, 3064-3071 (2008). http://www.opticsinfobase.org/abstract.cfm?URI=ao-47-16-3064

[54] Matsushima, Kyoji, Schimmel, Hagen and Wyrowski, Frank, "Fast calculation method for optical diffraction on tilted planes by use of the angular spectrum of plane waves," J. Opt. Soc. Am. A **20**, 1755-1762 (2003). http://www.opticsinfobase.org/josaa/abstract.cfm?URI=josaa-20-9-1755

[55] Marvin J. Weber, "Handbook of Optical Materials," CRC Press, Boca Raton, 2003

BIBLIOGRAPHY

Born, M., Wolf, E., *Principles of Optics: Electromagnetic Theory of Propagation, Interference and Diffraction of Light,* Cambridge University Press (1999)

Bray, D. *Cell Movements: from molecules to motility*, 2nd ed. New York: Garland (2001).

Fischer, R. E., and Tadic-Galeb, B., *Optical System Design*, SPIE Press; McGraw-Hill, (2000)

Goodman, J. W., *Introduction to Fourier Optics*, *Second Edition*, McGraw-Hill, Inc., New York, NY (1996).

Hariharan, P., *Basics of Holography***,** Cambridge University Press (2002).

Hariharan, P., *Optical Interferometry, Second Edition***,** Academic Press (2003).

Hecht, E., Zajac, A., *Optics*, Addision Wesley Publishing, Reading, MA. (1974)

James, J. and Tanke H., *Biomedical Light Microscopy*. Dordrecht: Kluwer Academic Press, (1991)

Murphy, D. B. *Fundamentals of Light Microscopy and Electronic Imaging*. New York: Wiley-Liss, (2001).

O'Shea, Donald C., *Elements of Modern Optical Design*, Wiley-Interscience, New York, (1985)

Schnars, U. and Jueptner, W., *Digital Holography,* Berlin: Springer Verlag, (2005).

Spencer, M. *Fundamentals of Light Microscopy*. New York: Cambridge University Press, (1982).

Weber, Marvin, *Handbook of Optical Materials*, CRC Press, Boca Raton, FL (2003)

PAPERS AND CONFERENCES

Ash, William M. , Krzewina, Leo and Kim, Myung K., "Quantitative imaging of cellular adhesion by total internal reflection holographic microscopy," Appl. Opt. **48**, H144-H152 (2009).

W. M. Ash and M. K. Kim, "Digital holography of total internal reflection," Opt. Express **16**, 9811-9820 (2008) http://www.opticsinfobase.org/abstract.cfm?URI=oe-16-13-9811

Ash, William M., Clark, David, Lo, Chun-Min and Kim, Myung K., "Quantitative characterization of cellular adhesions with Total Internal Reflection Holographic Microscopy," in *Digital Holography and Three-Dimensional Imaging*, OSA Technical Digest, (2010).

Ash, William M., Clark, D., Lo, Chun-Min and Kim, Myung K., "Total internal reflection holographic microscopy for quantitative phase characterization of cellular adhesion", Proc. SPIE BIOS, Vol. 7568-58, (2010).

Ash, William M. and Kim, Myung K., "Cellular imagery with total internal reflection

holographic microscopy" Proc. SPIE BIOS, Vol. 7182-9, (2009).

Ash, W. M. and Kim, M. K., "Total Internal Reflection Holographic Microscopy," in *Frontiers in Optics*, OSA Technical Digest (CD) (Optical Society of America), paper PDPB1, (2008) http://www.opticsinfobase.org/abstract.cfm?URI=FiO-2008-PDPB1

Kim, M. K. and Ash, W. M., "Digital Holography of Total Internal Reflection," in *Coherent Optical Technologies and Applications*, (Optical Society of America), paper CTuA4, (2008) http://www.opticsinfobase.org/abstract.cfm?URI=COTA-2008-CTuA4

W.M. Ash III and M.K. Kim, "A demonstration of total internal reflection holographic microscopy for the study of cellular motion," in *Digital Holography and Three-Dimensional Imaging*, Opt. Soc. Am. Topical Meeting (St. Petersburg, FL, March 2008) Technical Digest.

ABOUT THE AUTHOR

Bill Ash received his Bachelor's of Science Degree in Physics from Indiana University of Pennsylvania in 1985 and his Masters of Science in Applied Physics from The Johns Hopkins University in 1995. In addition to his work at The Johns Hopkins University Applied Physics Laboratory, he has also worked in all aspects of aerospace systems from semiconductor fabrication to interplanetary mission analysis for NASA, DoD and the FORTUNE 100 aerospace industry.

As part of his National Science Foundation IGERT-SKINS Fellowship at the University of South Florida, Bill completed an integrated curriculum including work in Electrical Engineering, Anatomy and Technical Entrepreneurship. This resulted in the generation of one US patent for an Interfereometric Chemical Sensor Array and a technological business venture. Bill is also a former President of the USF Student Chapter of the Optical Society of America (OSA), a Duckworth Fellow, and a Charter Member of the USF Inventor's Academy.